

Hybrid Inductive and Capacitive Wireless Power Transfer System for Future Transportation Electrification

by

Deepa Vincent

A thesis submitted to the
School of Graduate and Postdoctoral Studies in partial
fulfillment of the requirements for the degree of

Doctor of Philosophy in Electrical and Computer Engineering

Faculty of Engineering and Applied Science
University of Ontario Institute of Technology (Ontario Tech University)

Oshawa, Ontario, Canada

August 2020

© Deepa Vincent, 2020

THESIS EXAMINATION INFORMATION

Submitted by: **Deepa Vincent**

Doctor of Philosophy in Electrical and Computer Engineering

Thesis title: Hybrid Inductive and Capacitive Wireless Power Transfer System for Future Transportation Electrification

An oral defense of this thesis took place on July 22, 2020 in front of the following examining committee:

Examining Committee:

Chair of Examining Committee	Dr. Ying Wang
Research Supervisor	Dr. Sheldon Williamson
Examining Committee Member	Dr. Vijay Sood
Examining Committee Member	Dr. Jing Ren
University Examiner	Dr. Marc Rosen
External Examiner	Dr. Khurram Khan Afridi Department of Electrical and Computer Engineering Cornell University Ithaca, NY,USA

The above committee determined that the thesis is acceptable in form and content and that a satisfactory knowledge of the field covered by the thesis was demonstrated by the candidate during an oral examination. A signed copy of the Certificate of Approval is available from the School of Graduate and Postdoctoral Studies.

ABSTRACT

The inductive link in wireless power transfer (WPT) fed by various high-frequency power converters is widely accepted for medium power (<50 kW) and medium power transfer distance (100 mm-200 mm) applications due to remarkable efficiencies (>90%) in stationary wireless charging scenarios. However, considering the dynamic or the on the move wireless charging, the inductive link implementation for millions of kilometers is quite expensive due to the need for sophisticated resources. Therefore, relatively inexpensive capacitive link, which initially focused on low power (<100 watts) and small distance (<10 mm) applications, has gained momentum and is explored for medium power (~3 kW) and medium distance (~100 mm) applications. It has achieved considerable DC-DC efficiencies (70%-90%), no induced eddy current loss in the nearby metal objects and low cost and weight implementation.

First, the thesis identifies the significant roles played by inductive and capacitive AC link designs in static and dynamic expansion of wireless electric vehicle charging. Through a relative analysis, the thesis emphasizes the need for mutual promotion of these AC links as a hybrid system in order to boost wireless EV charging technology. Second, capacitive wireless power transfer system is analyzed under different link configurations and dielectric influences aiming to improve their performances. Third, a reduced capacitance model is derived from the existing six capacitance model of bipolar 2x2 matrix configuration which is suitable for large charging area applications like electric vehicle charging. Here, when the separation distance between the same side plate pair is large enough, the effect of cross-coupling capacitances diminishes and the analysis based on a reduced capacitance model can be carried out. The advantage of using this model is that it

attains the unity gain and load-independent operation at designed resonant frequency instead of at dual resonant frequencies in the conventional model. Fourth, a novel hybrid inductive and capacitive wireless power transfer system is realized by combining both systems using a three-leg, mixed switching frequency inverter. The combination offered a choice of power management between two systems. The modular structure makes both systems independent and helps to achieve individual or combined wireless power transfer.

Keywords: coupling; electric vehicles; inductive; capacitive; wireless power

AUTHOR'S DECLARATION

I hereby declare that this thesis consists of original work of which I have authored. This is a true copy of the thesis, including any required final revisions, as accepted by my examiners.

I authorize the University of Ontario Institute Of Technology to lend this thesis to other institutions or individuals for the purpose of scholarly research. I further authorize University of Ontario Institute of Technology to reproduce this thesis by photocopying or by other means, in total or in part, at the request of other institutions or individuals for the purpose of scholarly research. I understand that my thesis will be made electronically available to the public.

DEEPA VINCENT

STATEMENT OF CONTRIBUTIONS

Part of this work has been published or submitted for publication as:

- [1] **D. Vincent** and S. S. Williamson, “Design and verification of a reduced model for capacitive wireless power transfer system for electric vehicle charging” in Proc. IEEE Energy Conversion Congress and Exposition (ECCE), Michigan, USA, Oct. 2020. (accepted)
- [2] **D. Vincent** and S. S. Williamson, "Role of Dielectrics in the Capacitive Wireless Power Transfer System" in Proc. IEEE International Conference on Industrial Technology (ICIT), Buenos Aires, Argentina, Feb. 2020.
- [3] **D. Vincent**, P. S. Huynh, N. A. Azeez, L. Patnaik, and S. S. Williamson, "Evolution of Hybrid Inductive and Capacitive AC Links for Wireless EV Charging -A Comparative Overview," in IEEE Transactions on Transportation Electrification, June 2019.
- [4] **D. Vincent**, P. S. Huynh, and S. S. Williamson, “A novel three leg inverter for high power hybrid inductive and capacitive wireless power transfer system,” in Proc. IEEE 45th Annual Conf. of Industrial Electronics Society (IECON), Lisbon, Portugal, Oct. 2019.
- [5] **D. Vincent**, P. S. Huynh, L. Patnaik, and S. S. Williamson, “Prospects of capacitive wireless power transfer (C-WPT) for unmanned aerial vehicles,” in Proc. IEEE PELS Workshop on Emerging Technologies: Wireless Power Transfer (WoW), Montreal, QC, June 2018.
- [6] **D. Vincent**, P. S. Huynh, L. Patnaik, David Capano, and S.S. Williamson, “Accelerating the autonomous electric transportation revolution: Wireless charging and

- advanced battery management systems” IEEE Transportation Electrification Community (TEC), e-newsletter, Feb.2018.
- [7] **D. Vincent**, S. Chakraborty, P. S. Huynh, and S. S. Williamson, “Efficiency analysis of a 7.7kW inductive wireless power transfer system with parallel displacement,” in Proc. IEEE 1st International Conf. on Industrial Electronics for Sustainable Energy Systems (IECON), Hamilton, New Zealand, Jan. 2018.
- [8] **D. Vincent**, P. S. Huynh, and S. S. Williamson, “Feasibility study of hybrid inductive and capacitive wireless power transfer for future transportation,” in Proc. IEEE Transportation Electrification Conf. and Expo., Chicago, IL, June 2017, pp. 229-233.
- [9] **D. Vincent**, A V J S Praneeth, and S. S. Williamson, "Modeling, Design, and Verification of a Reduced Capacitive Wireless Power Transfer System Model for Transportation Electrification Applications" (to be submitted).
- [10] **D. Vincent**, P. S. Huynh, and S. S. Williamson, "A Three-Leg Inverter Driven Hybrid Inductive and Capacitive Wireless Power Transfer System" (to be submitted).

DEDICATIONS

This thesis is dedicated to my beloved husband, Isidore, who has been a constant source of support and encouragement during this challenging period. I am truly grateful for having you in my life. This work is also dedicated to our lovely children Mia and Joe for their patience and understanding throughout this period. Special dedication to our parents for their spiritual guidance throughout this journey.

ACKNOWLEDGEMENTS

First and foremost I would like to thank God Almighty for giving me the desire, courage, knowledge, ability and opportunity to pursue this Ph.D. program.

I would like to express my sincere gratitude to my supervisor Dr. Sheldon Williamson for allowing me to be a part of his STEER research group. I thank him for his patience, motivation, and immense knowledge which guided me throughout this research. I am thankful for his tireless efforts in bringing research funds to establish the ASSET lab and I feel fortunate to work in this lab. I am extremely grateful for his support in securing the NSERC CGS-D Scholarship and Ontario Graduate Scholarship which would not be possible without his commendable guidance.

I am thankful to the STEER group members Dr. Najath Abdul Aziz, Deepak Rozario, Vamsi Pathipati and Dr. Kunwar Aditya for initiating the wireless power transfer research in this group under the guidance of Dr. Williamson which assisted me in pursuing this research smoothly. I thank Dr. Najath for all the insightful inputs and lab training sessions.

I thank Dr. Lalit Patnaik, Dr. Nimesh Vamanan and Dr. Ashutosh Trivedi for organizing lab meetings, procuring components for the research, conducting brain storming sessions and their timely feedback to enhance my research activities.

I thank my supervisory committee members Dr. Vijay Sood and Dr. Jing Ren for their essential inputs during my research.

I would like to thank all my fellow lab mates Sang, Praneeth, Vinicius, Sandra, Soma, Deepak, Rishi, Arvind, Siddhartha, Janamejaya, Hassan, Manjot, Navbir, David, Yashwanth and Apoorva for their consistent support. Special mention to Sang, Soma, Praneeth, Vinicius and Deepak for stimulating discussions and sharing their specialized knowledge.

I am extremely grateful to the faculty and staff, Ontario Tech for their excellent support throughout this period. I extend my special thanks to Ahmad Shamshiri, Technical support staff for his timely help and Joel Stewart, Graduate Program Assistant, for all the departmental assistance throughout this program.

I would like to thank all my teachers, colleagues and friends from Fr. Conceicao Rodrigues Institute of Technology. It is my pleasure to give special attention to Mrs. Bindu R, Dr. Sincy George, Dr. Sushil Thale and Dr. Mahendra Rane for their timely support in pursuing this program. Further, I thank all my teachers and friends in Sahrdaya College of Engineering and Technology especially Dr. Sudha George for her timely support in commencing this program.

Last but not the least, I extend my heartfelt thanks to all my family and friends for their unconditional love and support.

TABLE OF CONTENTS

THESIS EXAMINATION INFORMATION	ii
ABSTRACT	iii
AUTHOR’S DECLARATION	v
STATEMENT OF CONTRIBUTIONS	vi
DEDICATIONS	viii
ACKNOWLEDGEMENTS	ix
List of Tables	xiii
List of Figures	xiv
List of Abbreviations	xvii
List of Symbols	xvii
Chapter 1. Introduction.....	1
1.1 Wireless charging of electrified transport	1
1.2 Motivation	3
1.3 Research goals and objectives	6
1.4 Thesis organization	9
Chapter 2. Comprehensive review of inductive and capacitive AC links	10
2.1. Inductive wireless power transfer.....	10
2.1.1 IPT System Block Diagram	10
2.1.2 Inductive Coupler Structures	11
2.1.3 Inductive Coupler Structures for Dynamic Wireless Chargers.....	18
2.2. Capacitive wireless power transfer system	21
2.2.1 CPT System Block Diagram.....	21
2.2.2 Capacitive Coupler Structures for WPT	22
2.2.3 Long-distance and Dynamic CPT.....	25
2.3. Comparative Discussion.....	26
2.3.1 Frequency and Power Levels	26
2.3.2 Reactive Power Compensation	28
2.3.3 Efficiency	28
2.3.4 AC Link Power Transfer Density	30
2.3.5 Voltage Stress on the Link	32
2.3.6 Output Power Pulsation in Dynamic Wireless Charging.....	32

2.3.7	AC Link Structure	33
2.3.8	Link Construction Cost Factors	35
2.3.9	Misalignment Tolerance	35
2.3.10	Interoperability of Couplers	36
2.3.11	EMF Exposure Limits	37
2.3.12	Foreign Object Interaction in the Link Proximity.....	38
2.3.13	Power Scaling	39
2.4.	Hybrid Inductive and Capacitive AC Link – New Trend	39
2.4.1	Existing Hybrid Inductive and Capacitive Power Transfer Topologies	41
2.4.2	Future developments	43
Chapter 3. Study of CPT interface for low to medium power EV charging applications		46
3.1	Prospects of Capacitive Wireless Power Transfer (CPT) for Unmanned Aerial Vehicles	46
3.1.1	Design methodology	47
3.2	Coupler Interface design	50
3.3	Low power interface for UAVs.....	52
3.3.1	Design and simulation	53
3.4	High power interface and influence of dielectrics.....	60
Chapter 4. Reduced capacitance model for parallel plate capacitive wireless power transfer system		68
4.1	Reduced Capacitance Modelling and Formation of BCD.....	74
4.2	Voltage gain derivation and comparison of SCM and RCM	78
4.2.1	Equivalent circuit analysis and voltage gain derivation	78
4.2.2	Reduced capacitance model versus six capacitance model	85
4.3	Circuit parameter design, simulation and experimental validation.....	87
4.3.1	Design and Simulation.....	87
4.3.2	Experimental validation.....	89
Chapter 5. Hybrid inductive and capacitive wireless power transfer system		96
5.1	Proposed Topology	99
5.1.1	Circuit schematic	99
5.2	Modes of operation of the proposed converter.....	101
5.3	Steady state analysis.....	104

5.4	System Design and Simulation Results.....	107
5.4.1	Design of IPT system	107
5.4.2	Design of CPT system	111
5.5	Simulation Results.....	114
5.6	Experimental Outcomes	119
5.6.1	Experimental setup	119
5.6.2	Experimental results	122
5.7	Sensitivity analysis	124
5.8	Loss distribution.....	128
5.9	Comparison with the existing HPT topologies	129
Chapter 6. Conclusions and future work.....		131
6.1	Conclusions	131
6.2	Future directions.....	134
References		136
Appendix A.		155
A1.	Publications	155
Appendix B.		159
B1.	SiC MOSFET half bridge module (CREE [®]) (CRD-5FF0912P).....	159
B2.	Synchronous buck configuration (Reference: datasheet CRD-5FF0912P).....	159
B3.	GaN half bridge module (Broadcom and GaN systems).....	160
B4.	Connection diagram (Reference: ACPL-P346 GaN Systems GaN E-HEMT GS66508T)	160
B5.	Rectifier module Reference: GlobalPower SiC modules: GHXS030A120S-D1 datasheet	161
Appendix C.		162
C1.	Approximate cost and weight comparison of AC link built in the lab (without shielding).....	162

List of Tables

Table 2-1 Relevant Standards in Wireless Charging	26
Table 2-2 Static Wireless Power Transfer (IPT) Charging - SAE J2954	27
Table 2-3 Comparison of IPT and CPT Systems	29
Table 2-4 AC Link Power Transfer Density Comparison in IPT and CPT Systems.....	31
Table 2-5 Misalignment Performance Comparison in IPT and CPT Systems	35
Table 2-6 Maximum Permissible Exposure to Electric Field IEEE C95.1, 2005.....	37
Table 2-7 EMF Exposure Reference Levels - ICNIRP, 2010.....	37
Table 2-8 Prospective HPT Lab Prototypes for Wireless EV Charging.....	41
Table 2-9 HPT Configurations for Wireless EV Charging.....	43
Table 3-1 Examples of various capacity drones	49
Table 3-2 Circuit Parameters for 150 mm x 170 mm matrix interface at 20 mm air-gap	55
Table 3-3 Coupler interface parameters.....	59
Table 3-4 Selected dielectric material properties.....	62
Table 3-5 Parallel plate capacitance.....	62
Table 3-6 Circuit parameters for high power interface.....	63
Table 3-7 Influence of Various Dielectrics.....	66
Table 4-1 Circuit parameters for the CPT system.....	90
Table 5-1 WPT system comparison.....	97
Table 5-2 HPT System Specifications	114
Table 5-3 Peak voltage and current stress in IPT components	117
Table 5-4 Peak voltage and current stress in CPT components.....	118
Table 5-5 Comparison with existing HPT topologies.....	129

List of Figures

Figure 1-1 General schematic of WPT system.	2
Figure 2-1 IPT system block diagram.....	10
Figure 2-2 Non-planar couplers.	11
Figure 2-3 Common non-polarized planar coupler. (a) Circular. (b) Square. (c) Rectangular.	12
Figure 2-4 (a) Horizontal X direction misalignment. (b) Horizontal Y direction misalignment. (c) Horizontal XY direction misalignment. (d) Vertical or Z direction air gap variation. (e) Inclined.	13
Figure 2-5 Magnetic flux pattern. (a) Perpendicular – single sided. (b) Parallel – single sided. (c) Flux pipe – double sided.	14
Figure 2-6 (a) DD pad. (b) DDQ pad. (c) Bipolar pad.....	16
Figure 2-7 Short segmented couplers with individual power supply.....	18
Figure 2-8 Long track loop power rails with centralized power supply rail.....	19
Figure 2-9 Segmented couplers with distributed switch box.....	20
Figure 2-10 Segmented couplers with centralized power supply and distributed converters.	20
Figure 2-11 CPT system block diagram.	21
Figure 2-12 Parallel plate structures. (a) Rectangular plates with single dielectric. (b) Dielectric coated Rectangular plates with air-gap. (c) Circular or disk plates.	23
Figure 2-13 (a) Unipolar configuration. (b) Bipolar configuration.	24
Figure 2-14 Non-parallel plate structures (a) Inclined. (b) Deformed-flexible. (c) Deformed- rigid.	24
Figure 2-15 Multistage electric field repeater system.....	25
Figure 2-16 AC link construction cost factors.	34
Figure 2-17 50 kW modular charger prototype for IPT.....	38
Figure 2-18 Relative analysis plot of IPT, CPT and HPT. (The radar graph is ascending away from the center giving lowest (1) to highest (5) values for each factors listed).....	40
Figure 2-19 DC-DC stage of combined inductive and capacitive link proposed in [94].	41
Figure 2-20 DC-DC stage of hybrid inductive and capacitive link proposed in [96]......	42
Figure 3-1 CPT based in motion charging scenario for UAVs.....	48
Figure 3-2 Coupling interface. (a) 1x4 row. (b) 4x1 column. (c) 2 x 2 symmetric matrix. (d) Six plate combined structure. (e) Asymmetric matrix.	51
Figure 3-3 Parallel plate capacitive couplers (a) With single dielectric-Type I (b)With multiple dielectrics- Type II.....	52
Figure 3-4 Coupling interface (a) 1x4 Row (b) 4x1 Column (c) 2 x 2 Matrix	53
Figure 3-5 (a) Block diagram for a series compensated CPT driving UAVs (b) Equivalent circuit.	54
Figure 3-6 Simulation results in PSIM for matrix interface.	55
Figure 3-7 2x2 matrix interface.	56

Figure 3-8 2x2 matrix interface with potential and field distribution.....	56
Figure 3-9 Electric field distribution including the surrounding air region in 2x2 matrix arrangement.....	57
Figure 3-10 4x1 column interface.....	58
Figure 3-11 4x1 column interface with potential and field distribution.....	58
Figure 3-12 Electric field distribution including the surrounding air region in 4x1 column arrangement.....	59
Figure 3-13 Conformal bumper arrangement [23].....	61
Figure 3-14 Electric field distribution in high power interface. (a) Corner field (b) Vector plot	64
Figure 3-15 CPT experimental setup photo with air as dielectric.....	65
Figure 4-1 Layout of CPT system for EV charging.....	68
Figure 4-2 Bipolar capacitive coupler arrangement showing the flow of electric field lines, separation distance d_s and power transfer distance d_{air}	70
Figure 4-3 Six capacitances' influence in the bipolar coupler and its equivalent current source model.....	71
Figure 4-4 Air gap or power transfer distance, d_{air} and separation distance, d_s	73
Figure 4-5 Six capacitances' model to reduced capacitance model approximation by removing same side and cross coupling capacitances.....	74
Figure 4-6 Effect of separation distance, d_s on coupling coefficient, k_E at an air gap, $d_{air}=100$ mm.....	76
Figure 4-7 Effect of separation distance, d_s on coupling coefficient, k_E at an air gap, $d_{air}=25$ mm.....	77
Figure 4-8 Circuit schematic of the CPT system.....	79
Figure 4-9 Steady state switching waveforms of the CPT system.....	79
Figure 4-10 Reduced capacitance model: Equivalent circuit that includes the two main link capacitances (C_{12} and C_{34}) only and the dual LC compensation network.....	80
Figure 4-11 Gain magnitude plot of the CPT with reduced capacitance model for varying load conditions.....	83
Figure 4-12 Gain magnitude plot of the CPT with six capacitance model for varying load conditions.....	85
Figure 4-13 Simulated capacitive link input and output waveforms in PSIM.....	88
Figure 4-14 Photo of the experimental setup.....	89
Figure 4-15 Experimental waveforms of the CPT system a) PWM pulses at switch S_1 (5 V/div) b) V_{GS} at S_1 (20V/div) c) V_{DS} at S_1 (20V/div).....	91
Figure 4-16 Experimental waveforms of the CPT system a) Link input voltage V_P (100 V/div) b) Link input current I_P (5 A/div) c) Output voltage V_O (100 V/div) d) Output current I_O (5 A/div).....	91
Figure 4-17 Efficiency curves a) For varying input DC voltage, b) For varying output power.....	92
Figure 4-18 Output power and efficiency curves for varying separation distance: a) At power transfer distance, 25 mm b) At power transfer distance, 100 mm.....	93

Figure 5-1 Hybrid inductive and capacitive wireless power transfer system block diagram.	98
Figure 5-2 Circuit schematic of the proposed converter for hybrid inductive and capacitive wireless power transfer system.	99
Figure 5-3 The equivalent circuit of the HPT system without rectifier.	100
Figure 5-4 Modes of operation.	102
Figure 5-5 Equivalent circuit of the inductive link.	104
Figure 5-6 Equivalent circuit of the capacitive link.	105
Figure 5-7 Archimedean spiral.	110
Figure 5-8 Simulation Results (a) Switching pulses at S_1, S_2 (b) Switching pulses at S_3, S_4 (c) Switching pulses at S_5, S_6	115
Figure 5-9 Simulation Results (a) Input link voltage, V_{IPT} , primary current, I_{p1} , at inductive link (b) Input link voltage, V_{CPT} , primary current, I_{p2} , at capacitive link.	116
Figure 5-10 Simulation Results (a) Primary side voltage waveforms V_{IPT} and V_{CPT} (b) Primary current, I_{p1} , and secondary current, I_{s1} at inductive link (c) Primary current, I_{p2} , and secondary current, I_{s2} at capacitive link.	116
Figure 5-11 Simulation results (a) Common voltage at secondary side (V_{s1}/V_{s2}) (b) Secondary side currents (I_{s1}, I_{s2} and I_{total}) (c) Output voltage and current (V_0 and I_0)....	117
Figure 5-12 Field distribution simulated in JMAG (a) Magnetic flux density at the Inductive link(μT) (b) Electric field at Capacitive link (V/m) components.	118
Figure 5-13 Photo of the experimental setup.	121
Figure 5-14 Switching pulses at S_1, S_3 and S_5 (upper switches at each leg) (5 V/div). ..	122
Figure 5-15 Inductive link voltage, V_{IPT} (100 V/div), V_{CPT} (100 V/div).	123
Figure 5-16 Voltage and current waveforms at the primary side: V_{CPT} (50 V/div), I_{CPT} (5 A/div), V_{IPT} (100V/div), I_{IPT} (5 A/div).	123
Figure 5-17 Voltage and current waveforms at the secondary side: V_S (100 V/div), I_{S2} (5 A/div), V_0 (100V/div), I_0 (5 A/div).	124
Figure 5-18 HPT system performance for individual misalignment at capacitive and inductive link.	125
Figure 5-19 HPT system power and efficiency curves for simultaneous misalignment in both inductive and capacitive links.	126
Figure 5-20 Power transfer ratio between inductive and capacitive system with respect to misalignment.	127
Figure 5-21 Loss distribution.	128

List of Abbreviations

AC	Alternating current
BCD	Bipolar link dispersion factor
CPT	Capacitive wireless power transfer
DC	Direct current
EMI	Electromagnetic Interference
EV	Electric vehicle
FEA	Finite element analysis
GaN	Gallium Nitride
HPT	Hybrid wireless power transfer
IPT	Inductive wireless power transfer
PWM	Pulse width modulation
RCM	Reduced capacitance modelling
SAE	Society of automotive engineers
SCM	Six capacitance modelling
SiC	Silicon carbide
UAV	Unmanned aerial vehicle
VA	Volt Ampere
WPT	Wireless power transfer

List of Symbols

A	Area
b	Aspect ratio
C	Capacitance
C_m	Mutual capacitance
C_p	Primary compensation capacitor at inductive link
C_s	Secondary compensation capacitor at inductive link
d	Distance between the interface
D	Displacement flux density
d_{air}	Air-gap or power transfer distance
D_{CPT}	Duty cycle for CPT PWM
d_s	Separation distance between same side plates
E	Electric field strength
f_0	Resonant frequency (Hertz)
f_{CPT}	Operation frequency of CPT
f_{IPT}	Operation frequency of IPT
f_s	Switching frequency (Hertz)
k	Coupling coefficient of IPT

k_E	Coupling coefficient of CPT
L	Inductance
l	length
L_1	Primary compensation inductor at capacitive link
L_2	Secondary compensation inductor at capacitive link
L_m	Mutual inductance
L_P	Self inductance of primary coil
L_S	Self inductance of secondary coil
P_0	Output power
P_{CPT}	Power at the capacitive link
P_{IPT}	Power at the inductive link
q	Charge
Q	Quality factor
R_0	AC equivalent of DC load resistance
R_L	DC load resistance
t_d	Dead time
V_0	DC Output voltage
V_c	Terminal voltage at the capacitive link
V_{CPT}	Peak voltage at the capacitive link
V_{dc}	DC input to inverter
V_{in}	Input voltage
V_{IPT}	Peak voltage at the inductive link
V_p	Primary side peak voltage
V_s	Secondary side peak voltage
w	width
ϵ_0	Permittivity of free space
ϵ_r	Relative permittivity
ω_0	Resonant frequency (radians/sec)
ω_s	Switching frequency (radians/sec)
η	Efficiency
Ψ	Displacement flux
δ	Phase shift angle

Chapter 1. Introduction

1.1 Wireless charging of electrified transport

Production of Electric Vehicles (EVs) has exceeded 5.1 million in the year 2018, after surpassing 3 million and 2 million threshold in 2017 and 2016 respectively [1]. It is expected to continue the momentum at an even faster pace. Governments across the globe have set action plans for the rapid adoption of EVs. This will eventually witness the phasing out of internal combustion engines in the future. A major trial for the wide acceptance of EVs stems from the expensive and low energy density battery packs. The longer charging time, limited driving range and a shorter lifetime of batteries again slowed down the scenario. In the conductive/wired EV charging technology, where a cable is plugged in from AC/DC utility to the EV onboard charger, several fast charging options are reported [2]. The driver still needs to wait in front of the charging station, come out of the car and handle a heavy gauge cable that can cause tripping hazards. The conductive/wired charging infrastructures also occupy a substantial area on the sides of highways or parking lots. Mainly, wired charging does not give autonomous charging facility and the EVs must be equipped with heavy and expensive battery packs. Here, the benefits of wireless charging are multifold.

From the time Tesla demonstrated wireless power transfer with his highly resonant tesla coil, the way in which electricity was understood and used has been revolutionised [3]. The various techniques of wireless power transfer based on coupling of electric, magnetic or electromagnetic fields are proven good candidates for meeting specific requirements arising in high frequency/high power applications, like in electric transportation. Wireless power transfer involves the coupling of two or more coils at resonance frequency to transfer

maximum power. The two major near-field wireless power transfer technologies currently being studied in electric vehicle charging are inductive power transfer which uses the magnetic field coupling for the operation and capacitive power transfer that utilizes electric field coupling.

Figure 1.1 depicts a general schematic of wireless power transfer (WPT) system by considering loosely coupled coil pair for inductive wireless power transfer, coupled plates for capacitive wireless power transfer or a combination of coil pair and plates to serve the hybrid power management. The EV carries the secondary coil and the primary coil is fixed on the surface of a parking space, or on the road. The primary side power is provided by a utility supply that can be DC from a battery or low frequency 60 Hz AC from a grid. If the utility is 60 Hz AC, a power factor correction rectifier is used, followed by an inverter. If the utility is DC, a high-frequency converter that is a high frequency inverter then generates a high-frequency voltage at a few tens of kHz. The high-frequency voltage generates high-frequency current through a compensation network and primary coil. A primary compensation circuit aids to keep the primary input voltage and current in phase. This will minimize the reactive power component and thus the size of the high-frequency power converter. The energy from primary side is transferred to the secondary side either by means of magnetic coupling (through loosely coupled coil pairs) or by electric coupling

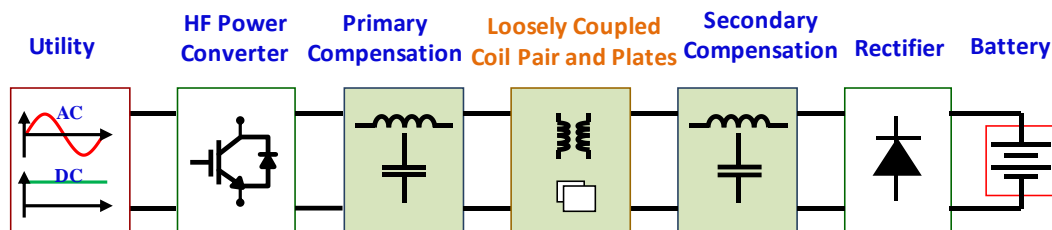


Figure 1-1 General schematic of WPT system.

(through parallel plates) or by both. The secondary compensation circuit improves the power transfer capability of the system and processes the energy received by the secondary side. The voltage thus received is rectified and utilized to charge the batteries. The coupling provided by resonant inductive interface or capacitive interface thus decides the power transfer capability of the system with desirable efficiency values.

The wireless chargers for electrified transport could be deployed in three modes of operation [2], [4], [5]. The first mode is by means of static wireless chargers that are installed in garages, office parking lots or any public/private charging lots. Since the chargers are built at the ground surface levels, it will not obstruct the driver's view [6], [7]. The second mode is by utilizing quasi-dynamic charging in which the charging pads can be installed at bus stops, taxi ranks, traffic lights and even highway shoulders are also ideal for the installation for emergency charging [8]. The last mode is via dynamic wireless charging where the transmitter assembly is installed on the roads offering dedicated charging lanes [9], [10]. Thus, by creating frequent automated charging opportunities, reduced battery size and extended battery life will be a reality. Apart from being the convenient charging option, wireless chargers also provide inherent galvanic isolation between the vehicle side and the grid side. A fully automated wireless charging process for EVs thus proves to be the solution for drive range anxiety and battery overheads [11].

1.2 Motivation

In EV wireless power transfer technology, the power transferred from utility to vehicle side is generally by means of magnetic coupling, resulting in inductive-wireless power transfer (IPT). The DC source to DC load efficiency of an IPT system has reached 95% with 7 kW of output power at 200 mm power transfer distance or air-gap in a laboratory

prototype [16]. This efficiency is comparable to that of conductive EV charging. The system efficiency of commercially available stationary chargers has achieved 92% with a power level ranging from 3.3 to 10 kW at an air-gap of 610 mm [12], [13]. From the literature, it is clear that researchers have stabilized the outcomes in IPT for EV charging [14]. Various commercial products and standards in IPT technology are already in use from nearly two decades ago. However, several drawbacks require attention in this technology.

Primarily, the interference caused by magnetic fields in nearby metals or electronic circuits creates eddy currents in them and in turn contributes to a significant rise in temperature. Researchers have adopted shielding techniques in order to limit the growing flux path around the charging pads [6], [13], [15], [16]. However, eddy currents generated in the metal debris caught in between the charging pads can cause a high temperature, thus leading to combustion hazard [17]. Secondly, the overall cost of IPT coupler interface is dependent mainly on three factors. First is the use litz wire in order to reduce the skin and proximity effect losses. Second is the placement of ferrite cores to direct the flux and third being the EMI shielding techniques adopted. There are several IPT research that focuses on the air-core/core-less implementation that utilizes magnetic field shaping techniques, but effective power transfer is less compared to core backed structures [18]. The cost will be significant when the infrastructure of a dynamic wireless charger needs to be laid, for example in millions of kilometers along highways [19], [20]. In Sweden, to power a 2 km road wirelessly, the cost incurred was €1 million/kilometer [21]. Nevertheless, IPT is a self-sufficient and promising technology. It has already evolved its coupling interface structures and resonant converter topologies to achieve highly efficient wireless power transfer in EV charging.

Recently, researchers started to employ capacitive-wireless power transfer (CPT) based on electric field coupling in high power applications essentially for EV charging [22]–[24]. This technology proved to be a good candidate in low power, low air-gap applications such as charging of biomedical and mobile devices in the last decade [25]. The power frequency product of the CPT system has increased ten times in this period. CPT technology is perceived as the dual of IPT technology. The capacitive compensation circuits in IPT systems and inductive compensation circuits in CPT systems achieve reactive power compensation, unity power factor, minimized VA rating of switches and maximizes efficiency of the WPT system [26], [27]. The main motives behind considering CPT technology for EV charging are the elimination of eddy current loss, low cost and weight, ease of implementation and enhanced misalignment performance [28]. These are substantial reasons for considering the CPT system an ideal candidate for efficient and cost-effective implementation in vast dynamic wireless charging. Having said that, the present CPT system has limits on surface power transfer density, which is the power transfer per unit area of the coupling interface, at higher air gaps compared to an IPT system [29]. Moreover, voltage stress reduction on plates and confinement of electric field emissions are two critical safety accepts that need to be effectively addressed to make CPT ready for commercial EV charging [30], [31].

It is clear that future developments in transportation electrification are centered on wireless charging to a certain extent. The inductive wireless power transfer system evolved greatly in the last two decades and achieved comparable outcomes with conductive charging. Its dual, capacitive wireless power transfer system made a gradual entry into the market with an aim to contribute towards a simple and cost-effective wireless charging

solution for EV at a comparable efficiency. A feasibility study and comparison based on various design and implementation characteristics revealed their benefits and limitations.

1.3 Research goals and objectives

The primary goal of this thesis is to design and implement a novel hybrid wireless power transfer system through combined arrangement of inductive and capacitive couplers. In addition the thesis aims to promote the use of CPT in vehicle charging applications as an alternative to IPT. To meet these goals several objectives are articulated.

1. To identify the need for promoting CPT as an alternative to IPT

The inductive link in a wireless power transfer (WPT) system, is widely accepted for medium power (<50 kW) and medium power transfer distance (100 mm-200 mm) applications in static wireless charging scenarios. However, considering the dynamic wireless charging, the inductive link implementation for millions of kilometers is quite expensive due to the need for sophisticated resources. Therefore, relatively low-cost capacitive link, which initially focused on low power (<100 watts), small distance (<10 mm) applications, has gained momentum and is explored for medium power (~3 kW), medium distance (~100 mm) applications. Through a relative analysis this thesis aims to find the significant roles played by inductive and capacitive AC link designs in static and dynamic expansion of wireless electric vehicle charging.

2. To evaluate capacitive coupler geometry for low to medium power EV applications and explore the influence of dielectrics in capacitive coupler

The value of coupling capacitance is dependent on the dielectric material used, area of the plates in the interface and distance between the plates. The thesis evaluates the influence of dielectrics on capacitive coupler interface for various air-gaps. The coupling interface can be arranged in different configurations such as row, column and matrix to achieve sufficient power transfer and is validated through the electric field analysis in JMAG finite element software. From the analysis of different coupling interfaces, matrix arrangement has a higher mutual capacitance than row/column structure. An increase in mutual capacitance is attained in all configurations if a high permittivity dielectric is employed between the coupling interfaces.

3. To derive a reduced capacitance model for parallel plate configuration in CPT

A reduced capacitance modeling for the CPT system is proposed which is suitable for large charging area applications like electric vehicle charging. Here, when the separation distance between the same side plate pair is large enough, the effect of cross-coupling capacitances diminishes and the analysis based on a reduced capacitance model (RCM) can be carried out. A bipolar capacitive link dispersion factor (BCD) is defined in this thesis to determine the suitability of the RCM. Further analysis showed that, RCM attains the unity gain and load-independent operation at designed resonant frequency. To validate the RCM analysis, a synchronous buck configured dual LC compensated topology is opted for the implementation of the CPT. The system is switched at 1.18 MHz, using GaN switches. The effectiveness of the reduced capacitance model is validated

experimentally for a power level of 100-200 W and the system achieved 72.12% efficiency at power level 114 W.

4. **To design and implement a hybrid inductive and capacitive system to achieve dual frequency operation, sharing of the system power, modularity and misalignment tolerance**

A hybrid wireless power transfer system (HPT) that uses both capacitive and inductive action, for shared power transfer is presented in this thesis. A three-leg inverter topology is used to realize this link independent HPT architecture. Two legs of the inverter, switched at 85 kHz, are used for inductive wireless power transfer (IPT) and the third leg, switched at 1 MHz, is used for capacitive wireless power transfer (CPT). The three-leg inverter module is realized using SiC and GaN switches. The dual switching frequency operation of the converter, is the novelty in the proposed topology. It also enables independent compensation techniques to be adopted for IPT and CPT systems bringing the modularity feature in the hybrid wireless power transfer link. The circular inductive link outer diameter is 460 mm and the parallel plate capacitive link dimension is 600 mm x 600 mm. The power transfer distance is 100 mm at both links. The output power ratio between inductive link to the capacitive link in this HPT system is 2:1. The effectiveness of the proposed topology is validated experimentally and the system prototype achieved 85% efficiency at a power transfer level of 500W. The advantages of this HPT system are modular link architecture, improved misalignment performance and distinct frequency of operation for each link which allows inductive link to meet

the SAEJ2954 standard limits compared to the existing HPT systems proposed for electric vehicle (EV) charging.

1.4 Thesis organization

The thesis outline is as follows:

Chapter 1 presents a brief introduction to wireless charging of electrified transport and the motivation behind selecting the IPT and CPT technologies. Then the research goals and objectives are defined in this chapter.

Chapter 2 deliberates a comprehensive study of inductive and capacitive AC links on various aspects like coupler configurations, static and dynamic charging, standards and an It gives an insight on utilizing the capabilities of both technologies mutually for the enhancement of wireless EV charging.

Chapter 3 discusses the influence of the coupler geometry and the role of dielectrics for low to medium power CPT systems.

Chapter 4 presents a reduced capacitance model and introduces a bipolar capacitive link dispersion factor. A synchronous buck configured dual LC compensated topology is opted for the implementation of the CPT to validate the model.

Chapter 5 discusses the design and implementation of a hybrid inductive and capacitive system to achieve dual frequency operation, sharing of the system power, modularity and misalignment tolerance.

Chapter 6 summarizes the contributions in the thesis with an insight into the future works.

Chapter 2. Comprehensive review of inductive and capacitive AC links

2.1. Inductive wireless power transfer

2.1.1 IPT System Block Diagram

The architecture of an inductive wireless power transfer system for EVs is as shown in Figure 2.1. It consists of low frequency to high frequency power conversion stage followed by primary compensation network and coupler interface at the primary side/ground assembly. Thus creating a resonant tank at the primary side. At high power and frequency levels, as the leakage inductance is high, to attain the desired power level, current needs to be increased. This will create conduction losses in the system in addition to the existing reactive power. Thus, the Volt-Amp (VA) rating of the inverter needs to be increased if there is no adequate compensation. In order to achieve stable soft switching, the inverter switching frequency is kept slightly different from the resonant frequency. Therefore, compensating the primary reactive power reduces the VA rating of the inverter switches, enables soft-switching operation of the switches to reduce switching losses and prevents

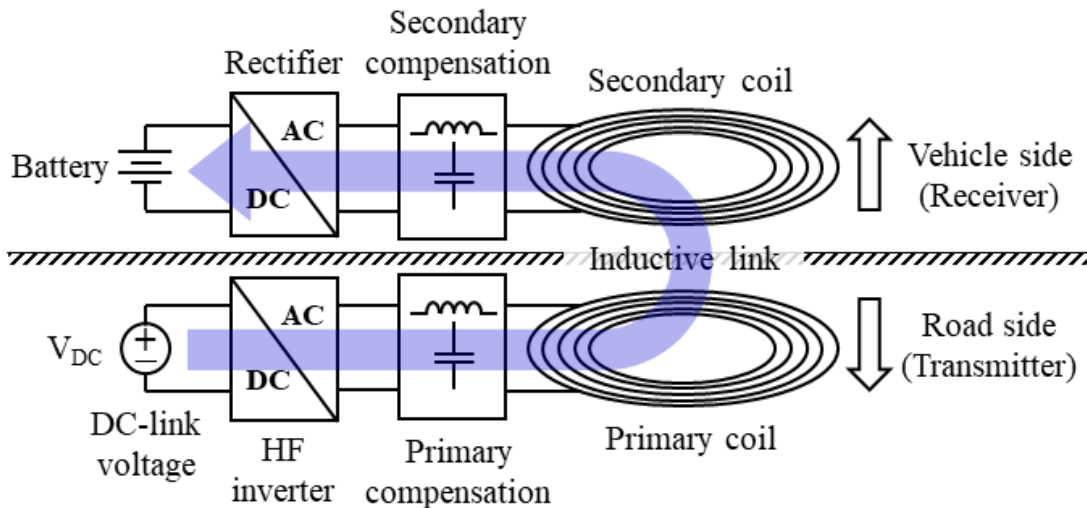


Figure 2-1 IPT system block diagram.

the harmonic propagation in the circuit due to its filtering function. At the vehicle side, a secondary compensation network and rectifier follow coupler interface to the load. Here, the secondary circuit operates at resonant frequency to improve the power transfer capability of the system [6], [27], [32].

2.1.2 Inductive Coupler Structures

The inductive AC link design is mainly categorized in this thesis into non-planar couplers and planar couplers. In non-planar couplers, the link structure is developed around different shapes of cores and named after that. In planar couplers, the link is constructed and named based on the geometry of the coil structure. However, in some cases, coil structure is named after the way the magnetic field is generated. This is further classified into polarized and non-polarized designs based on the shape of the magnetic path. The recent research focusing on air-core/ferrite-less construction of inductive coupler is also discussed in this section.

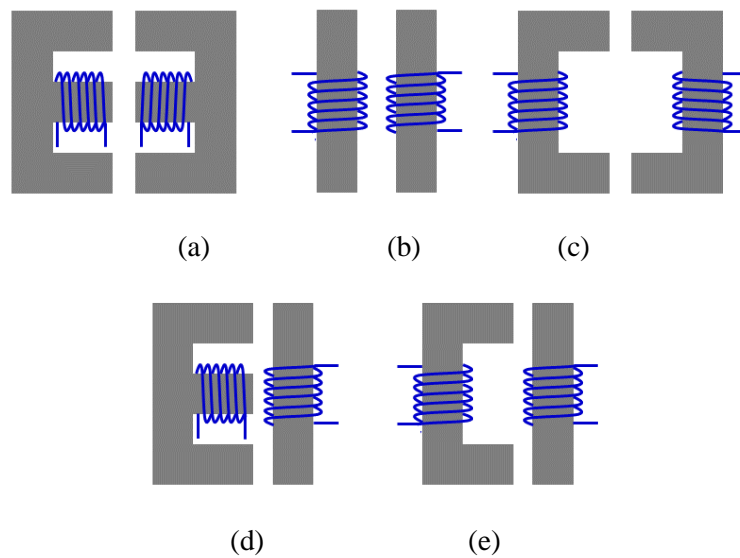


Figure 2-2 Non-planar couplers.

2.1.2.1 Non-planar Couplers

The conventional magnetics design of ferrite core based couplers enhances the coupling coefficient between primary and secondary windings. It reduces unwanted stray magnetic radiation in addition to improving coupling efficiency with low eddy current and hysteresis losses in high frequency application [33], [34].

In Figure 2.2, the primary and secondary winding on various geometries based on E-E, I-I, U-U, E-I, U-I ferrite core combinations are given. For the EV charging application, ferrite core prominent structure can compromise the ground clearance due to the ferrite thickness and in order to accommodate the charger, EV chassis modification is necessary. However, bumper to wall charging option is possible without any extensive modification to EV chassis. Therefore, non-planar couplers are useful for wireless charging of electric

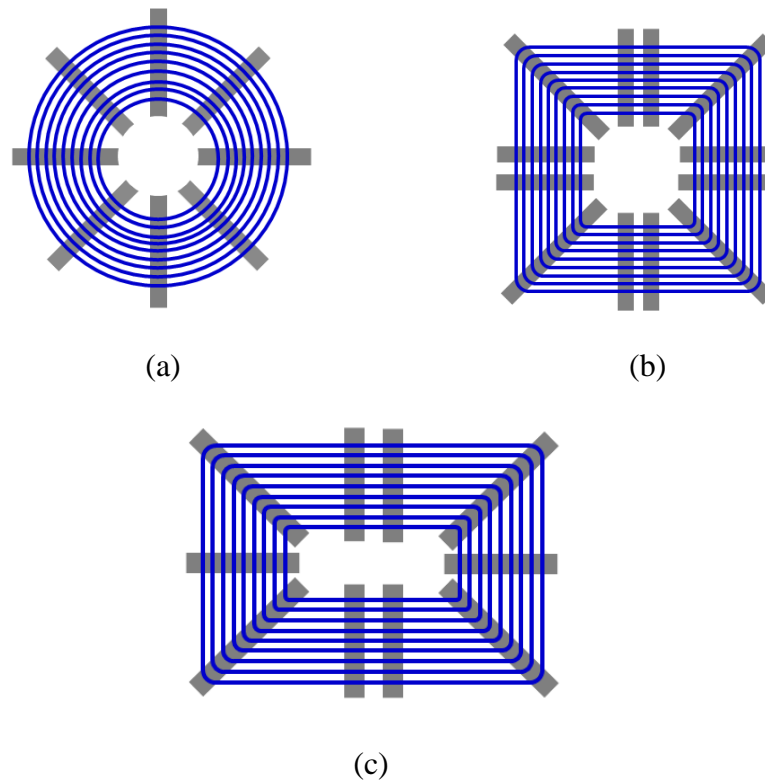


Figure 2-3 Common non-polarized planar coupler. (a) Circular. (b) Square. (c) Rectangular.

golf carts, mine carts, etc. In [33] paddle and disc type ferrite core structures are investigated in which disc type design has reduced weight and better coupling efficiency.

2.1.2.2 Planar couplers

2.1.2.2.1 Non-polarized Charging Pads

The common coupler structures in the non-polarized charging pads are circular, square and rectangular shaped pads, Figure 2.3. The couplers can be designed without ferrite cores (air-core) for power ratings in the range of hundreds of watts. For higher power applications, the flux lines are guided from the primary to secondary by adding ferrite bars. The optimum arrangement of ferrite bars channels the flux lines and increases the coupling [35]. Hence, magnetic field direction in these structures is single-sided which means flux lines are entering and leaving from one side [36]. The leakage flux is then shielded using

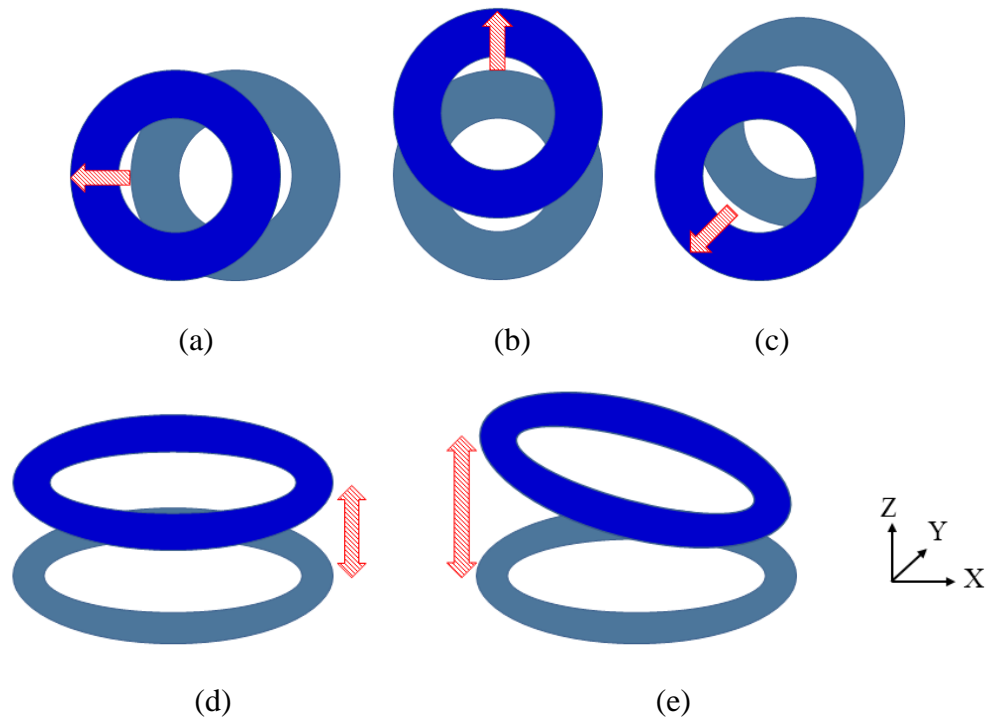


Figure 2-4 (a) Horizontal X direction misalignment. (b) Horizontal Y direction misalignment. (c) Horizontal XY direction misalignment. (d) Vertical or Z direction air gap variation. (e) Inclined.

aluminum plates, by placing coils and ferrites on the shielding plates [15]. This minimizes any interaction of magnetic flux with the surroundings. Misalignment positions and air gap/ground clearance variations are given in Figure 2.4. The horizontal or parallel displacement positions can be in the X direction, Y direction and XY direction, Figure 2.4(a)-(c). The vertical or perpendicular displacement in the Z direction is also termed as power transfer distance or air-gap, Figure 2.4(d). Due to uneven loading or a flat tire, the receiver at the vehicle side can have a tilted/inclined position as well, Figure 2.4(e).

The circular coupler has the same tolerance to misalignment in all directions or it is non-directional [37]. The square and rectangle shaped couplers increase the flux area and their cost-effective design has better power transfer capability [38]. The single-sided and

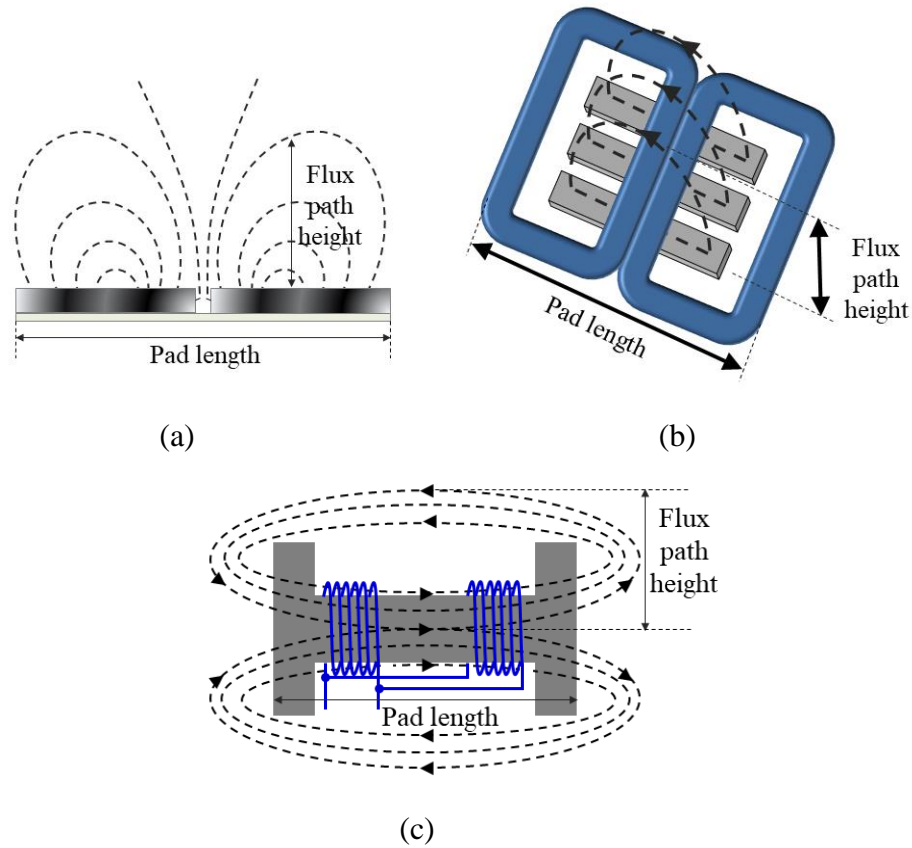


Figure 2-5 Magnetic flux pattern. (a) Perpendicular – single sided. (b) Parallel – single sided. (c) Flux pipe – double sided.

double-sided magnetic flux pattern are given in Figure 2.5. In non-polarized coupler designs, the perpendicular/vertical flux component, Figure 2.5(a), alone is generated and coupled. The flux lines leaving from the primary side of the coupler are travelling perpendicular to the surface while entering the secondary side. The distance, flux travels from transmitter to receiver is dependent on the size of the transmitter pad and is defined as flux path height. The flux path height in non-polarized coupler design is a quarter of transmitter pad length and thus has a lower coupling coefficient. In the mutual coupling profile, circular couplers exhibit magnetic null due to flux cancellation at 40% horizontal X direction misalignment [35].

2.1.2.2.2 Polarized charging pads

The parallel/horizontal component of flux, Figure 2.5(b), is utilized in these types of charging pads and are derived from flux pipe or solenoidal field design. A flux pipe channels flux along a maximum length of ferrite to increase the flux path height by connecting two coils in parallel on the charging pad, to lower the inductance seen by the power supply. The mutual flux path extends from one end of the pole to the other. The main advantage is that the height of the flux path is half of the pad length and therefore it has a higher horizontal X direction misalignment tolerance. This design has a double-sided flux path as shown in Figure 2.5(c).

The rear side flux is shielded using aluminum plate. However, the high frequency magnetic flux creates eddy current losses in the shield. This adds to the total losses in the system. Thus reducing the quality factor as it is an indication of how much energy is placed in storage (continual transfer from one reactive element to the other) compared to that dissipated in resistive element. The system power output is proportional to quality factor,

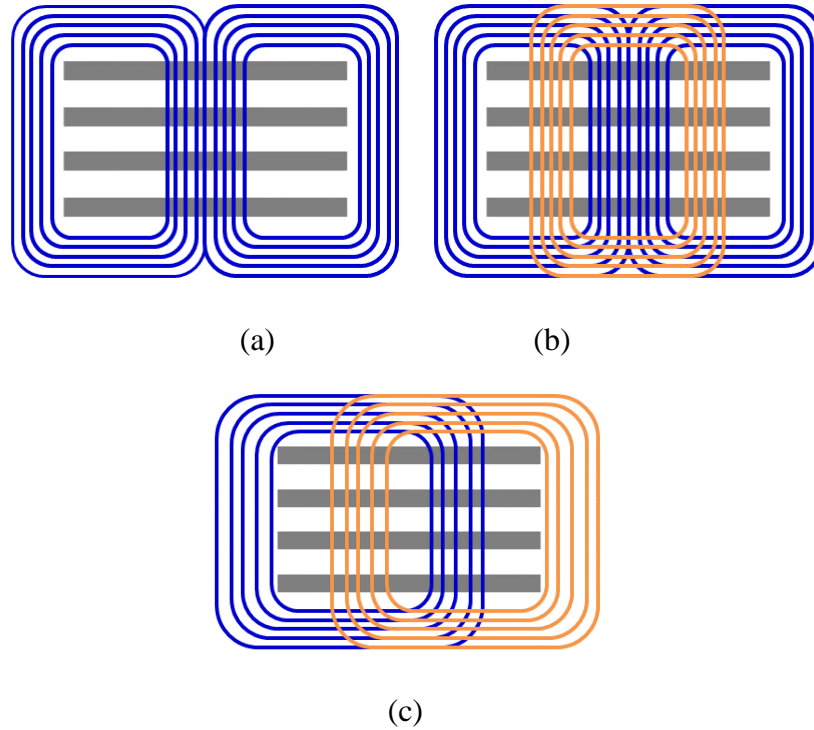


Figure 2-6 (a) DD pad. (b) DDQ pad. (c) Bipolar pad.

hence affecting the efficiency of the system. The structure derived from the flux pipe is aimed to generate a single-sided flux with the same flux path height as that of flux pipe is the Double D (DD) pad, Figure 2.6(a). Here, two D shaped coils are magnetically in series and are placed above ferrite bars, generating only a single-sided flux path [35], [36].

DD pads are non-interoperable with non-polarized circular pads and have a magnetic null due to flux cancellation when horizontal X direction misalignment is $\sim 34\%$. A double D quadrature pad (DDQ), Figure 2.6(b) is derived from DD by adding a quadrature coil below the DD coils in the center. Thus, both vertical and horizontal component of flux is captured and thereby avoiding power nulls with horizontal displacement. Hence, it has a higher misalignment tolerance in horizontal X and Y directions. However, in order to excite the DDQ charging pad, two synchronous inverters at primary and two synchronous rectifiers at the secondary side are required. The DDQ charging pad can generate polarized

or parallel, non-polarized or perpendicular or both components of flux depending on the excitation of the DD and Q coils [39].

A bipolar pad (BP) design, Figure 2.6(c) proposed in [40] has two identical mutually decoupled coils that overlap at the center and are placed over the ferrite core. The coupling coefficient and misalignment tolerance of BP are equivalent to DDQ pad. The BP design has a similar performance to DDQP, but it is simpler to construct and uses less amount of copper. In [29], a compact and efficient BP design is outlined which integrates the planar type compensation inductors into the DD pads to share the cores. In [41], intermediate embedded couplers are proposed to increase the coupling from primary to secondary pads. A coplanar, independently tuned intermediate coupler based on two coil and three coil structures has improved the efficiency of this system.

2.1.2.3 Ferrite-less structures

Ferrite-less pads are an effective alternative to ferrite dependent designs. Increased mechanical robustness makes it practically more oriented to dynamic wireless EV charging applications [10], [42]–[44]. Ferrites were deployed to boost the power transfer and reduce the leakage flux in WPT systems. However, ferrites are brittle in nature, expensive and losses in these cores at high power can aid in the thermal runaway of the WPT system. In [44], the leakage EMF outside the primary and secondary pads are mitigated by means of out of phase flux cancellation coils. By combining a conductive plate and flux cancelling resonant coil, the leakage flux in large air gap applications is controlled [18]. A similar approach where only an inductive coil connected in series-opposing configuration with the main coil is designed to minimize the flux beneath the charging pad and outside the

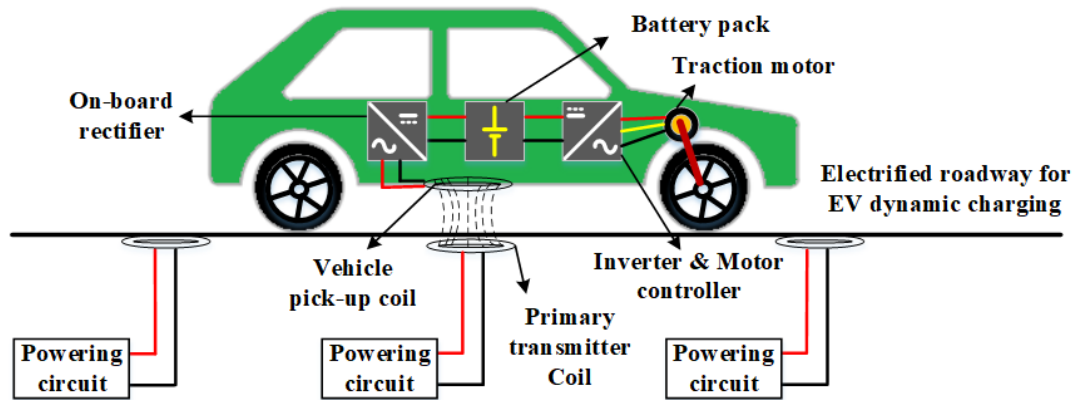


Figure 2-7 Short segmented couplers with individual power supply.

charging area is introduced in [43]. Even though ferrite-less pads promises a reduction in leakage flux, it adversely affects the coupling factors thus cannot effectively contribute to the power transfer capability of a WPT system. Another solution is to keep only the transmitter coil ferrite less which ensures cost reduction and robustness [10], [42].

2.1.3 Inductive Coupler Structures for Dynamic Wireless Chargers

Wireless power transfer in EVs can happen through static or dynamic modes [2], [5], [7]. In static wireless charging, the vehicle is stationary and aligned above the charging link. The coupler designs for static wireless chargers are suitable to be installed in public charging stations, house garages, office and mall parking lots etc. When the vehicle charges on the go, it is termed as dynamic wireless charging which is a very effective method of wireless power transfer. It can eliminate the range anxiety problem in an EV and reduce the size of batteries utilized. The long track power rails, short segmented and segmented power rails are different types of dynamic mode coupler structures.

2.1.3.1 Short Segmented Couplers with Individual Power Supply

The magnetic couplers discussed in static wireless charger section can be employed here as well due to the availability of individual power supply for each short segments, Figure

2.7. The power pads will be energized only when a wireless EV passes over it [6], [13], [45]. The advantages of short-segmented couplers are efficiencies up to 93% for power levels of 22 kW, compact structure, reduced leakage EMF and high reliability. Due to the short segment implementation, the challenge is in designing the automatic detection system to energize the required segment and it also involves high construction and maintenance cost.

2.1.3.2 Long Track Loop Power Rail Couplers with Centralized Power Supply

A basic long track loop power rail with two wires forming a loop without any magnetic material adopted for roadway powered EVs is depicted in Figure 2.8. Korea Advanced Institute of Science and Technology (KAIST) initiated this model in On-Line EV generations (OLEV- 1G-5G) for on the go EV charging [13], [20]. The misalignment performance of the power rail is improved by adding magnetic material with different core shapes to direct the flux towards the secondary. Different core shapes E, I, U, W and S type are employed for power supply rail and a comparison is provided in [4].

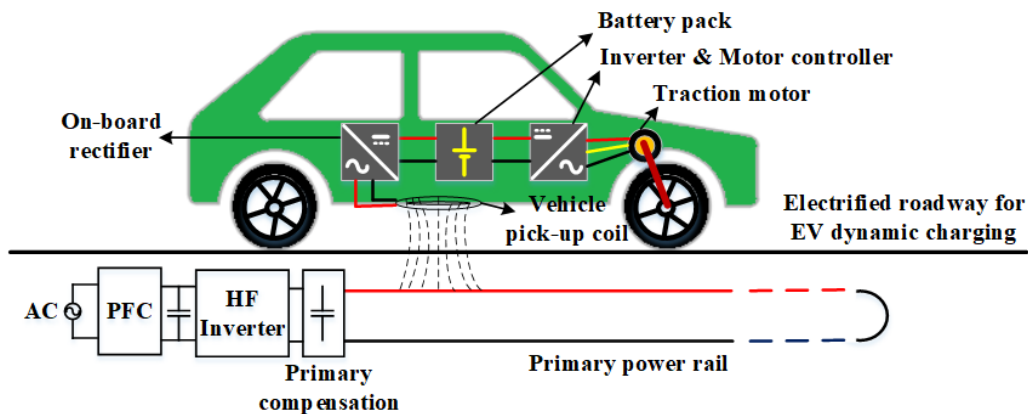


Figure 2-8 Long track loop power rails with centralized power supply rail.

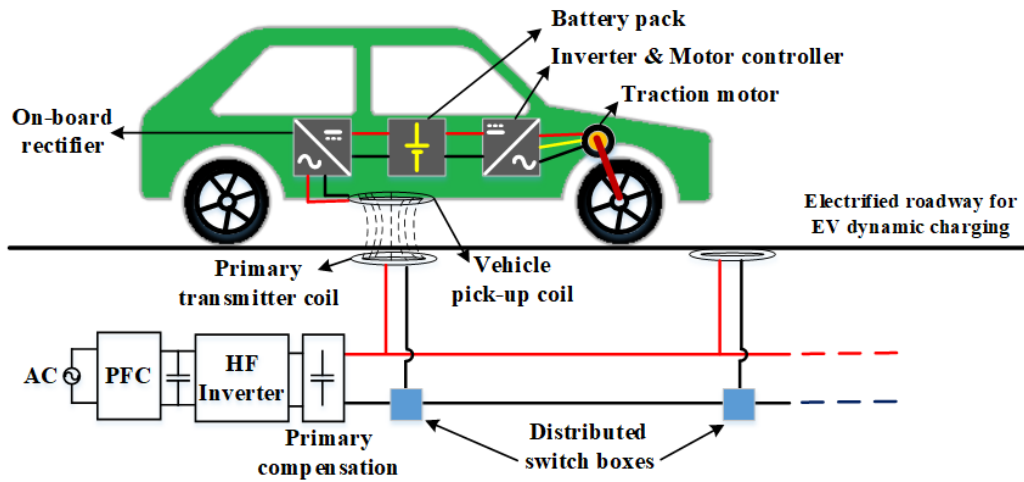


Figure 2-9 Segmented couplers with distributed switch box.

The earlier pick-up designs were experimental and generally flat type, E type and U type were chosen in order to easily adopt into the existing infrastructure [46], [47]. Later, the S type pick up gave an enhanced power density, however, the core fabrication is complex [20]. To enhance the lateral misalignment performance, a quadrature pick up (E type with additional coil) is introduced in [48].

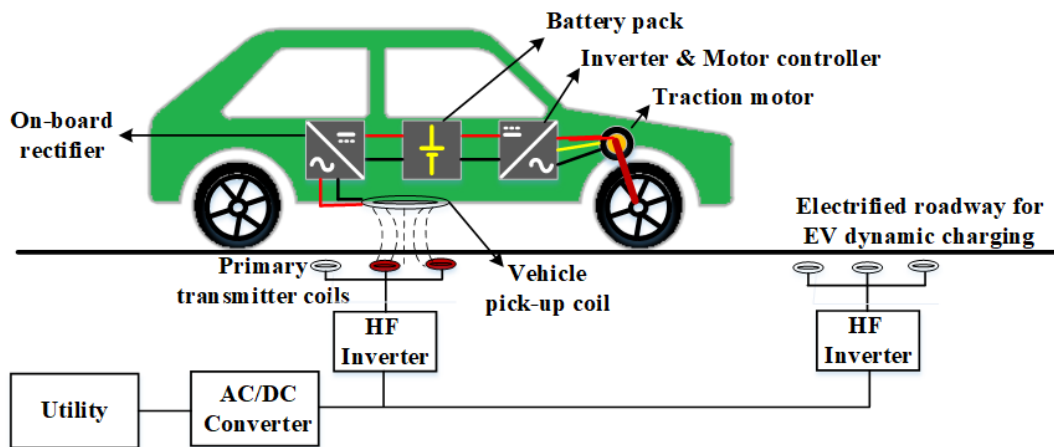


Figure 2-10 Segmented couplers with centralized power supply and distributed converters.

2.1.3.3 Segmented Power Rails with Centralized Power Supply

To improve the energy utilization and to reduce leakage EMF, instead of long power rails with centralized supply, segmented power rails are proposed. This has many sub rails that can be activated through a distributed switch box as required, which is fed from a centralized power supply as shown in Figure 2.9. The switch box controls the activation of each segment as the vehicle approaches and deactivates the segment once the vehicle passes over it. The energy consumption and losses are reduced over the entire length by modifying this infrastructure with distributed converters, as given in Figure 2.10, which are fed from centralized at the expense of construction cost and complexity [49].

2.2. Capacitive wireless power transfer system

2.2.1 CPT System Block Diagram

A CPT system depicted in Figure 2.11, is energized from a high frequency voltage source at the primary, which drives the capacitive coupler. The various types of high frequency inverters used in the primary side are voltage fed full/half bridge resonant converter, current fed push-pull resonant converter and class E converter [28]. The

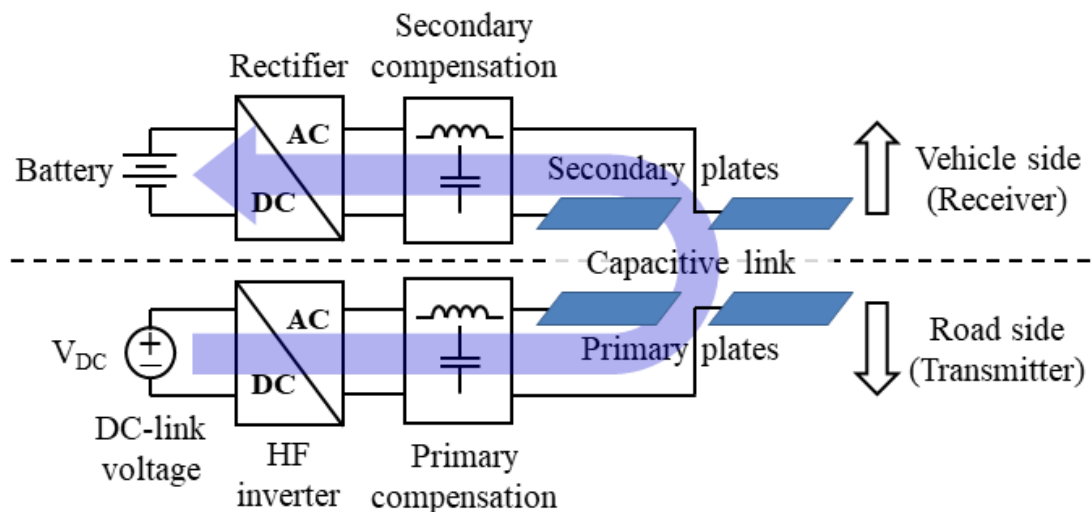


Figure 2-11 CPT system block diagram.

capacitive coupler allows the displacement current to flow through it acting as an energy transfer medium. The coupler structure and alignment conditions determine the capacitance of coupling plates that decides the power transfer capacity. Depending on the application, a capacitive coupler structure can be implemented in different configurations.

The coupling capacitance is in the range of tens-hundreds of pF for large air-gap application. It depends on the plate area, distance, and the dielectric material (typically air for large distance/air-gap application) between the plates. The permittivity constant ϵ_0 of air is as small as 8.85×10^{-12} F/m coupled with large air-gap operation limits the value of coupling capacitance. Therefore, the compensation network and the coupler forms a resonant tank, to produce high voltages on the plate to generate sufficient electric fields for power transfer. Since the capacitance is small (\sim pF), by increasing the resonant frequency range (\sim MHz), the resonant inductor value can be kept low (\sim μ H). At the secondary side, a compensation circuit follows the coupler structure.

2.2.2 Capacitive Coupler Structures for WPT

For the capacitive AC link design, coupling interface at the primary and secondary side includes metal plates that are coated using a suitable dielectric/insulator separated by an air-gap [22], [50]. This type of link design, with horizontal or vertical parallel plate structures in general, is simpler and cost-effective compared to the litz-ferrite combination [23], [51], [52]. The value of the capacitance that is obtained between the coupling plates directly impacts the maximum power transferred and efficiency of the system. It depends primarily on the structure and the distance between the plates. The capacitive link is mainly classified as parallel plate and non-parallel plate structures. For high power EV charging applications [53], parallel plate structures are popular in the literature. However, a non-

parallel plate deformed architecture is recently employed with minimum spacing between the plates [23]. In the following section, these structures are discussed.

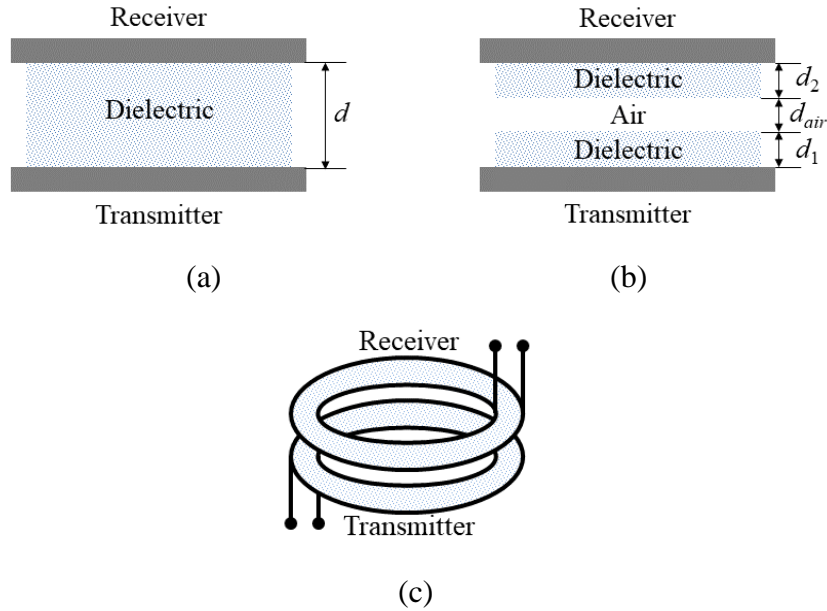


Figure 2-12 Parallel plate structures. (a) Rectangular plates with single dielectric. (b) Dielectric coated Rectangular plates with air-gap. (c) Circular or disk plates.

2.2.2.1 Parallel Plate Structures

The parallel plate structures are generally implemented in the rectangular/square and circular/disk type architecture as given in Figure 2.12. The parallel plate architecture is constructed in general with at least two plate pairs forming a bipolar or unipolar configuration. In a bipolar configuration, both plate sets are active and contribute to the wireless power transfer. When both pairs are active, each pair forms a main capacitance in series to complete a power transfer loop as given in Figure 2.13 (a). When one pair is active, it gives rise to unipolar configuration and the power loop is completed by the passive plates, Figure 2.13 (b).

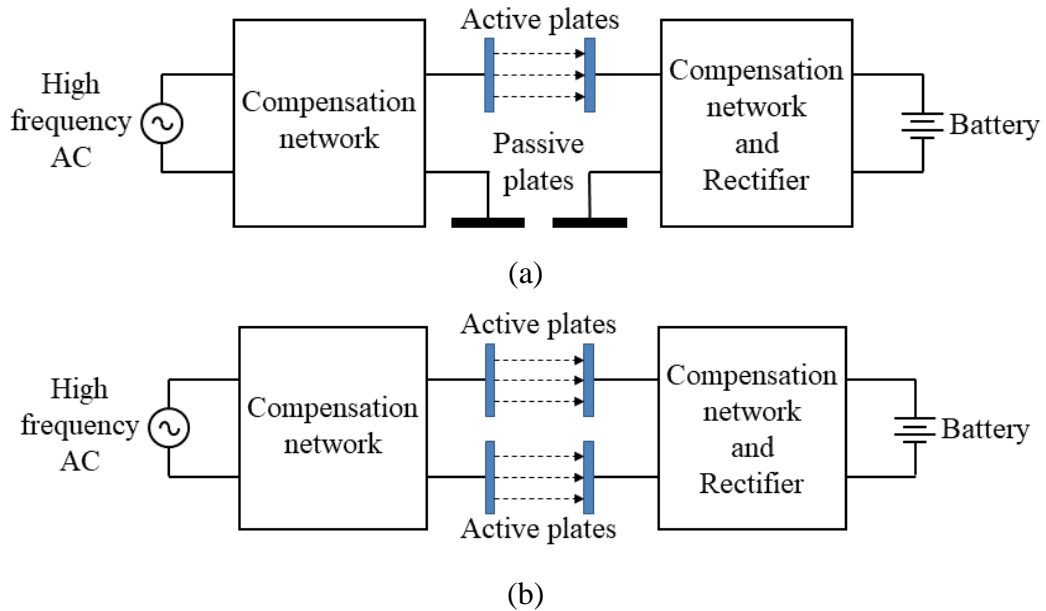


Figure 2-13 (a) Unipolar configuration. (b) Bipolar configuration.

2.2.2.2 Non-parallel Plate Structures

In non-parallel plate structures, at least one of the plates of the system is either inclined or deformed as shown in Figure 2.14. The inclined structure in Figure 2.14 (a) is formed when the secondary plate is inclined at an angle θ with respect to the primary. The

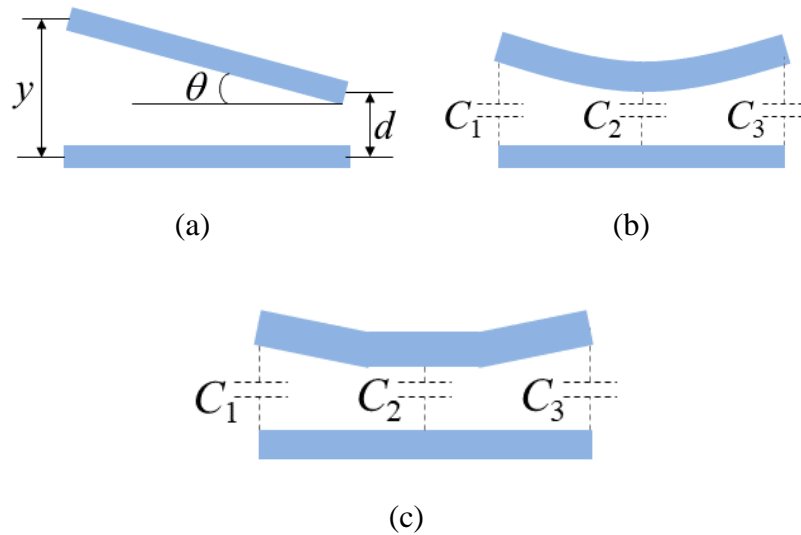


Figure 2-14 Non-parallel plate structures (a) Inclined. (b) Deformed-flexible. (c) Deformed- rigid.

deformed construction can either provide a more flexible or rigid deformation as given in Figure 2.14 (b) and (c). The flexible structure, Figure 2.14 (b), can adhere well in front of an EV, where the capacitance decreases from the center to outwards. A conformal transmitter that molds and contours itself at the front end of the vehicle with high capacitive coupling was demonstrated for a 1 kW EV charging application [23].

2.2.3 Long-distance and Dynamic CPT

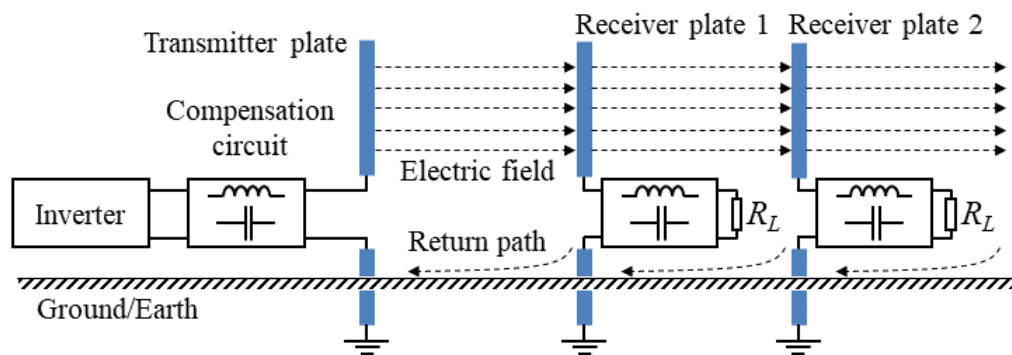


Figure 2-15 Multistage electric field repeater system.

For long-distance power transfer in CPT, repeater systems are proposed in [54] which consists of a transmitter energized from the source and multiple receiver plates that act as repeaters. A unipolar configuration in Figure 2.15 with two active plates at each stage and passive plates at a common ground for the current return path can serve as a quasi-wireless repeater system. However, a bipolar repeater system with four active plates and isolated multiple stages can serve as pure wireless repeater system.

A dynamic capacitive coupling system is demonstrated in [55]. When the secondary/receiver moves along primary/transmitter track, the output power remained within $\pm 4.0\%$ of the nominal power. The system reduced the receiver power pulsations, which in turn improves the battery lifetime. In [52], the concept of dynamic charging is

extended to railway charging application by means of high voltage ground side or overhead parallel plates. A 230 mm vehicle prototype received about 700-W power through a 24-pF coupling capacitor on a 1500 mm track.

2.3. Comparative Discussion

In this section, a comparison between inductive and capacitive AC link, based on their benefits and challenges is given. This section identifies the potential research gaps in this area and ascertains the evolution of hybrid inductive and capacitive link.

2.3.1 Frequency and Power Levels

The important standards defining the wireless power transfer system are defined in Table 2.1. They are SAE J2954, IEC 61980 part 1 and 2, ISO/AWI PAS 19363 and UL 2750 [14], [56]–[58].

Table 2-1 Relevant Standards in Wireless Charging

Standards	Description
SAE J2954	Wireless power transfer for light-duty plug-in/Electric vehicles and alignment methodology
IEC 61980	Electric vehicle wireless power transfer (WPT) systems Part 1: General requirements Part 2: Specific requirements for communication between electric road vehicle (EV) and infrastructure with respect to wireless power transfer (WPT) systems Part 3: Specific requirements for the magnetic field power transfer systems
ISO/AWI PAS 19363	Electrically propelled road vehicles - Magnetic field wireless power transfer - Safety and interoperability requirements
UL 2750	Wireless charging equipment for electric vehicles
UL 2750	Wireless charging equipment for electric vehicles

Table 2-2 Static Wireless Power Transfer (IPT) Charging - SAE J2954

WPT Levels	1	2	3	4
Frequency band (kHz)	81.39 – 90 (typical 85)			
Maximum AC input power (kVA)	3.7	7.7	11.1	22
Minimum target efficiency at nominal x, y alignment (%)	>85	>85	>85	TBD
Minimum target efficiency at offset position (%)	>80	>80	>80	TBD

For the IPT system, the SAE J2954 defines specific criteria for interoperability, electromagnetic compatibility, minimum performance, safety and testing for static wireless charging of light duty electric and plug-in electric vehicles. Following a common design guideline will ensure the interoperability of various wireless charging infrastructure among manufacturers in different nations. Table 2.2 shows power level and operating frequency standards for static wireless power transfer charging as defined in SAE J2954 technical information report [14]. The SAE J2954 standard insists the use of a single nominal frequency of 85 kHz and for systems that compensate various operating variations must achieve tuning in the frequency band as given in Table 2.2. The signaling and communication protocols between wirelessly charged electric vehicles are discussed in standards SAE J2847/6 and SAE J2931/6 [59], [60].

CPT system is recently applied to wireless EV charging in laboratory settings. Hence, power and frequency ranges have not yet been standardized.

2.3.2 Reactive Power Compensation

AC link design is incomplete without compensating for the link reactive power. To minimize the VA rating of the power supply, adequate compensation is required that will also ensure unity power factor operation of the system. The compensation networks are then selected based on the constant current or constant voltage output to address the battery charging requirements in the WPT system.

In resonant circuits, even if the system is tuned to resonant frequency or zero phase angle frequency, due to sudden parameter variations, this frequency is split into multiple resonant frequencies. This phenomenon is called bifurcation and it decreases the system voltage gain. Therefore, an important design requirement here is to make the circuit bifurcation free and it depends on the coupling coefficient and quality factor at the secondary side [32], [61], [62]. In the CPT system, the compensation circuit helps to achieve sufficient plate voltages for effective power transfer in addition to improving the coupling coefficient [63], [64]. The compensation topology adopted in some of the relevant WPT research is given in Table 2.3.

2.3.3 Efficiency

In large air-gap applications, maximum achievable efficiency is dependent on the coupling coefficient, primary and secondary quality factors and the optimum load ratio in both WPT systems. Thus, it is primarily dependent on the switching frequency of the inverter, AC link parameters and compensation circuit design. In order to increase the efficiency and power levels in a CPT system, high switching frequency operation and advanced compensation circuit design to improve the coupling capacitance for large air-gap are adopted. As the operation frequency of IPT systems is less compared to CPT

systems, with the basic compensation circuits efficiency levels greater than 90% is obtained [65].

Table 2-3 Comparison of IPT and CPT Systems

WPT Technology	Power level (kW)	Frequency (kHz)	Power Converter	Compensation Topology	Power Transistor technology	Ref.
IPT	3.6	40	Full Bridge	SS	Si MOSFET	[120]
	3.3	23	Full Bridge	SP	SiC MOSFET	[104]
	2.1	100	Full bridge	SS	GaN GIT	[105]
	7.7	79	Full Bridge	LCC	Si MOSFET	[107]
	5.6	95	Full Bridge	LCC	SiC MOSFET	[29]
	50	85	Full Bridge	SS	SiC MOSFET	[68]
	5	140	Full Bridge	SS	Hybrid SiC MOSFET & Si IGBT	[106]
CPT	1.00	200	Single active switch PWM converters	SS	SiC MOSFET	[109]
	1.00	530	Class E ²	SS	SiC MOSFET	[23]
	1.97	1000	Full Bridge	LCL	SiC MOSFET	[31]
	2.4	1000	Full Bridge	LCLC	SiC MOSFET	[64]
	1.0	1000	Full Bridge	CLC	SiC MOSFET	[30]
	0.7	2000	Half Bridge Transformer based	CLLC	SiC MOSFET	[52]
	0.557	6780	Full Bridge	LC	GaN FET	[110]
0.884	13560	Full Bridge	LC	GaN FET	[69]	

The CPT system is high voltage and low current driven circuits and hence conduction losses from coupler material are less compared to the IPT system [64]. This also means reduced heat generation, which is an added advantage in all charging applications especially in biomedical devices [66]. High frequency magnetic fields in an IPT system generates eddy current losses in the nearby metal objects which causes a significant

temperature rise in low to high power applications especially in EV charging application where power transfer is in kW range.

On the contrary, the electric field cannot create eddy currents and it penetrates through the metal objects. The inverter switching losses in the CPT system is higher due to its high switching frequency (~MHz) operation compared to the IPT system that operates in the range of 20-150 kHz.

The use of wide-bandgap semiconductor devices such as Silicon carbide, Gallium nitride with their lower gate charge and ON-resistance offers lower switching and conduction losses as compared to Silicon power transistors. The lower losses allow utilization of lightweight and inexpensive heat dissipation components. The size of compensation circuit components are also reduced owing to the higher operational frequency, however increasing the frequency above a certain limit causes switching losses. Therefore, recent WPT technologies are rapidly adopting these devices for increasing overall system efficiency and power density.

2.3.4 AC Link Power Transfer Density

The AC Link power transfer density can be enumerated as surface and volume power transfer density. The former is the power transfer per unit area (kW/m^2) and later is the power transfer per unit volume (kW/m^3). Since the thickness of both couplers is small and comparable (~2-4 mm), it is generally omitted in power transfer density calculations, resulting in only surface power transfer density measurements. However, volume power transfer density can be defined by incorporating the power transfer distance or air-gap into consideration in addition to the coupler plate area [67]. This is an important design

Table 2-4 AC Link Power Transfer Density Comparison in IPT and CPT Systems

WPT Technology	Power level (kW)	Frequency (kHz)	Coupler transmitter size (mm × mm)	DC-DC efficiency (%)	Surface power density (kW/m ²)	Air-gap (mm)	Ref.
IPT	7.7	85	500 × 500	95.2	30.8	150	[108]
	7.7	79	600 × 800	96	16	150	[107]
	50	85	410 × 760	95	160	160	[68]
CPT	2.4	1000	610 × 610 × 2 [#]	90.8	6.4	150	[64]
	0.589	6780	122.5 × 122.5 × 2 [#]	-	19.6	120	[111]
	0.884	13560	138 mm diameter circular* × 2 [#]	91.3	29.5	120	[69]
	1.125	6780	138 mm diameter circular* × 2 [#]	85	37.5	120	[70]
	1.217	7420	122.5 mm diameter circular* × 2 [#]	74.7	51.6	120	[70]

[#]Quantity * plates enveloped in 254- μ m of PTFE (polytetrafluoroethylene)

specification to evaluate the readiness of IPT and CPT system for practical applications and quantifies the compactness of a system. The best reported surface power transfer density in IPT systems is 160 kW/m² [68]. In earlier coupler designs, CPT systems' surface power transfer density values were low. This is because of the low coupling capacitance (~pF) across a power transfer distance in the range of ~100 mm and premature dielectric breakdown at the corners of the plates. Recently, CPT systems improved performance by utilizing multi-megahertz switching frequency operation accompanied with innovative compensation network and PTFE enveloped circular coupler design as employed in [69], [70]. Table 2.4 summarizes surface power transfer density comparison of IPT and CPT.

2.3.5 Voltage Stress on the Link

In IPT systems, the high frequency currents through the coupling coils generate heat and in turn losses. As the higher currents can increase the power transfer levels in an inductive link, there exists a tradeoff. Therefore, in high power application (~50 kW), forced air cooled inductive couplers are adopted [68]. Similarly, in capacitive couplers, the plate voltages need to be high enough (~1000s of volts) to establish an effective wireless power transfer.

In [71], a two-plate capacitive coupler implementation is proposed that utilizes a unipolar column interface with two active plates and two passive plates. The passive plates are vehicle chassis and earth ground. Here the voltage build-up on the vehicle chassis is proved to be limited to 8.35V in a 3 kW CPT system when the switching frequency is 6.78 MHz. Therefore, the AC link stresses can be reduced by controlling the switching frequency, improving the coupler design and optimizing the compensation topology [30].

2.3.6 Output Power Pulsation in Dynamic Wireless Charging

Dynamic wireless charging promises the quick adoption of EVs. As discussed in the previous section, the two implementations of dynamic wireless transmitters are either long track loop transmitters or short segmented transmitters. The short segmented transmitters have higher efficiency and reduced field emissions. However, the technology suffers from high power pulsations at the output during the charging process which decreases the lifespan of EV batteries [49], [72].

By buffering the incoming power pulse with a super capacitor (SC) and then feeding it to the battery pack is a popular technique to reduce the power pulsations [9], [72]. The

placing of SC directly at the EV DC bus cannot utilize the energy storage capability of the SC in contrast with the designs using a dedicated DC-DC converter that utilizes the entire voltage range of SC, but with increased component count and complexity. There also exists excessive stress on the grid at the transmitter side during the dynamic wireless power transfer. Adding an SC on the transmitter side, serves as an energy buffer and reduces harmonic currents in the AC grid. The use of SCs as energy buffers on transmitter and receiver of a dynamic wireless charging system reduced harmonic currents in AC grid as well as smoothed the battery charging current at ORNL (Oak Ridge National Laboratory) facility [9].

2.3.7 AC Link Structure

AC links must be designed not only to have excellent electrical and magnetic performance, but they also must be extremely rugged to survive the vibrations on roads in order to be integrated into the existing roadway infrastructure. In addition, they should be cost-effective, interoperable, and require minimal maintenance, to cope with the fast changing automotive technologies. Therefore, the materials used for building the AC link interface must be carefully selected, designed, tested and implemented. In inductive links, brittle and expensive ferrites are used to direct the magnetic flux and thus to boost the power transfer. In addition, aluminum plates are employed for shielding unwanted flux from the top surface of the receiver which can interact with the human body and other electronic circuitry in the vehicle. In capacitive links, the link interface is easier to be incorporated into the roadway infrastructure as its only two conductive plates usually made with aluminum or copper and the shielding is inherently provided by the passive ground plates.

A simple and cost-effective implementation of the link is the key to promote wireless charging technology for EVs extensively. In the case of IPT implementation, at high frequency (~100s of kHz), skin effect becomes prominent and expensive.

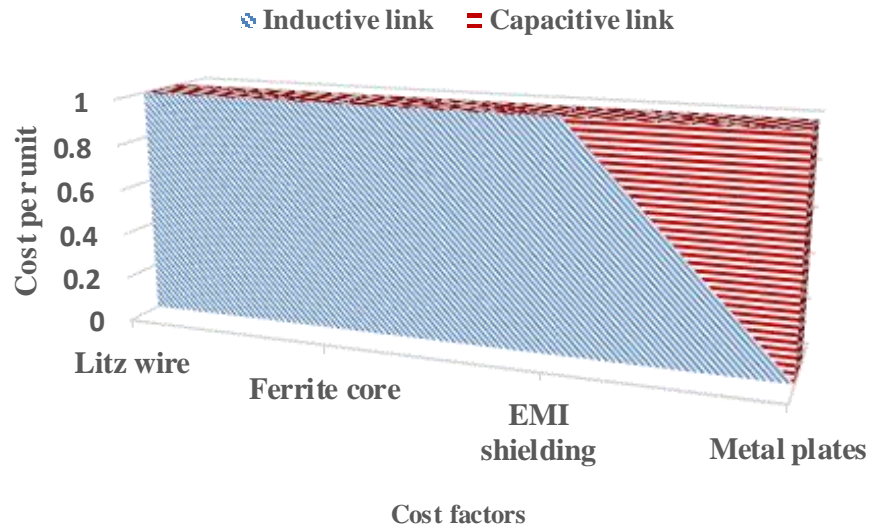


Figure 2-16 AC link construction cost factors.

Litz wire is used to build the coils to reduce this effect and further the magnetic flux is guided by bulky and costly ferrite cores. This increases the overall system weight and construction cost for the IPT system [73]. The coupling plates in the CPT system are implemented using aluminum or copper sheets of ~2 mm thickness, thus offering a simpler, low weight and cost-effective solution [24]. The energy transfer is through an electric field, which confines between the metal plates. Unlike IPT systems, the shape of the coupler was not of concern in earlier CPT designs as long as the effective area of implementation remained the same. However, recent research in [70] concluded that, poor power transfer density in large air-gap, kW scale CPT system was due to the premature dielectric

breakdown of air at the corners of square plates and the use of circular plates improved the scenario significantly as summarized in Table 2.4.

2.3.8 Link Construction Cost Factors

The construction cost of the AC link is decided by the use of specialized technological factors involved in fabricating each structure. The inductive link requires litz wire, ferrite cores, and metal shielding whereas capacitive link needs only metal plates in the transmitter-receiver assembly. In Figure 2.16, author attempt to give cost factor analysis based on the essential resources to manufacture these links. Here, the cost involved per material is considered as unit cost on Y axis in order to simplify the representation. The cost factors involved for link design are three times more for IPT link compared to CPT link.

2.3.9 Misalignment Tolerance

Table 2-5 Misalignment Performance Comparison in IPT and CPT Systems

WPT Technology	Power level (kW)	Coupler size (mm × mm)	Maximum DC-DC efficiency achieved (%)	Horizontal Misalignment (mm)	Efficiency at horizontal misalignment (%)	Ref.
IPT	3.5	450 × 450	95	150 in X direction	56	[76]
				150 in Y direction	82.6	
CPT	2.4	610 × 610	90.8	300	89.4	[64]
IPT	2.16	300 × 90	94.89	200	38.5	
HPT	0.84	610 × 610	93.04	200	80.2	[94]
		CPT (o)* 457 × 457 (i)				

*The CPT coupler is in 4X1 column arrangement (o)-outer plate (i)-inner plate

The power transfer efficiency is dependent on the relative positions of the transmitter and receiver of a WPT system. Thus, power transfer decreases with the horizontal or

vertical misalignment as pointed out in section 2.1. That means in an EV charging scenario, different ground clearance or misaligned parking of the vehicle causes lower power transfer, reduced efficiency and prolonged charging time. Therefore, an improved coupler design along with enhanced compensation circuit topology can give high tolerance to misalignment and ground clearance variations [74]–[76]. Table 2.5 reveals CPT system has better misalignment tolerance than IPT system. For the comparable dimensions and misalignment distance, power transfer in the CPT system is 33% more than the IPT system. This result is very important in EV charging application where misalignment of primary and secondary circuits are unavoidable.

2.3.10 Interoperability of Couplers

When the WPT systems are commercialized, the charging pads or couplers of various shapes must be compatible to each other. In IPT systems, the polarized DDQ and bipolar pads are interoperable with other pad types as they generate both horizontal and vertical components of flux. In [36], it was found that the DD-DDQ pad interface could achieve higher coupling and a five times larger coverage zone for charging compared to circular pad system. This interface does not have any net zero flux or null region. The bipolar pads are operated as non-polarized or polarized depending on the phase excitation of its coils. However, the non-polarized pad designs exhibited low coupling coefficient during interoperability [77]. The CPT couplers are metal plates and it is not affected by any charging pad compatibility issues. The coupling efficiency is only related to the total overlap area of the conductive plates.

2.3.11 EMF Exposure Limits

Table 2-6 Maximum Permissible Exposure to Electric Field IEEE C95.1, 2005

Frequency range (MHz)	<i>E</i> (RMS) (V/m)	
	General public	Persons in controlled environments
0.1-1.34	614	1842
1.34-30	823.8/f _{MHZ}	1842/f _{MHZ}

If the couplers are very close (less than 1 mm), the electric field in CPT are confined within the area enclosed and the leakage field is negligible in the surroundings. The slight presence of leakage flux in IPT systems in close coupling application can also be handled effortlessly depending on the shape of the coils, presence of ferrite or by shielding. However, for EV charging application, as the coupling distance is larger (100 mm-200 mm), the radiations are significant and must be effectively shielded. The shielding is achieved in a CPT system through proper grounding unlike the metal shielding infrastructure needed in the IPT system.

The ICNIRP 2010 guidelines and IEEE C95.1, 2005 (amended in 2019) standard have set the limits of maximum permissible exposure, which should be monitored while designing and testing the wireless power transfer systems and are given in Table 2.6 and 2.7 [78]–[80]. Therefore, adverse safety effects of electromagnetic radiations emitted from

Table 2-7 EMF Exposure Reference Levels - ICNIRP, 2010

Entity	RMS level	Peak level
Magnetic field	27 μ T or 21.4 A/m	38.2 μ T or 30.4 A/m
Contact current	17 mA @ 85 kHz	24 mA @ 85 kHz

the link to the surroundings need to be controlled by observing the standards and shielding techniques [81]–[83].

2.3.12 Foreign Object Interaction in the Link Proximity

The foreign body interaction can be defined as the proximity of living and metal objects in and around the link. Any interference of objects in between the wireless link can be critical as it causes heating of the conductive objects apart from affecting the power transfer. The magnetic fields from the inductive coupler cause eddy currents in metallic debris, but electric fields penetrate through it. The ability of electric field to penetrate metal objects enables the CPT to be installed in an environment with metal surroundings especially in electric locomotives used in mines.

A recent study in [84] validated the impact of foreign objects metal, wood, plastic and water on the performance of CPT systems and concluded that the performance degradation is prominent only when the presence of object is in less than 3 cm from the coupling plates which causes the system to deviate from the resonant frequency. The study evaluated two methods to retune the system, first, by adjusting the operating frequency, which is not recommended for multi-MHz CPT systems and second by providing required reactance to

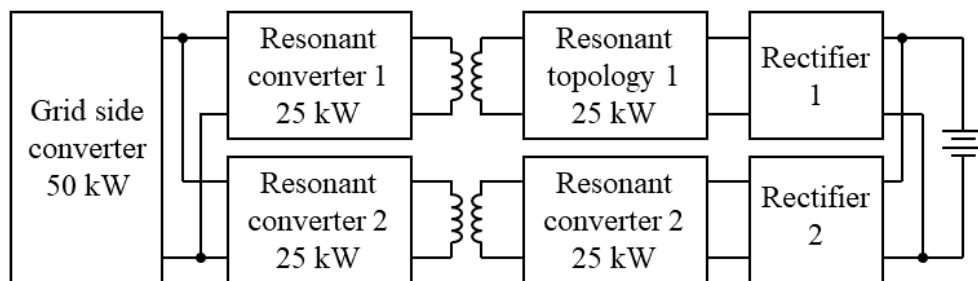


Figure 2-17 50 kW modular charger prototype for IPT

retune the system through active variable reactance (AVR) rectifier that operates at a fixed frequency. Several research on living and metal object detection techniques focused to energize the primary transmitter only when the link is free of foreign objects if any [85]–[87].

2.3.13 Power Scaling

As the WPT technology progresses, researchers are also focusing on scaling up the power transfer capabilities which is already offered by wired chargers [88]. A 120 kW DC fast charger can recharge an EV with battery capacity 30 kWh in 15 minutes. For light-duty EVs, the maximum defined WPT power level standard is class 4 (22 kVA). Therefore, power scaling allows for a reduced recharging time in static wireless chargers and an essential feature for deploying dynamic WPT systems.

In [89], a 22 kW WPT system design using DD couplers with SS compensation is reported where the preliminary results with a downgraded power level of 5 kW achieved 95% efficiency. The Unplugged project in [90] portrays the development of a 50 kW inductive coupler design and control using a modular charger as depicted in Figure 2.17. This reduces the current stress on the link and makes the IPT system resilient. The capacitive couplers are still in the initial stage of development and the experimental prototypes built are scaled only up to WPT power class 1 (3.6 kVA).

2.4. Hybrid Inductive and Capacitive AC Link – New Trend

The concept of shared power transfer can utilize the available magnetic and electric fields to form a single system with hybrid inductive and capacitive AC link [91]. In [92], [93] several integrated combinations are discussed for transferring power and data simultaneously. A relative discussion of inductive and capacitive AC links in the previous

section revealed this imminent trend of hybridizing the AC link for reliable and efficient wireless power transfer, as summarized in Figure 2.18, where the radar values are ascending away from the center. Since the factors listed in the figure are measured differently, in order to generalize the influence of these factors on IPT, CPT and existing HPT systems, they are given values from 1 (lowest) to 5 (highest). For example, the factor ‘frequency’ has lower value (kHz) for IPT compared to CPT and existing HPT (~MHz). Similarly, the cost factors involved in IPT is higher than CPT and so on. Thus, by combining the merits of IPT and CPT, HPT system can have better power scaling capability, reduced compensation elements, higher link power transfer density, less pad compatibility issues, and improved misalignment tolerance.

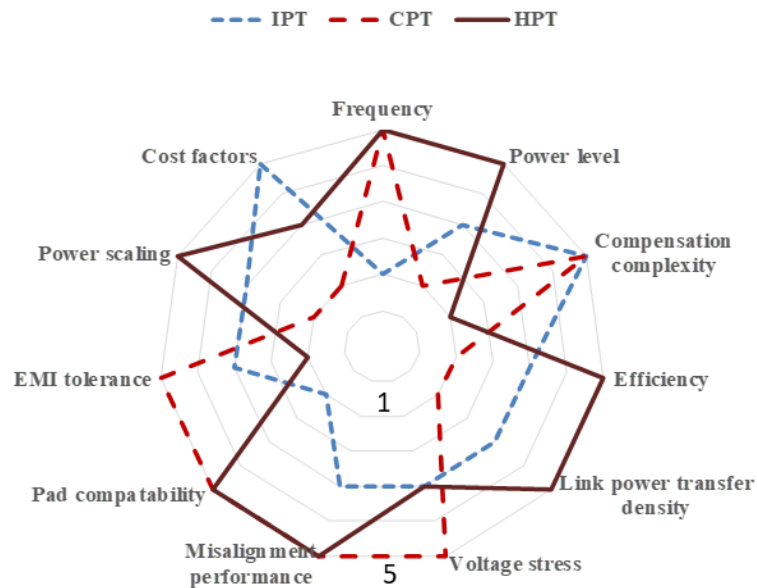


Figure 2-18 Relative analysis plot of IPT, CPT and HPT. (The radar graph is ascending away from the center giving lowest (1) to highest (5) values for each factors listed)

2.4.1 Existing Hybrid Inductive and Capacitive Power Transfer Topologies

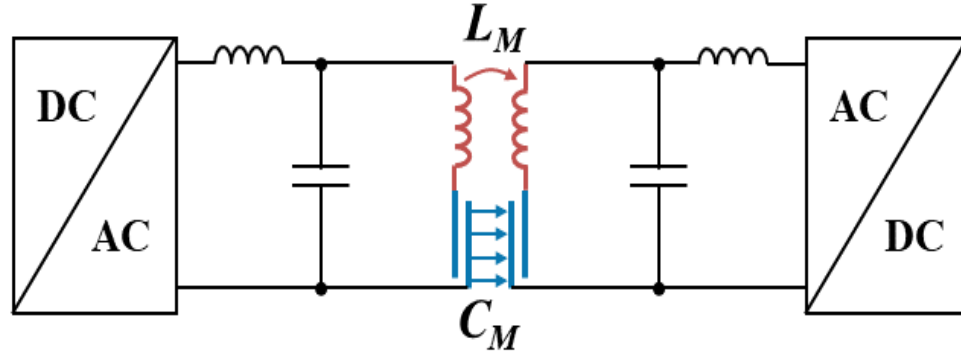


Figure 2-19 DC-DC stage of combined inductive and capacitive link proposed in [94].

A 3.0 kW combined IPT-CPT system proposed in [94] provided a means to stimulate the evolution of the CPT system, Figure 2.19. Here, the capacitive link is connected in series with the inductive link and operated at 1 MHz switching frequency. The combination offered a choice of power management between IPT and CPT. However, the high frequency switching currents through inductive link increases undesirable magnetic field emissions to the surroundings [95]. This topology has achieved 94.45% efficiency with an IPT to CPT power ratio of 2.5.

Table 2-8 Prospective HPT Lab Prototypes for Wireless EV Charging

WPT Technology	Power level (kW)	Frequency (kHz)	Power transfer percentage (%)	Maximum DC-DC efficiency achieved (%)	Coupler transmitter size (mm × mm)	Air-gap (mm)	Distance between IPT-CPT coupler (mm)	Ref.
HPT $\frac{\text{IPT}}{\text{CPT}}$	3	1000	$\frac{72}{28}$	94.45	$\frac{300 \times 90}{610 \times 610}$	150	300	[94]
HPT $\frac{\text{IPT}}{\text{CPT}}$	1.1	800	~50	91.9	$\frac{300 \times 300}{500 \times 500}$	150	300	[97]

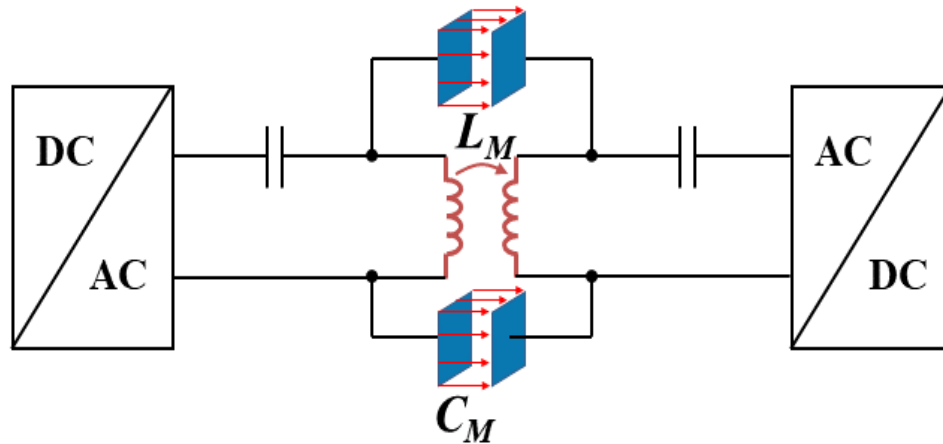


Figure 2-20 DC-DC stage of hybrid inductive and capacitive link proposed in [96].

In [96], an integrated inductive and capacitive coupler is implemented where the coils of the IPT system also acts as plates of the CPT system and vice versa. The power ratio of IPT and CPT system is proportional to the ratio of inductive and capacitive coupling coefficients of the integrated system. A 100 W prototype achieved 73% efficiency at 1 MHz switching frequency. This integrated coupler design can potentially improve the power transfer density of the system, eliminate external compensation circuit and reduce magnetic field emissions by the shielding effect from plates.

Another hybrid system, a 1.1 kW lab prototype proposed in [97] reported a 91.9% DC-DC efficiency, Figure 2.20. The placement of capacitive link with the inductive link utilizes the high voltage stress in coils for the power transfer. This hybrid AC link provided twice the power transfer capability compared to individual inductive and capacitive link with the same coil currents and plate voltages. The system operating frequency is 800 kHz, which is still much higher for an inductive coupler implementation. Therefore, the future research focus will be on hybrid designs with reduced switching frequency operation of inductive coupler without affecting the power transfer capability of capacitive couplers.

Table 2.8 summarizes prospective lab prototypes of HPT system applicable to wireless EV charging from the literature.

2.4.2 Future developments

From the above discussions, it is clear that the combined operation of inductive and capacitive link can ensure cost effective, scalable and reliable implementation of wireless chargers for electric vehicles. The implications of existing systems and directions for further enhancing the HPT system are listed below and summarized in Table 2.9.

Table 2-9 HPT Configurations for Wireless EV Charging

HPT technology	System frequency	Air-gap (mm)	Inverter architecture	Power scalability	WPT system architecture	WPT link reliability
Dependent two-channel power transfer I	~MHz	100-200	Full bridge	Complex	Integrated	Low
Dependent two-channel power transfer II	~kHz	IPT ~ 100-200 CPT ~ 10-20	Full bridge	Complex	Integrated	Low
Independent two-channel power transfer	IPT ~ kHz CPT ~ MHz	IPT ~ 100-200 CPT 100-200	Three leg	Simple	Modular	High

2.4.2.1 Dependent Two-channel Power Transfer at High Frequency

The existing research listed in Table 2.8 focused on creating a combined resonant tank for the mutual operation of both links creating a dependent two channel power transfer through coupling coils and coupling plates. Here, apart from contributing to power transfer, coupling coils also provides the required compensation inductance for the capacitive power transfer. Similarly, in addition to power transfer function, coupling plates also works as capacitors resonating with coils. Moreover, the high voltage stress in the coils can be

utilized as driving voltages for the coupling plates. However, the drawback of this method is the dependency of inductive and capacitive links that accounts for operating the whole HPT system at high frequency (800 kHz - 1 MHz). This is far beyond the standard frequency band of inductive couplers utilized for EV charging.

2.4.2.2 Dependent Two-channel Power Transfer at Medium Frequency

The need for high frequency (~1MHz) operation in the existing HPT links is for compensating the low coupling capacitance in the capacitive link when operated in large air-gap, especially in EV applications where the receiver is mounted on the chassis as discussed in section 2.2. The capacitive link air-gap can be reduced by placing it at the front or rear ends of the EV instead of keeping it underneath the vehicle. In this case, the effective coupling capacitance is in the range of nano farads and the frequency of operation can be kept at hundreds of kHz to reduce the reactance. Furthermore, introducing dielectrics in the above coupler arrangement where the air-gap is in the order of several millimeters, further increase the coupling capacitance and reduce the operating frequency (~200 kHz). Therefore, the entire HPT link can be operated at medium frequency levels which is acceptable to inductive coupler frequency standards.

2.4.2.3 Independent Two-channel Power Transfer with Modular Architecture

For the independent operation of inductive and capacitive links that can be switched at different frequencies, modular inverter architecture is a viable and simple solution. In previous designs, the links were combined in series and the circuit design required to consider the mutual effects of parameters making the design complex. Here, the inductive link is operated at low frequency and capacitive link at high frequency, creating two independent resonant tanks in parallel supplying power to the load. This modular

architecture will provide a flexible operation of the links and increases the reliability and scalability of the hybrid system.

Chapter 3. Study of CPT interface for low to medium power EV charging applications

3.1 Prospects of Capacitive Wireless Power Transfer (CPT) for Unmanned Aerial Vehicles

The unmanned aerial vehicle (UAV) or drone is an aircraft without a human pilot aboard. UAVs are a part of an unmanned aircraft system (UAS). UAS comprises of a UAV, a ground-based controller, and a system that communicates between the two [98]. UAVs originated in military application; however, their use expanded to commercial, scientific, agricultural and recreational applications rapidly. They have limited area and can carry only a few kilograms of weight. Therefore their battery weight and power density cannot be higher, thus it can only fly for 20-30 minutes with full recharge. Hence, flight autonomy is limited for drones and here wireless charging finds a role to play. This will reduce the human intervention to replace or recharge the drone batteries. To increase the flight time, equipping the UAV with a higher battery capacity is an option. However, this additional weight leads to considering the reduction of the payload, which comprises of global positioning system (GPS), geographic information system (GIS), high-resolution cameras, sensors etc. Another approach is to create base stations where drones will land and get recharged wirelessly [99].

In reference [99], authors gives a scheme for resonant inductive wireless charging of drones for an output power target of 62.5 watts via circular coupling coils and analyzed the electromagnetic interference (EMI) compatibility and misalignment performance. Here the receiving coil is onboard and without ferrite blocks to reduce the overall weight of the

system. However, during misalignment, the magnetic field can penetrate through the non-conductive parts and destroy engine components. In order to improve the coupling coefficient, another approach is adopted in [100] where receiving coil is mounted on landing support and the transmitter is a 3x2 primary coil loop array. This system provided a maximum efficiency of 93% and an average efficiency of 85% at any point in the charging loop.

In near field wireless power transfer, electrostatic coupling based capacitive wireless power transfer (CPT) systems are gradually proving their paybacks over electromagnetically coupled inductive wireless power transfer (IPT) system. Firstly, the electromagnetic interference to nearby electronic circuits is negligible. This in turn reduces the EMI shielding expenses for drone's electronic circuitry. Secondly, to reduce the skin effect and leakage flux, IPT system has to use expensive Litz wire and ferrite material combinations. Therefore making the overall system cost and weight higher compared to the low cost, less bulky alternative achievable through CPT.

3.1.1 Design methodology

A conceptual system architecture is as given in Figure 3.1. Here a master drone, will act as a transmitter. The receiver or slave drones will hover over it and are recharged wirelessly through capacitive coupling. Therefore, receiver drones need not land for charging as it is recharged over air via a master drone that can reach it from a base station. Authors assume that dedicated wireless communication takes place among drones and base station,

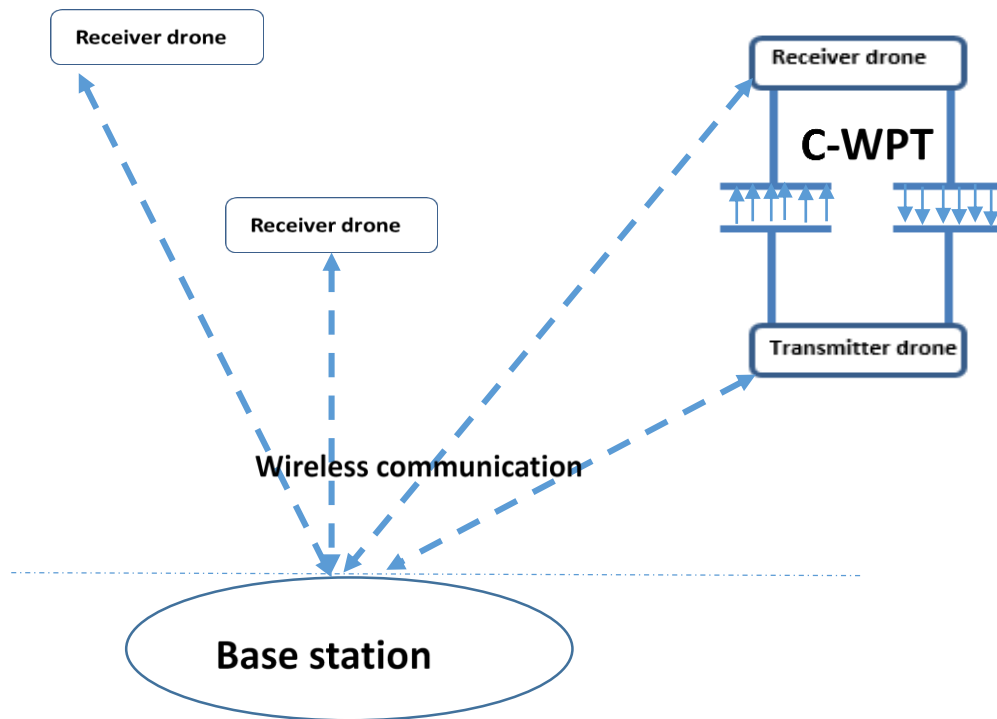


Figure 3-1 CPT based in motion charging scenario for UAVs

concerning the state of charge of batteries, location, speed etc. This recharging option saves time and increases flight autonomy. Typical power requirement of slave drones is approximately 100-150 watts for 30 minutes of flying time. Table 3.1 summarizes some of the commercial drone specifications. The capacitive transmitter plate pair will be mounted on the top surface of the master drone and the receiver plate pair on the base of slave drones. In this approach, wireless power transfer is triggered only when master and slave drones are completely aligned and travelling at the same speed. This in fact emulates a standstill wireless charging behavior at an air gap or power transfer distance in the range of 100 mm to 150 mm. Another approach is to interlock the transmitter and receiver drone interface mechanically allowing only negligible air gap of less than 20 mm, before activating the wireless power transfer.

Table 3-1 Examples of various capacity drones

Specifications	DJI AGRAS MG-1	FREEFLY ALTA 8	DJI S1000	DJI F550
Max. Payload (kg)	9	10	6.8	0.5
Flight time (min.)	24	16	15	10
Battery Capacity (Wh)	533	444	222	72
Mass (kg)	8.8	6.2	4.4	3.5

The design methodology is as follows.

1. Decide the power levels of transmitter and receiver drones depending on recharging time. For example, let the receiver drone be DJIF550 with a lithium polymer (LiPo) battery of nominal voltage 14.4 V and capacity 5000 mAh. Power required from the transmitter drone to recharge it in one hour is 72 W. In fact, any higher power capacity transmitter drones can deliver power to the lower capacity receiver drones. However, for mid-air charging, the flight time is important as the transmitter drone needs to return to the base station for replenishing itself. Therefore, for instance, for a fast recharge in 10 minutes, minimum energy required to be delivered from the transmitter drone battery is 432 Wh at a 6C rate to fully recharge the 72Wh receiver drone battery. Therefore, from the table 3.1, the first two drones can be a transmitter drone for the receiver DJIF550.

2. Determine the compensation topology and calculate the passive components for the desired resonant frequency. Typical range is in tens of MHz. This frequency selection will reduce the size of passive components, which in turn reduces the overall weight of the system.
3. Once the electrical parameters are finalized, decide upon the coupling geometry and interface based on the UAV dimensions. Here, the objectives are to achieve lightweight and misalignment tolerant interface.

3.2 Coupler Interface design

The parallel plates at the coupling interface can be arranged in row, column and symmetric forming four plate structures, combined column and symmetric configuration forming six plate structure and asymmetric matrix configuration as given in Figure 3.2. From the linear algebra, in an $m \times n$ (row \times column) matrix, the $1 \times n$ arrangement is termed as a row matrix and $m \times 1$ as a column matrix, Figure 3.2 (a) and (b). Here, to define the capacitive coupling interface similar analogy is used. The symmetric matrix is formed when primary and secondary have an equal number of plates as in Figure 3-2 (c) two plates at primary and two plates at secondary to form 2×2 configuration.

In [31] this configuration is modified into a six plate coupler structure by incorporating roadway and vehicle chassis as additional plates to shield the electric field at transmitter and receiver sides respectively which also improved the performance of the system as given in Figure 3.4(d).

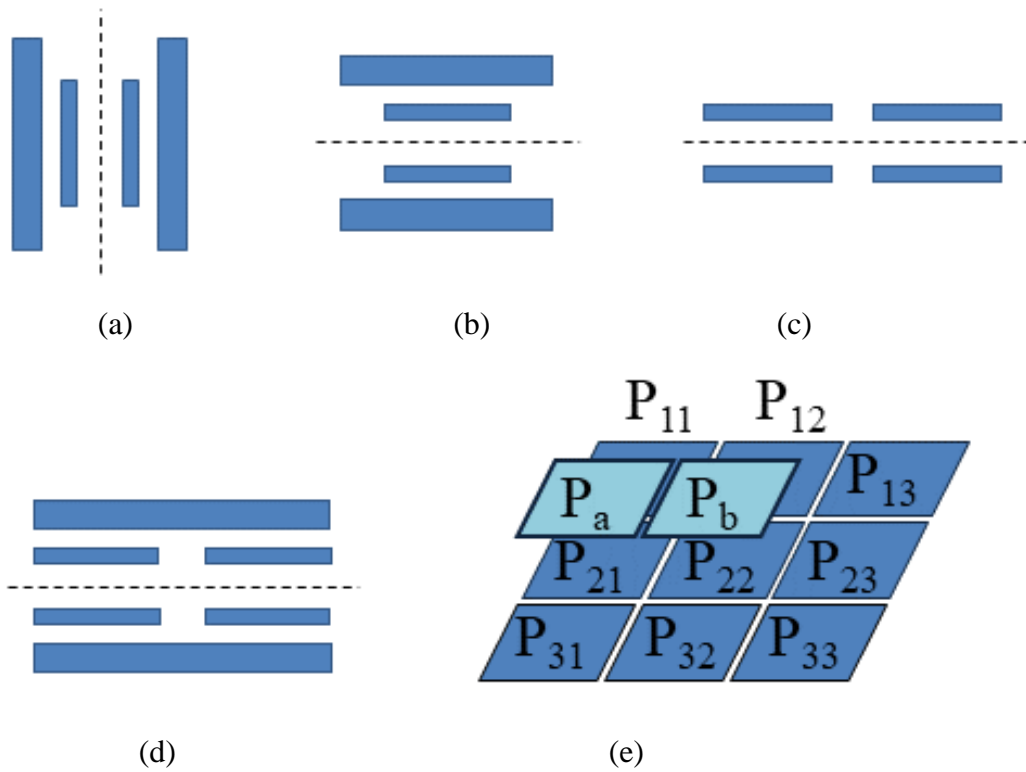


Figure 3-2 Coupling interface. (a) 1x4 row. (b) 4x1 column. (c) 2 x 2 symmetric matrix. (d) Six plate combined structure. (e) Asymmetric matrix.

In asymmetric matrix Figure 3.4 (e), the primary plates alone form a 3x3 matrix charging pad and the secondary consists of only two plates. This asymmetric matrix structure has a higher misalignment performance than all other configurations due to the fact that the coupling coefficient never drops to zero, as the primary plate area is much larger than secondary plates.

3.3 Low power interface for UAVs

The selection of coupling geometry and interface configuration is based on the mutual coupling capacitance, voltage gain and design simplicity. In Figure 3.3, two types of parallel plate capacitive couplers are shown. The coupling capacitance of type I and type

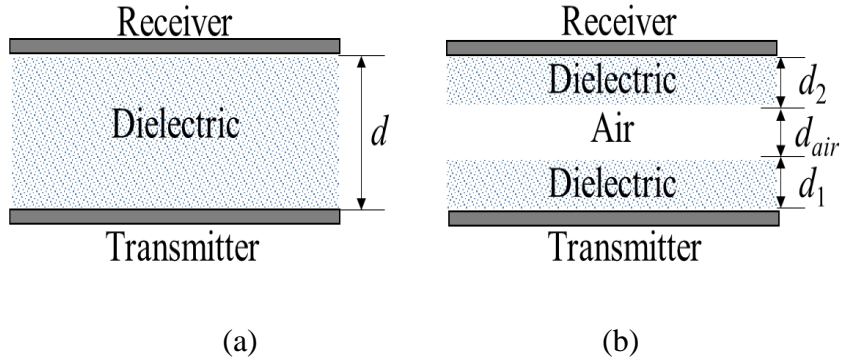


Figure 3-3 Parallel plate capacitive couplers (a) With single dielectric-Type I
(b)With multiple dielectrics- Type II.

II are given in (3.1) and (3.2) respectively. Here, in equation (3.1), A is the area of plates, d is the distance between the plates, ϵ_0 is the permittivity of free space; ϵ_r corresponds to the relative permittivity of the dielectric material used if any (for air ϵ_r is one), as in Figure 3.3 (a). When multiple dielectrics are used such as a coating on transmitter and receiver plates, as given in Figure 3.3 (b), with the dielectric thickness d_1 , d_2 and air-gap, d_{air} the equation (3.2) is obtained.

$$C = \epsilon_0 \epsilon_r A / d \quad (3.1)$$

$$C = A / [(d_1 + d_2) / \epsilon_0 \epsilon_r + d_{air} / \epsilon_0] \quad (3.2)$$

Once the geometry is decided to be parallel plate, the arrangement of plates in coupling interface can be either row, column or matrix as given in Figure 3.4. The row interface depicted in Figure 3.4 (a) is applicable if the plates are mounted on the front end for a face to face electric coupling.

3.3.1 Design and simulation

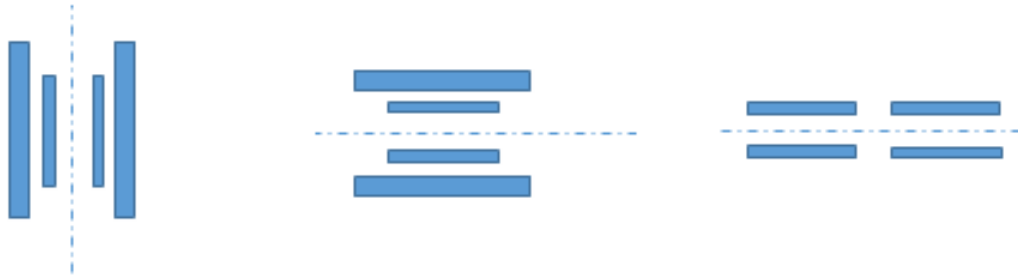
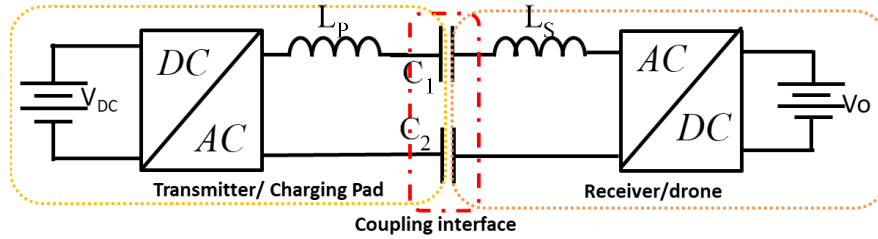


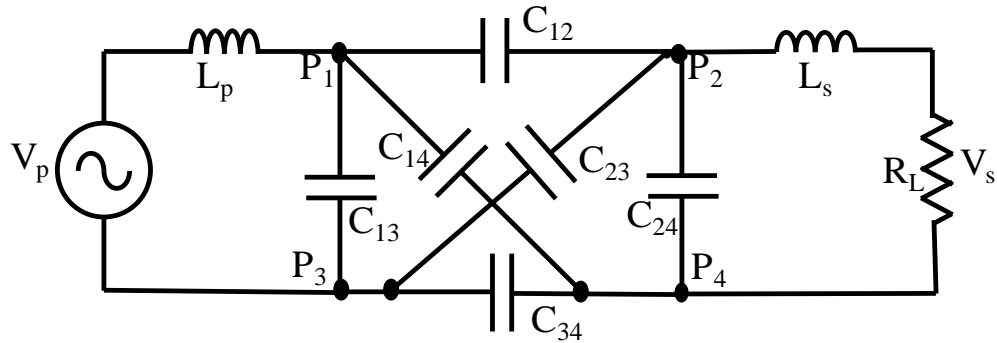
Figure 3-4 Coupling interface (a) 1x4 Row (b) 4x1 Column (c) 2 x 2 Matrix

The capacitive link interface selected are row, column and matrix arrangement. The 1x4 row and 4x1 column interface have the outer plate dimension 150 mm x 170 mm and inner plate dimensions 120 mm x 120 mm. As discussed, here the difference in these structures is only in their orientation that is suitable for implementation. Therefore, only 4x1 column interface is simulated. In the 2x2-matrix interface arrangement, all plates are of equal size, 150 mm x 170 mm.

The component count in compensation network is critical as it can increase the overall weight of a UAV where every gram counts. Therefore a series compensated topology [22] is the low cost and light weight implementation and thus selected. The simplified block diagram for a series compensated CPT for drone charging application is given in Figure 3.5(a) and the equivalent circuit in Figure 3.5(b). The voltage and power levels are selected



(a)



(b)

Figure 3-5 (a) Block diagram for a series compensated CPT driving UAVs (b) Equivalent circuit.

according to drone battery capacity and nominal voltage ratings, from the manufacturer. The electrical parameters are calculated for the battery requirements of the drone, for a power level of 80 W and are listed in Table 3.2 with reference to the equivalent circuit given in Figure 3.5 (b). The input voltage at the primary side of the link is 15.5 V and the output voltage at the secondary side of the link is 14.4 V.

The 2x2 matrix arrangement with plate dimensions 150 mm x 170 mm and a minimum air-gap of 20 mm that accounts for the interlocked transmitter and receiver drones. The corresponding capacitance across the plates is 11.3 pF. Therefore, the compensation inductor can be designed from the relation (3.3), after deciding the frequency of operation (f_0).

$$f_0 = \frac{1}{2\pi\sqrt{L_p C_1}} = \frac{1}{2\pi\sqrt{L_s C_2}} \quad (3.3)$$

Table 3-2 Circuit Parameters for 150 mm x 170 mm matrix interface at 20 mm air-gap

Parameters	Values
f_0	10 MHz
P_0	80 W
$V_{P(RMS)}$	15.5 V
$V_{S(RMS)}$	14.4 V
$L_P (L_S)$	22.4 μ H
$C_1 (C_2)$	11.3 pF

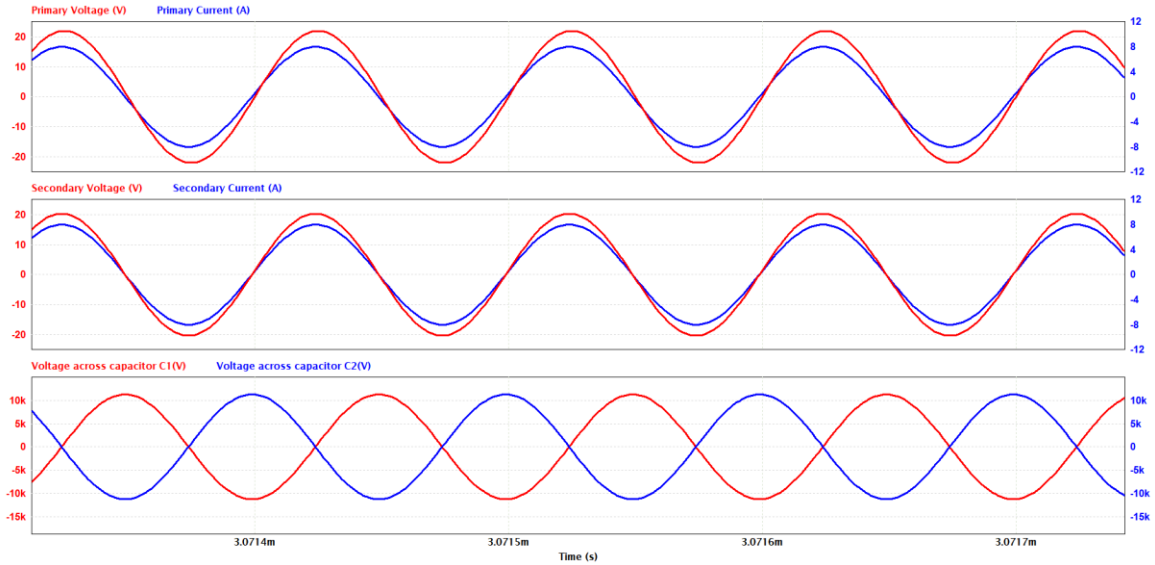


Figure 3-6 Simulation results in PSIM for matrix interface.

The designed series compensated topology is simulated in PSIM and the input and output voltage waveforms along with the voltage across the capacitive link is given in Figure 3.6. The rms voltage across the coupling plates is measured as 7.8 kV. Since the distance across the plates is 20 mm, the electric field developed is 396 V/mm, which is

much less than the breakdown voltage of air (3 kV/mm) and therefore there is no concern of arcing across the plates.

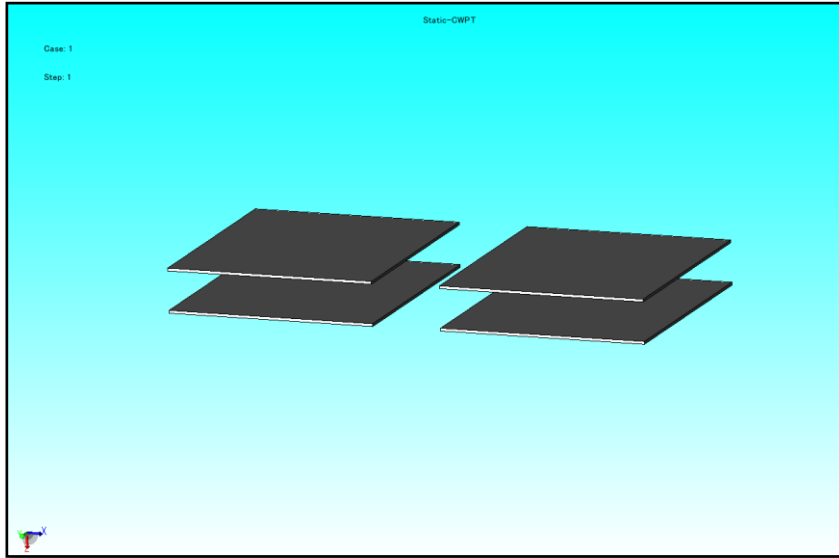


Figure 3-7 2x2 matrix interface.

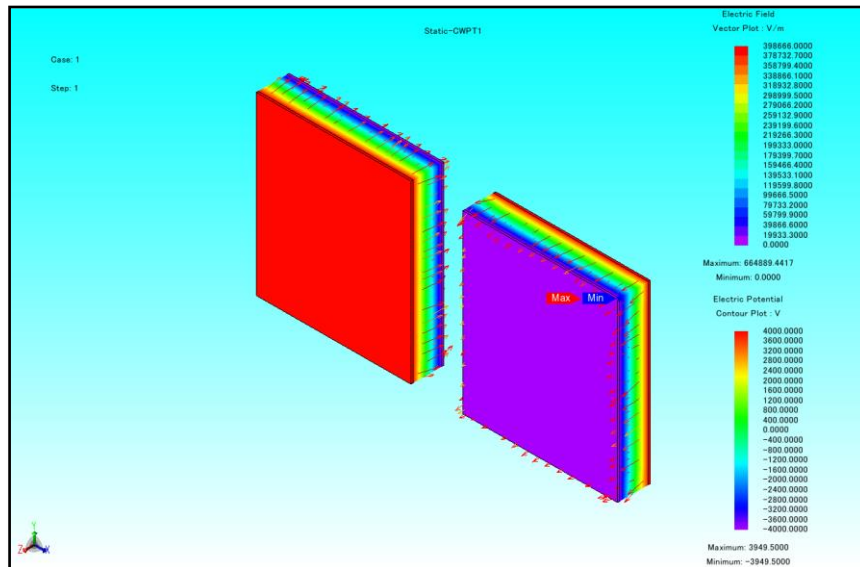


Figure 3-8 2x2 matrix interface with potential and field distribution.

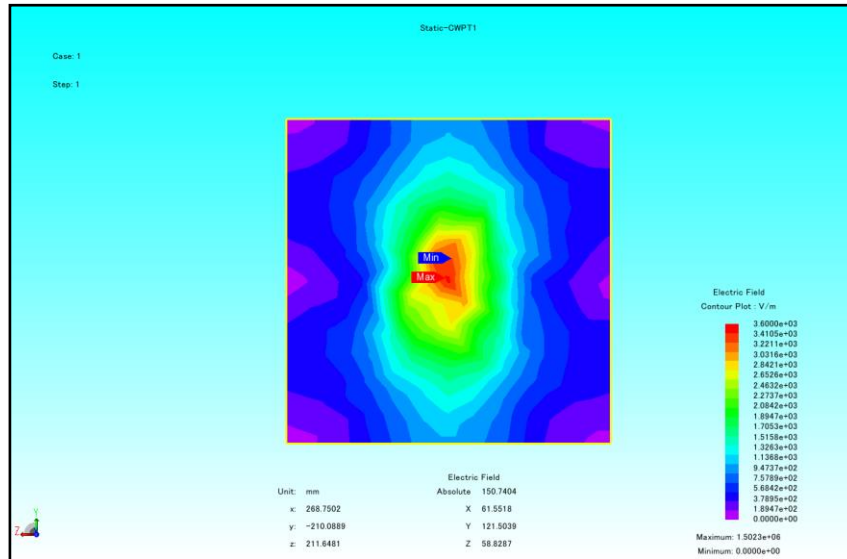


Figure 3-9 Electric field distribution including the surrounding air region in 2x2 matrix arrangement.

The 2x2 matrix arrangement is modelled using JMAG geometry editor (see Figure 3.7). After setting the measured potential across the plates, the mutual capacitance is verified from the surface charge obtained in FEA analysis and the applied potential difference across the plates as shown in Figure 3.8.

The electric field distribution observed is given in Figure 3.9. The absolute electric field obtained at a distance of 211 mm from the plates is 150.7 V/m which is within the IEEE C95.1 limits.

Similarly the 4x1 column interface is modelled in JMAG geometry editor with the outer plate dimension 150 mm x 170 mm and inner plate dimensions 120 mm x 120 mm (see Figure 3.10) and the mutual capacitance is verified as discussed by applying the electric potential across the plates, as given in Figure 3.11. The electric field distribution of the column interface surrounded by the air region is given in Figure 3.12.

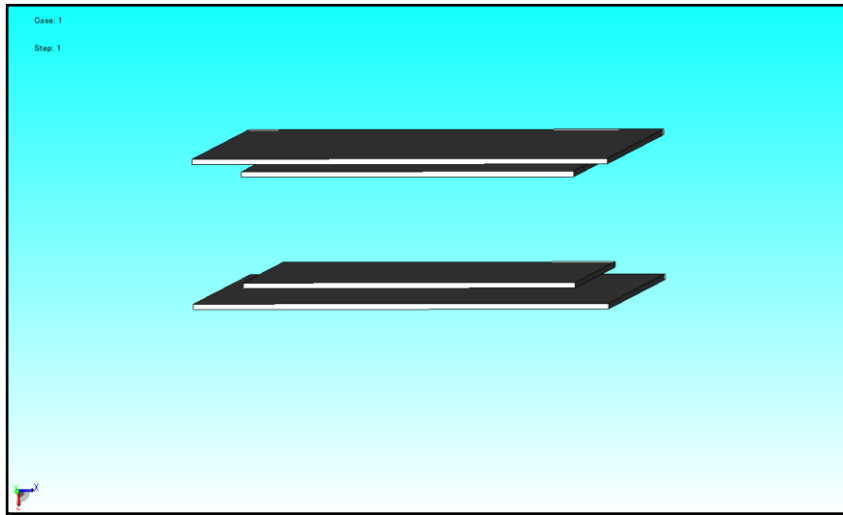


Figure 3-10 4x1 column interface.

As it can be seen, the minimum field measurement of 1578 V/m is observed at around 105 mm from the center. The plate pair coupling capacitances obtained for matrix and column interface are given in Table 3.3.

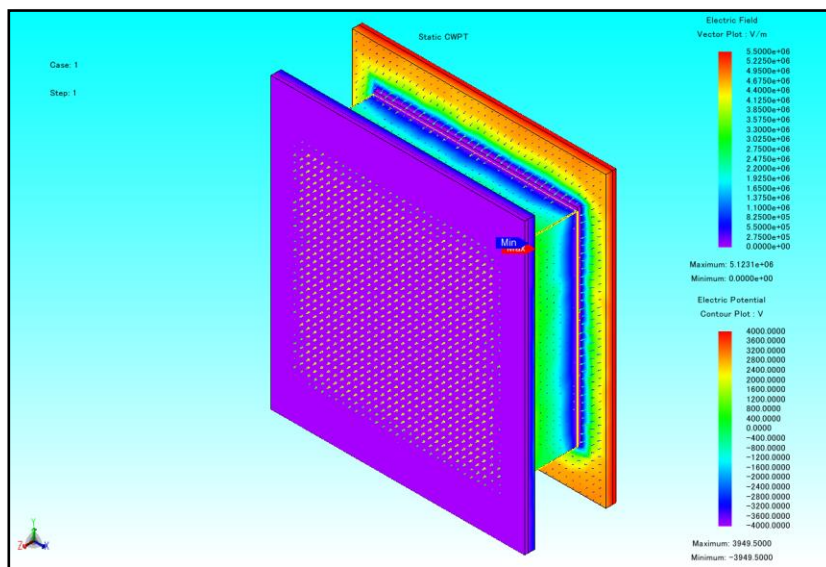


Figure 3-11 4x1 column interface with potential and field distribution.

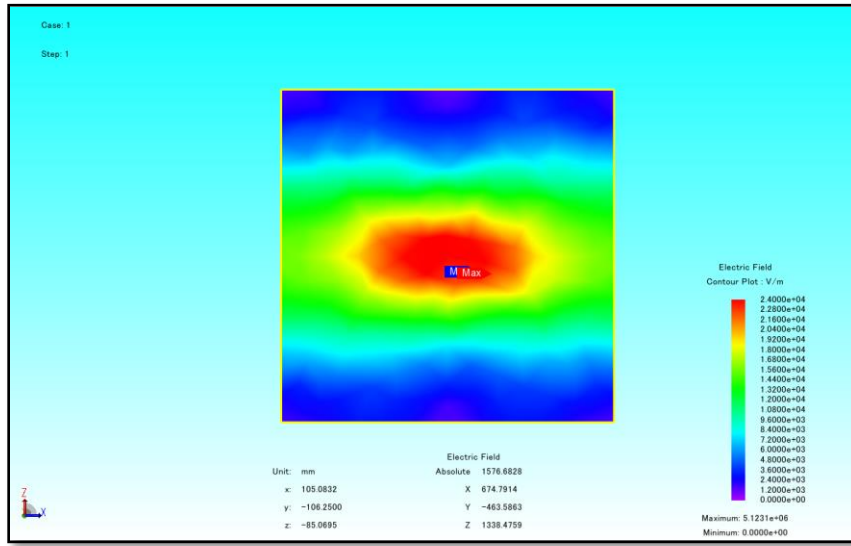


Figure 3-12 Electric field distribution including the surrounding air region in 4x1 column arrangement.

Table 3-3 Coupler interface parameters

Coupler interface	Plates	Dimension (mm)	Plate capacitance (pF)
Matrix	4	150x170	11.3
Column	4	120x120 (Inner pair)	6.9

Both column and matrix arrangement can achieve surface to base coupling. The column interface is more compact and misalignment tolerant in the horizontal direction. This is because the mismatch between primary and secondary plates in the matrix structure reduces the output power, but in column interface for the same misalignment in the horizontal plane, effective capacitance remains unchanged as it is mainly contributed by the same side plate pair. For the variations in the vertical power transfer distance or air-gap, matrix configuration is more tolerant than the column configuration due to larger coupling area.

The matrix interface provided a higher mutual capacitance at an air-gap of 20 mm. The row/column interface provides a compact capacitive wireless charging solution at the cost of mutual capacitance. This corresponds to the scenario where transmitter and receiver interlocks mechanically. For analyzing the scenario where a standstill behavior is emulated by achieving same speed for master and slave drones, the air gap is increased to 120 mm and found that the mutual capacitance is reduced by 45%.

Another inference from this study is that with air alone as the dielectric, mutual capacitance obtained is very less in low power and large air-gap interfaces. Thus reducing the overall efficiency of the system. In order to increase the mutual capacitance, the plate area needs to be extended significantly. However, this is not possible here due to the limited drone dimensions. The desired mutual capacitance for the given plate area can be increased by the use of high permittivity dielectrics which can also improve the breakdown electric field, thus reducing the possibility of a dielectric breakdown.

3.4 High power interface and influence of dielectrics

The power transferred through the coupler/link, $P_{coupler}$ can be formulated as (3.4) where ω is the angular switching frequency, C_m is the mutual capacitance, V_1 and V_2 are the link voltages across C_1 and C_2 of the CPT system. Therefore, as the mutual capacitance increases, the power transferred across the coupler will be higher.

$$P_{coupler} = \omega C_M V_1 V_2 \quad (3.4)$$

The capacitance values are first calculated based on the plate dimensions, permittivity of the selected material and power transfer distance. The transmitter and receiver plates are

of the size $600 \times 600 \text{ mm}^2$ and thickness 1 mm . The distance between the transmitter and receiver is 80 mm . The gap is filled with the low to high permittivity dielectric materials namely air, silicon, titanium dioxide (Ceramic class 1) and barium titanate (Ceramic class 2) in each case. The properties of these materials are listed in Table 3.4.

From (3.2), the effect of the dielectric constant is minimal on the value of capacitance when the air-gap area is greater than the dielectric thickness. Therefore, for large air-gap (100 mm - 200 mm) application, air is the preferred dielectric. On the other hand in case of conformal bumper EV charging as proposed in [23], where face to face close coupling is possible, the air gap is negligible and use of dielectric coating is advantageous.

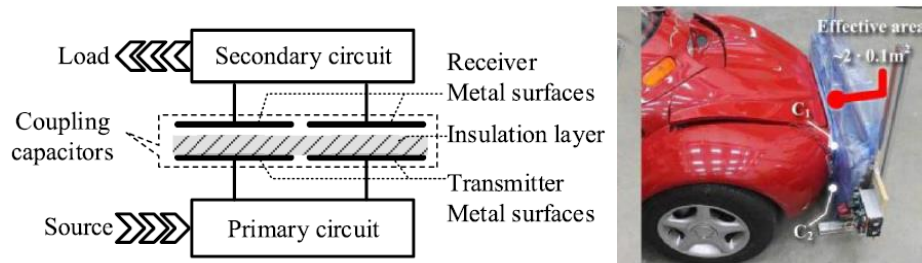


Figure 3-13 Conformal bumper arrangement [23].

A large air-gap or separation distance introduces edge effect due to fringing fields and the capacitance estimation is inaccurate with (3.1),(3.2). In [101], the capacitance is estimated using the Schwartz-Christoffel transformation, making it possible to map the entire electric field. Another approach is using the boundary element method that utilizes the Laplace electrostatic equation to find the edge effect [102]. It also defines an aspect ratio (b) for rectangular, square and disk type structures as given in Table 3.5. The fringing field cannot be neglected for aspect ratio greater than or equal to one. The actual

capacitance including the edge effect can be found from the product of normalized capacitance and capacitance without edge effect.

Table 3-4 Selected dielectric material properties

Dielectric Material	Air	Glass (Pyrex)	Silicon	Titanium dioxide (Ceramic class 1)	Barium Titanate (Ceramic class 2)
Relative permittivity (ϵ_r) at 20°C	1.0	4-7	11.8	86-173	1500-7400
Breakdown electric field (kV/mm)	3	14	30	12.4	150
Dielectric loss ($\tan \delta$)	0.0	3×10^{-3} @ 100 MHz	5×10^{-3} @ 1 GHz	3×10^{-3} @ 1GHz	2×10^{-2} @ 1GHz

According to the dimensions chosen, the aspect ratio b which is defined in Table 3.5 is 0.133. Thus by using the formula given in Table 3.5, the capacitance is calculated as the product of normalized capacitance and capacitance without edge effect.

In order to simulate the coupler, the capacitive coupler plates are modelled in JMAG-Designer using the geometry editor as discussed earlier. The plates are placed face to face in the air region and the dielectric area is modelled in between.

Table 3-5 Parallel plate capacitance

Parallel-Plate Geometry	Aspect ratio (b)	Capacitance without edge effect	Normalized capacitance
Rectangular	$b = \frac{\text{Plate separation}}{\text{Plate width}}$	$C_R = \frac{\epsilon_0 \epsilon_r w l}{d}$	$C_{RN} = 1 + 2.343 \times b^{0.891}$ ($0.1 \leq b \leq 1.0$)
			$C_{RN} = 1 + 2.343 \times b^{0.992}$ ($1.0 \leq b \leq 10.0$)
Square	$b = \frac{\text{Plate separation}}{\text{Plate width}}$	$C_S = \frac{\epsilon_0 \epsilon_r w^2}{d}$	$C_{SN} = 1 + 2.343 \times b^{0.891}$ ($0.1 \leq b \leq 1.0$)
			$C_{SN} = 1 + 2.343 \times b^{0.992}$ ($1.0 \leq b \leq 10.0$)
Disk	$b = \frac{\text{Disk separation}}{\text{Disk diameter}}$	$C_D = \frac{\epsilon_0 \epsilon_r \pi r^2}{d}$	$C_{DN} = 1 + 2.367 \times b^{0.867}$ ($0.005 \leq b \leq 0.5$)
			$C_{DN} = 1 + 2.343 \times b^{0.992}$ ($0.5 \leq b \leq 5.0$)

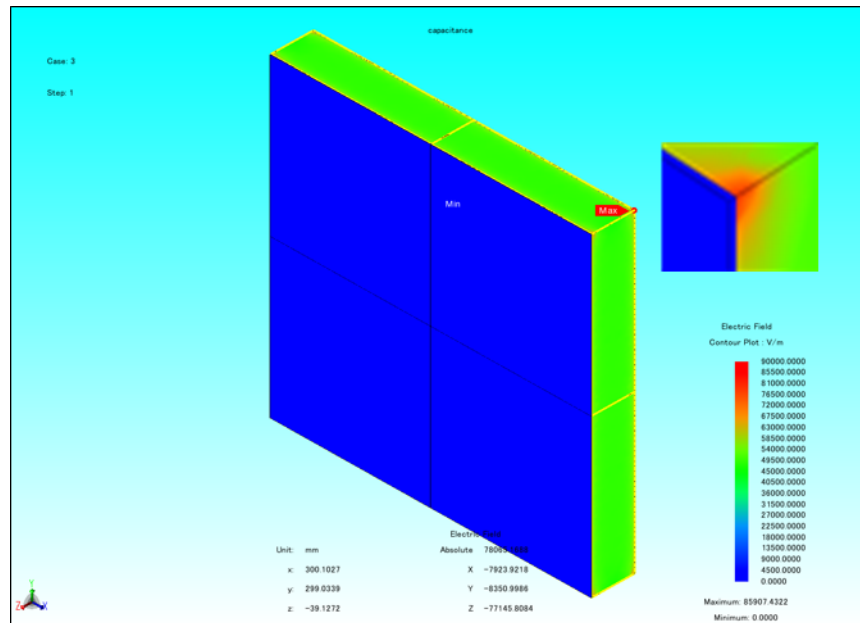
As the geometry of parallel plate capacitor and its electric field are symmetric, a quarter model is used for the analysis and the results are extended to the full model in order to reduce the computational time. The air region is created in an area of 1000 x 1500 mm². This helps to observe the entire span of electric field around the coupler including air region as given in Figure 3.14. For performing the electrostatic analysis, an electric potential is applied between the parallel plates. This potential is determined after simulating the CPT system for the designed parameters, (given in Table 3.6) in a circuit simulation software, here PSIM is used. From the parameters, the potential across the plates are found for each case.

Table 3-6 Circuit parameters for high power interface

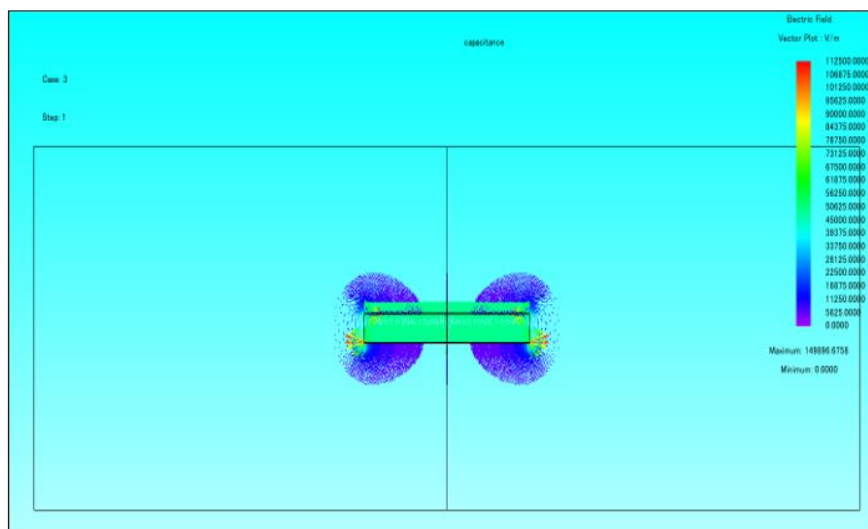
Parameters	Values
f_0	1 MHz
P_0	1 kW
$V_{P(RMS)}$	120 V
$V_{S(RMS)}$	110 V

Dielectric (Case)	C_1/C_2	L_P/L_S
Air	3.98E-11	636 μ H
Silicon	4.78E-10	53 μ H
Titanium dioxide	3.98E-09	6.36 μ H
Barium Titanate	1.99E-07	127 nH

The corresponding electric field distribution can be observed as in Figure 3.14 for each case. At this point the charge accumulation takes place on both transmitter and receiver plates. The amount of charge stored depends on the dielectric material used. Using the electric charge distribution model, the surface charge density is found and from this, the capacitance can be validated.



(a)



(b)

Figure 3-14 Electric field distribution in high power interface. (a) Corner field (b) Vector plot

The capacitive coupler is built in the lab, see Figure 3.15 and the capacitance is measured using Keysight E4980A LCR meter with air as dielectric. The result is provided in Table 3.7, column 4. From the knowledge of breakdown electric field of dielectrics (given in

column 5) used, the break down voltage can be calculated for different power transfer distances (see column 6 and 7).

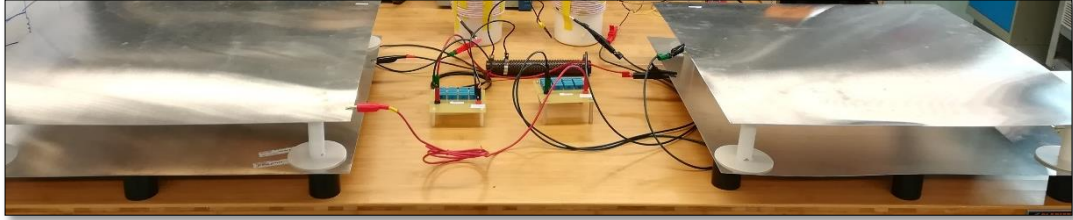


Figure 3-15 CPT experimental setup photo with air as dielectric.

The electric field created in the dielectric material varies depending on the size and shape of the material and the location (corners/center) on the material where the voltage is applied. In parallel plate structures, the electric field E is proportional to the voltage difference V divided by the thickness d of the insulator, and hence the breakdown voltage is proportional to the distance between the plates covered by the dielectric, which is the power transfer distance. For larger power transfer distances, the breakdown voltage limit is higher and therefore such applications like EV charging can operate safely without the concern of arcing compared to the small power transfer distance applications (Table 3.7 columns 6 and 7). The edge effects are prominent at the corners and can be observed in Figure 3.14. The use of circular parallel plates can alleviate this issue [70].

The results are summarized in Table 3.7. In column 1 the dielectric materials used are listed. The material properties are added in JMAG designer to conduct the FEA analysis. The calculated values of capacitance between the link is listed in column 1.

Table 3-7 Influence of Various Dielectrics

Dielectrics	Capacitance (<i>F</i>) (calculated)	Capacitance (<i>F</i>) (simulated)	Capacitance (<i>F</i>) (measured)	Breakdown Electric-field (kV/mm)	Breakdown Voltage @ 10 mm (kV)	Breakdown Voltage @ 80 mm (kV)
BaTiO ₃	1.99E-07	1.99E-07	-	150	1500	12000
TiO ₂	3.98E-09	3.99E-09	-	30	300	2400
Silicon	4.78E-10	4.82E-10	-	12.4	124	992
Air	3.98E-11	4.21E-11	4.31E-11	3	30	240

In column 2, the JMAG simulated values are listed. The effective capacitance is improved with the use of dielectrics as predicted and the calculated and simulated values are very close for the high permittivity materials BaTiO₃ and TiO₂. However, there is 0.8% variance in the case of Silicon and 5.4% variance for air. The practical measurement was conducted for air alone as the dielectric condition and recorded in column 3. It is close to the simulated value with only 2.3% variance. Further, column 4 lists the break down electric field (kV/mm) limits of each dielectric material. As it can be observed in column 5 and 6 the breakdown voltage limits are much higher in the case of large air-gap interfaces if it is separated by dielectrics.

To summarize, wireless power transfer through capacitive coupling interface is investigated as a dual of inductive coupling interface for low to medium air-gap (~ 1 mm – 100 mm) applications. The value of coupling capacitance is dependent on the dielectric material used, area of the plates in the interface and distance between the plates. Here the effect of utilizing various dielectrics to improve the power transfer capability of the CPT

system is evaluated. From the analysis it is found that, the effective coupling capacitance can be increased with the introduction of dielectrics provided the area covered by dielectrics is greater than the air-gap area. Moreover, the use of dielectrics gives much larger limits on breakdown voltage at all power transfer distances.

Chapter 4. Reduced capacitance model for parallel plate capacitive wireless power transfer system

A typical layout of the CPT system for EV charging is given in Figure 4.1. It consists of loosely coupled capacitor plates at the roadside transmitter (primary) and vehicle side receiver (secondary) interface that works on the principle of electrostatic induction. As long as the primary side is activated, the high voltage at the primary plate induces a high-frequency electric field between the primary and secondary plates by the displacement of charges. This causes a displacement current to flow from primary to secondary of the capacitive link.

The amount of displaced charges is also termed as displacement flux Ψ . The displacement flux is the sum of electric field lines passing through the overlapping area A of primary and secondary and displacement flux density D is given by (4.1).

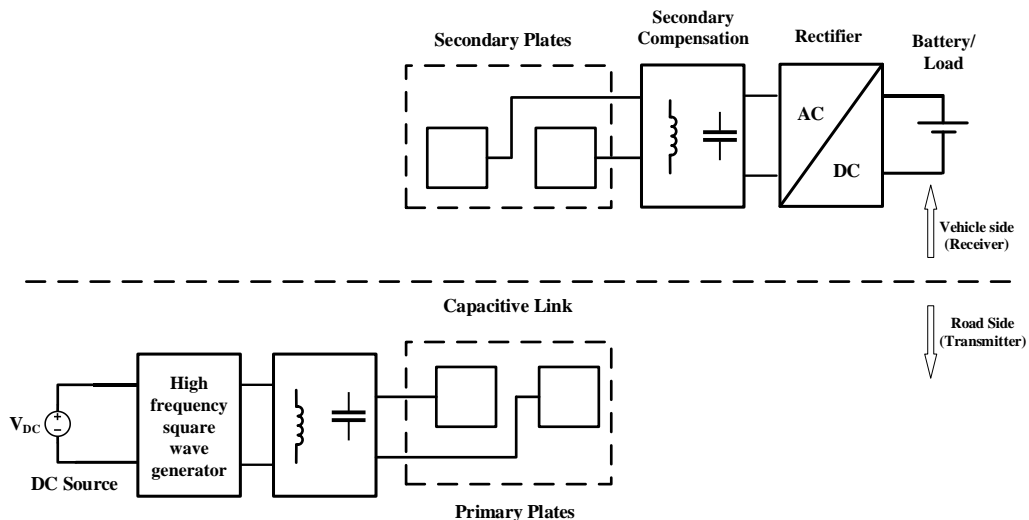


Figure 4-1 Layout of CPT system for EV charging.

$$D = \psi/A = \varepsilon_0 \varepsilon_r E \quad (4.1)$$

$$E = V/d_{air} \quad (4.2)$$

Here, ε_0 is the permittivity of vacuum and ε_r is the permittivity of respective dielectric used. The electric field strength E is given in (4.2), where V is the terminal voltage of the link plates separated by a distance d_{air} .

As the CPT system is operated at resonance with the help of compensation circuits at the primary and secondary sides, it minimizes the overall impedance of the circuit and reduces the reactive power contribution. This also accounts for deciding a quality factor in the CPT system, as given in (4.3) for a series compensated network. The relation between circuit quality factor with respect to the input voltage to the link V_{in} and voltage across coupling plates V_c is defined by (4.4).

$$Q = \frac{1}{R} \sqrt{C/L} \quad (4.3)$$

$$V_c = -jQV_{in} \quad (4.4)$$

Therefore, in the design of CPT systems, the parameter V_c should be less than the breakdown voltage of the dielectric materials between coupling plates. For wireless power transfer applications, where air is the dielectric, the break down electric field is 3×10^6 V/m and the breakdown voltage can be in the range of 75 kV to 300 kV for an air gap variation of 25 mm to 100 mm. Also, the link capacitance is very small, in the order of 100s of pico-farad. These are also limited by the effective coupling area and the air gap between the

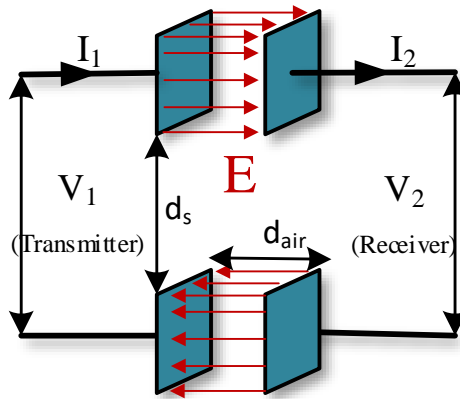


Figure 4-2 Bipolar capacitive coupler arrangement showing the flow of electric field lines, separation distance d_s and power transfer distance d_{air} .

coupling plates. In order to increase the output voltage, the following options are possible. Firstly, operating frequency can be increased to reduce the impedance of the circuit [112]; secondly, designing various compensation circuits to counteract the capacitive impedance [28]; thirdly, to get the required output voltage, high frequency transformer based or converter based boost up circuits can be used to increase the voltage fed into the coupling plates [113].

The capacitive link, as shown in Figure 4.2, contains four parallel metal plates in a 2x2 matrix arrangement forming a bipolar topology. In a bipolar coupling interface, it must comprise of at least two pairs of conductive plates on either side that acts as the primary and secondary. When the primary plate of the capacitor is energized from a high-frequency inverter, an electric field is set up between the primary side and secondary side plates due to the charges q_1 and q_2 accumulated on either sides due to electrostatic induction. This electric field causes a displacement current to flow in between and enables the power transfer.

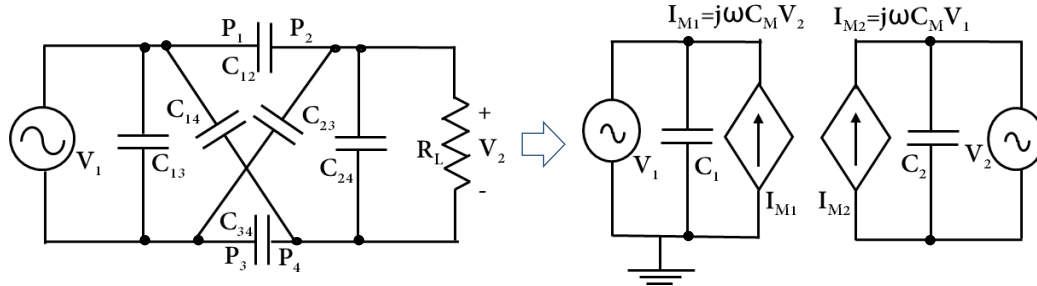


Figure 4-3 Six capacitances' influence in the bipolar coupler and its equivalent current source model.

From the circuit model of the capacitive coupler, as shown in Figure 4.3, the capacitive couplings between the plate pair result in six coupling capacitors [21]. At the primary side, plates P_1 and P_3 acts as the transmitter, while plates P_2 and P_4 that are placed at the secondary side constitute the receiver. In Figure 4.3, the capacitive coupling interface includes main capacitances (C_{12} , C_{34}), same side capacitances (C_{13} , C_{24}), and cross coupling capacitances (C_{14} , C_{23}). By considering the effect of these coupling capacitors, the equivalent capacitances C_1 and C_2 and the mutual capacitance C_M are derived. The equivalent current source model, (see Figure 4.3) consists of two coupling capacitance C_1 and C_2 along with mutual capacitance C_M .

In [114] a charge balance model is defined which establishes the relation between equivalent capacitances, mutual capacitance and the primary and secondary voltages involved. The analysis of this circuit model is carried out as follows. The charge q_1 corresponds to the applied input voltage V_1 contributing to C_1 at the primary side, which induces charge accumulation q_2 and the corresponding output voltage V_2 at the secondary side as given in (4.5) and (4.6).

$$q_1 = V_1 C_1 + V_2 C_M \quad (4.5)$$

$$q_2 = V_2 C_2 + V_1 C_M \quad (4.6)$$

The equivalent capacitances C_1 and C_2 are calculated by short-circuiting the secondary and primary voltages respectively. The relations are given in (4.7) and (4.8). The mutual capacitance, C_M is further evaluated as in (4.9).

$$C_1 = \frac{q_1}{V_1} = C_{13} + \frac{(C_{12} + C_{14})(C_{32} + C_{34})}{C_{12} + C_{14} + C_{32} + C_{34}} \quad (4.7)$$

$$C_2 = \frac{q_2}{V_2} = C_{24} + \frac{(C_{12} + C_{32})(C_{14} + C_{34})}{C_{12} + C_{14} + C_{32} + C_{34}} \quad (4.8)$$

$$C_M = \frac{C_{12}C_{34} - C_{14}C_{32}}{C_{12} + C_{14} + C_{32} + C_{34}} \quad (4.9)$$

The capacitive coupling coefficient k_E that defines the effective mutual coupling based on the influence of main and cross coupling capacitances is given by,

$$k_E = \frac{C_M}{\sqrt{C_1 C_2}} \quad (4.10)$$

In [114] a quantification of the coupling coefficient is provided and the span of k_E is proved to be from -1 to 1 for different coupling conditions.

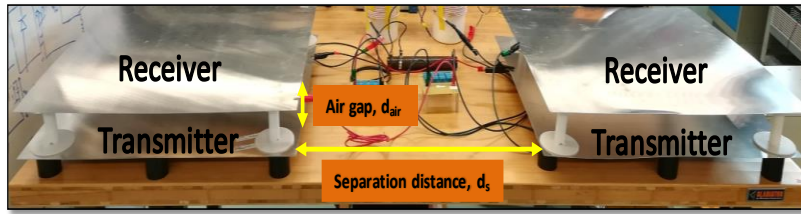


Figure 4-4 Air gap or power transfer distance, d_{air} and separation distance, d_s .

In this chapter, author proposes a reduced capacitance circuit topology for analyzing the bipolar capacitive links when the separation distance d_s (distance between transmitter side plate pair or receiver side plate pair) is greater than the power transfer distance d_{air} (distance between the transmitter and receiver plate pair)(see Figure 4.4). In previous works, for all conditions, six capacitance modelling (SCM) as discussed earlier is performed including the influence of all six capacitors which are main capacitances (C_{12} , C_{34}), same side capacitances (C_{13} , C_{24}), and cross coupling capacitances (C_{14} , C_{23}). However, for large separation distance d_s , this modelling is not essential and can be reduced to include the main capacitances (C_{12} , C_{34}) only as the influence of other capacitances are insignificant. Thus a criteria for choosing the reduced capacitance modelling (RCM) is formulated based on the separation distance, power transfer distance and plate width and a new parameter bipolar capacitive link dispersion factor is derived. The reduced model analysis achieved load and coupling coefficient independent unity-gain operation at the designed resonant frequency and avoided the formation of multiple resonance frequencies in the vicinity of designed resonant frequency. Thus simplifying the need for the multiple resonant frequency tracking.

4.1 Reduced Capacitance Modelling and Formation of BCD

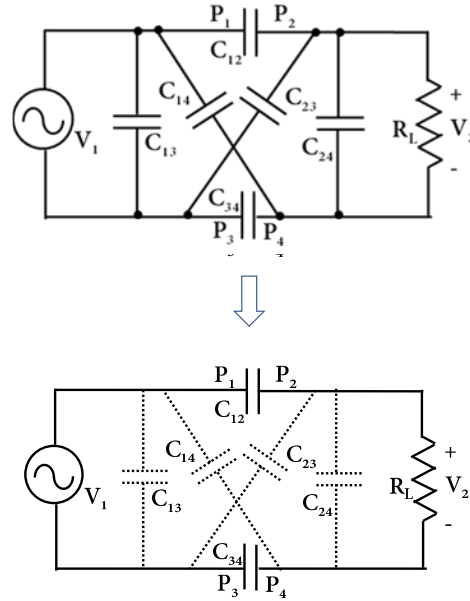


Figure 4-5 Six capacitances' model to reduced capacitance model approximation by removing same side and cross coupling capacitances.

For a horizontal or bipolar plate arrangement, when the plates at each side are kept at adequate separation distance d_s , (see Figure 4.4) in comparison with the power transfer distance, the values of the same side capacitances C_{13} , C_{24} and cross coupling capacitances C_{14} , C_{23} are negligible. The minimum separation distance to be maintained is derived shortly. Then, the equivalent capacitances C_1 , C_2 and the mutual capacitance C_M are reduced to the series combination of main capacitances C_{12} , C_{34} as given in (4.11) and (4.12).

$$C_M = \frac{C_{12}C_{34}}{C_{12} + C_{34}} \quad (4.11)$$

$$C_1 = C_2 = C_M \quad (4.12)$$

Further, when the coupling plates at both sides are symmetric or in equal dimensions, as in (4.13), (4.11) reduces to (4.14). Further, the coupling coefficient k_E is equal to 1.

$$C_{12} = C_{34} \quad (4.13)$$

$$C_1 = C_2 = C_M = C_{12}/2 \quad (4.14)$$

$$k_E = 1 \quad (4.15)$$

Therefore, in theory, when the same side and cross coupling are eliminated, only the main capacitance exists between the primary and secondary sides, and the coupling coefficient is unity for the symmetric bipolar coupler arrangement. However, since the measured main capacitances C_{12} and C_{34} can only be approximately equal, k_E will not be exactly unity, but close to it, in a practical scenario.

Hence, when the plates at each side are kept at an adequate separation distance d_s , (see Figure 4.4) the cross coupling and same side capacitances are weakened and the effective capacitances in the CPT are reduced to a series combination of C_{12} and C_{34} as depicted in Figure 4.5. Nevertheless, this approximation to reduced capacitance model cannot be useful when the application require a compact structure where the same side plate pairs need to be close enough and the effect of cross coupling capacitances is pronounced, refer Figures 4.6 and 4.7.

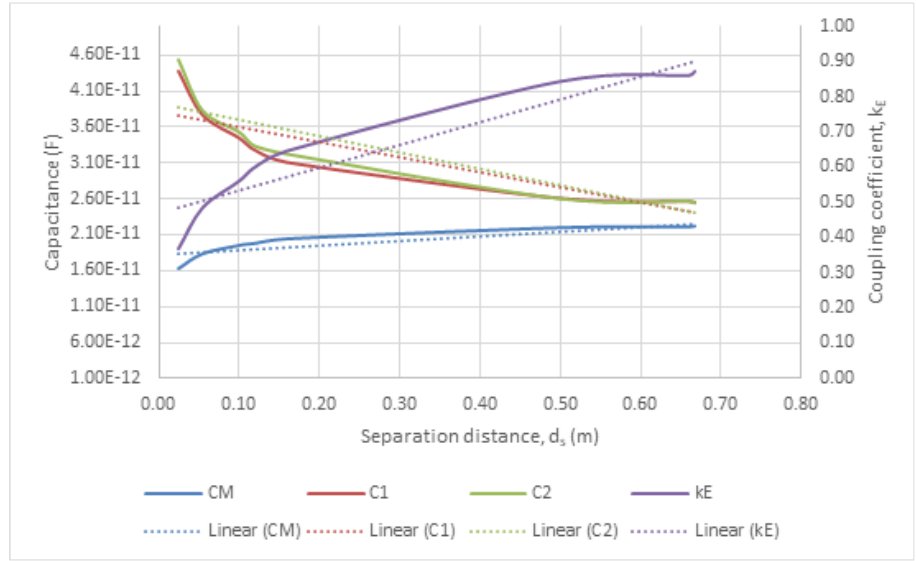


Figure 4-6 Effect of separation distance, d_s on coupling coefficient, k_E at an air gap, $d_{air} = 100$ mm.

The power transfer distance d_{air} selected is based on the installation locations of capacitive link which can be either underneath the vehicle where the d_{air} ranges from 100 mm to 200 mm or on the front and rear bumpers [34] or sides of the vehicle where d_{air} can be much smaller that is in the range of 10 mm to 50 mm.

Here, in Figure 4.6, when the 600 mm length primary and secondary square plate pairs are at an air gap (power transfer distance) $d_{air} = 100$ mm and are separated at a distance, $d_s = 25$ mm, the equivalent capacitances are around 45 pF and mutual capacitance is at 16 pF giving a coupling coefficient, $k_E \cong 0.3$. From the trend lines shown in the graph, when the separation distance d_s is at around 650 mm, the equivalent capacitances and mutual capacitance are converging and the coupling coefficient is approaching unity.

Similarly, in Figure 4.7, when the $d_{air} = 25$ mm, the equivalent capacitances are around 98 pF and mutual capacitance is at 62 pF giving a coupling coefficient, $k_E \cong 0.64$. The

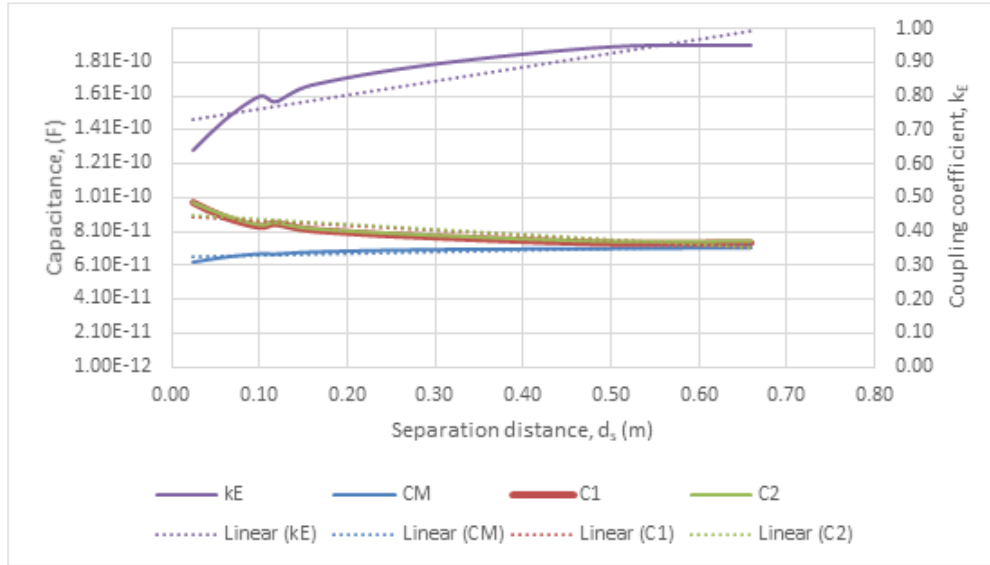


Figure 4-7 Effect of separation distance, d_s on coupling coefficient, k_E at an air gap, $d_{air} = 25$ mm.

capacitances are converging beyond 500 mm and $k_E \cong 0.95$. Therefore the findings are summarized as:

When d_s is less than d_{air} , k_E is less than 0.5 and the effects of cross coupling and same side capacitances are predominant and the use of six capacitances model is essential. That means more compact the system, the influence of cross coupling and same side capacitances play a major role in the capacitive link modelling.

On the contrary, when d_s is greater than or equal to d_{air} , k_E attains a value greater than 0.5 and the use of reduced capacitance model is advisable. This is because the effects of cross coupling and same side capacitances starts diminishing beyond this point. Larger the d_s , higher the k_E and greater the accuracy in utilizing the reduced capacitance model.

A bipolar capacitive-link dispersion-factor (BCD) is defined here as the ratio of separation distance, d_s to aspect ratio, b . The aspect ratio b is the ratio of power transfer distance (d_{air}) to plate width (l). The BCD in meters is given as,

$$BCD = \frac{d_s}{b} = \frac{d_s * l}{d_{air}} \quad (4.16)$$

When $d_s=d_{air}$, the BCD is equal to the plate length l . Further, from the analysis of experimental measurements, the reduced model fitness is high when BCD is greater than one. Thus, the BCD gives a clear distinction on when to consider reduced capacitance and six capacitances modelling strategies.

4.2 Voltage gain derivation and comparison of SCM and RCM

4.2.1 Equivalent circuit analysis and voltage gain derivation

The circuit diagram of the CPT system in Figure 4.8 shows the topology of a synchronous buck configured CPT system. The GaN-based square wave generator comprises of power switches S_1 and S_2 , is switched at 1.18 MHz for driving the capacitive links. This generator produces a unipolar square-wave voltage, V_P , by driving switches S_1 and S_2 , with 50% duty cycles for each switch. The duty cycle d is defined as the ratio between the on-time of the switch S_1 and the switching period T_s . Small dead time t_d is provided in the experimental realization, between the consecutive transitions from S_1 to S_2 , and vice versa in order to prevent the possibility of cross conduction. This also helps to achieve soft switching. The transmitter side receives a unipolar square-wave voltage, V_P and this voltage is transferred to the receiver side through the compensation circuit. The compensation circuit consists of a dual LC resonant tank formed by L_p , C_p at the transmitter

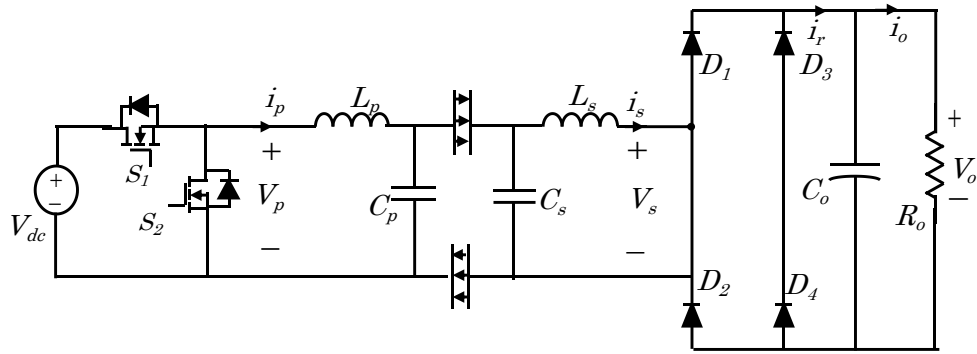


Figure 4-8 Circuit schematic of the CPT system.

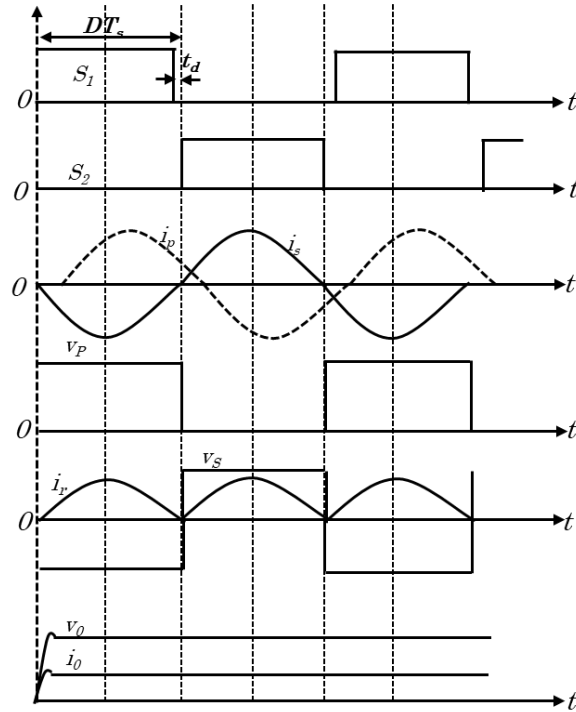


Figure 4-9 Steady state switching waveforms of the CPT system.

side, and L_s , C_s at the receiver side. The dual LC compensation block that resonates with the coupling interface improves the power transfer capability of the system [43]. The resonant network circulates the electric current and, as a result, the energy is delivered to the load through the capacitive link. At the receiver side, a diode bridge constitutes a full-

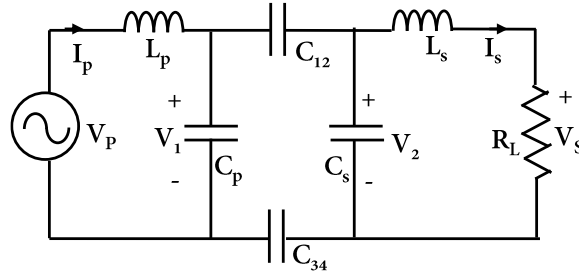


Figure 4-10 Reduced capacitance model: Equivalent circuit that includes the two main link capacitances (C_{12} and C_{34}) only and the dual LC compensation network.

wave rectifier to convert AC input to DC output and supply the load, R_o . The output capacitor smooths the rectified voltage and current. The unipolar square wave voltage generated at the output of the converter contains undesirable higher-order harmonics. Due to the bandpass filtering action of the resonant link, the link input current shape is maintained sinusoidal (see Figure 4.9). Therefore, the first harmonic approximation is utilized to model the resonant capacitive link as realized by the equivalent circuit in Figure 4.10.

$$V_P = \frac{2V_{dc} \sin \omega t}{\pi} \quad (4.17)$$

$$V_S = \frac{4V_0 \sin \omega t}{\pi} \quad (4.18)$$

$$R_L = \frac{8}{\pi^2} R_o \quad (4.19)$$

The fundamental voltage component of the unipolar square wave seen by the resonant tank, V_P is given by (4.17) and the fundamental voltage component at the full bridge rectifier input, V_S is given by (4.18). The load resistance R_L is the equivalent resistance seen

from the input of the rectifier and capacitive filter as given in (4.19). By applying KVL in the equivalent circuit given in Figure 4.10, results in (4.20-4.22) and by defining the reactances as in (4.23-4.28), the currents i_p , i_d , i_s in each loop (4.29-4.31) are obtained. The rectified output current I_o is given in (4.).

$$V_p - j\omega L_p i_p - \frac{i_p - i_d}{j\omega C_p} = 0 \quad (4.20)$$

$$-\frac{i_d}{j\omega C_{12}} - \frac{(i_d - i_s)}{j\omega C_s} - \frac{i_d}{j\omega C_{34}} - \frac{(i_d - i_p)}{j\omega C_p} = 0 \quad (4.21)$$

$$-j\omega L_s i_s - i_s R_L - \frac{(i_s - i_d)}{j\omega C_s} = 0 \quad (4.22)$$

$$j\omega L_p = X_{Lp} \quad (4.23)$$

$$\frac{1}{j\omega C_p} = X_{Cp} \quad (4.24)$$

$$j\omega L_s = X_{Ls} \quad (4.25)$$

$$\frac{1}{j\omega C_s} = X_{Cs} \quad (4.26)$$

$$\frac{1}{j\omega C_{12}} + \frac{1}{j\omega C_{34}} = X_{Cr} \quad (4.27)$$

Using the currents obtained in (4.28-4.30), the voltage stress across the capacitances V_{cp} , V_{cr} , and V_{cs} are calculated (4.32-4.34). The output voltage V_S is expressed in (4.35). The resultant voltage gain is derived in (4.36-4.38).

$$i_p = \frac{V_p + X_{Cp}i_d}{X_{Lp} + X_{Cp}} \quad (4.28)$$

$$i_d = \frac{X_{Cp}(X_{Ls} + R_L + X_{Cs})V_p}{X_{Ls}X_{Cr}(X_{Lp} + X_{Cp}) + X_{Ls}X_{Lp}(X_{Cp} + X_{Cs}) + X_{Lp}X_{Cs}(X_{Cp} + X_{Cr}) + A + B + C} \quad (4.29)$$

$$A = X_{Cp}X_{Cs}(X_{Cr} + X_{Ls}) \quad B = R_LX_{Lp}(X_{Cp} + X_{Cr} + X_{Cs}) \quad C = R_LX_{Cp}(X_{Cr} + X_{Cs})$$

$$i_s = \frac{X_{Cs}i_d}{(X_{Ls} + R_L + X_{Cs})} \quad (4.30)$$

$$I_0 = \frac{2i_s}{\pi} \quad (4.31)$$

$$V_{cp} = \frac{i_p - i_d}{j\omega C_p} = (i_p - i_d)X_{Cp} \quad (4.32)$$

$$V_{cr} = \frac{i_d}{j\omega C_r} = i_dX_{Cr} \quad (4.33)$$

$$V_{cs} = \frac{i_d - i_s}{j\omega C_s} = (i_d - i_s)X_{Cs} \quad (4.34)$$

$$V_s = i_sR_L \quad (4.35)$$

Reduced capacitance model voltage gain curve

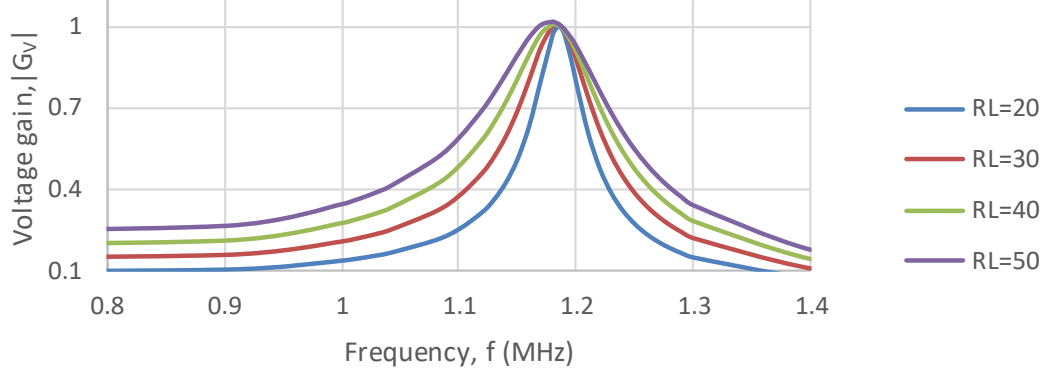


Figure 4-11 Gain magnitude plot of the CPT with reduced capacitance model for varying load conditions.

$$\begin{aligned}
 V_S &= \frac{X_{Cs} i_d R_L}{(X_{Ls} + R_L + X_{Cs})} \\
 &= \frac{X_{Cp} X_{Cs} R_L V_P}{X_{Ls} X_{Cr} (X_{Lp} + X_{Cp}) + X_{Ls} X_{Lp} (X_{Cp} + X_{Cs}) + X_{Lp} X_{Cs} (X_{Cp} + X_{Cr}) + X_{Cp} X_{Cs} (X_{Cr} + X_{Ls}) + D + E} \quad (4.36) \\
 D &= R_L X_{Lp} (X_{Cp} + X_{Cr} + X_{Cs}), E = R_L X_{Cp} (X_{Cr} + X_{Cs})
 \end{aligned}$$

$$\begin{aligned}
 \frac{V_S}{V_P} &= \frac{X_{Cp} X_{Cs} R_L}{X_{Ls} X_{Cr} (X_{Lp} + X_{Cp}) + X_{Ls} X_{Lp} (X_{Cp} + X_{Cs}) + X_{Lp} X_{Cs} (X_{Cp} + X_{Cr}) + X_{Cp} X_{Cs} (X_{Cr} + X_{Ls}) + D + E} \quad (4.37)
 \end{aligned}$$

$$\begin{aligned}
 |G_V| &= \frac{V_S}{V_P} = \frac{s C_r R_L}{s^4 L_p (C_p L_s C_s + L_s C_r C_p + L_s C_r C_s) + F + G + H + 1} \\
 F &= s^3 R_L L_p (C_r C_s + C_p C_s + C_p C_r), G = s^2 (L_s C_r + L_s C_s + L_p C_p + L_p C_r), H = s (R_L C_s + R_L C_r) \quad (4.38)
 \end{aligned}$$

The magnitude of gain $|G_V|$ versus frequency plot is depicted in Figure 4.11. The plot in Figure 4.11 resembles the narrow bandpass filter characteristics. This is because, the resonant wireless power transfer systems are tuned circuits that provides low impedance path to the current at the resonant frequency and blocks all the other frequency currents. The CPT system attains unity gain at the resonant frequency, f_{RCM} , which is defined in (4.39).

$$f_{RCM} = \frac{1}{2\pi\sqrt{L_p C_p}} = \frac{1}{2\pi\sqrt{L_s C_s}} \quad (4.39)$$

Here, L_p and C_p , are the resonant tank elements at the primary side and L_s and C_s , are the resonant tank elements at the secondary side. As the system is designed to be symmetric, the resonant frequency at the primary side and the secondary side is the same. The quality factor of the system, Q is selected to be 9. The system resonant frequency was designed at 1.18 MHz which is the same as the switching frequency of the inverter.

4.2.2 Reduced capacitance model versus six capacitance model

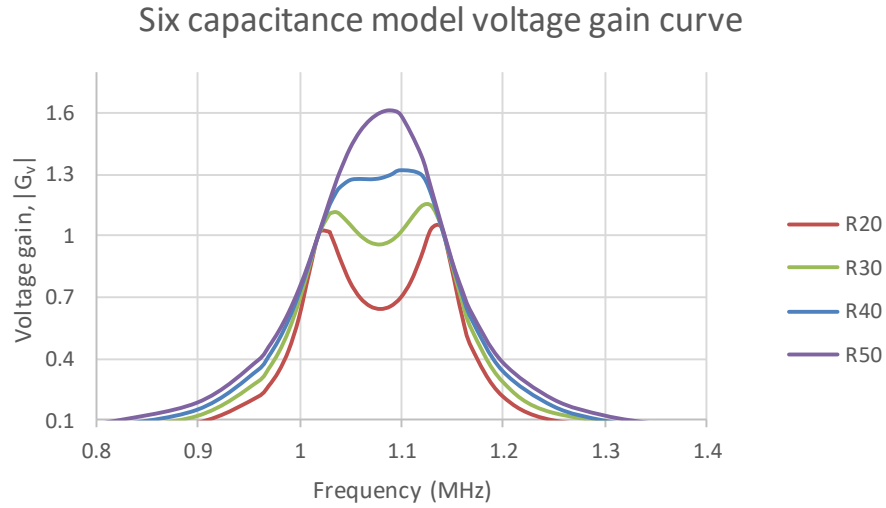


Figure 4-12 Gain magnitude plot of the CPT with six capacitance model for varying load conditions.

In [43], Lu. et. al introduced the dual LC compensated CPT system and was modelled as an equivalent behaviour source model with the current source approximation, (refer Figure 4.3) to represent the coupling capacitance. Here, the capacitive link was modelled to include all six capacitances (main capacitances (C_{12} , C_{34}), same side capacitances (C_{13} , C_{24}), and cross coupling capacitances (C_{14} , C_{23})). As the system is symmetric, primary and secondary inductances and capacitances are approximately equal and hence the resonant frequency remains the same at both sides. Here, the resonant frequency f_{SCM} is determined by (4.40). L_p and L_s are the resonant inductors. The link capacitance C_1 and C_2 are found using (4.7) and (4.8) which includes the influence of all six capacitances. Then C_{total1} is calculated as the sum of link capacitance C_1 and external resonant tank capacitor C_P (4.41). Similarly, C_{total2} is formed as the sum of link capacitance C_2 and external resonant tank capacitor C_S (4.42).

$$f_{SCM} = \frac{1}{2\pi\sqrt{L_p C_{total1}}} = \frac{1}{2\pi\sqrt{L_s C_{total2}}} \quad (4.40)$$

$$C_{total1} = C_1 + C_P \quad (4.41)$$

$$C_{total2} = C_2 + C_S \quad (4.42)$$

The model analysis showed that as the load resistance is varied, there exist upper and lower resonant frequencies where the unity gain is achieved, as given in Figure 4.12. These frequencies are termed as constant voltage frequencies, $f_{SCM(cv1)}$ and $f_{SCM(cv2)}$ given in equation 4.43 and 4.44 respectively which are dependent on the coupling coefficient k_c and are situated at either sides of the resonant frequency f_{SCM} .

$$f_{SCM(cv1)} = \frac{f_{SCM}}{\sqrt{1 + k_c}} \quad (4.43)$$

$$f_{SCM(cv2)} = \frac{f_{SCM}}{\sqrt{1 - k_c}} \quad (4.44)$$

Therefore, when the effect of same side and cross coupling capacitances are high, that is when the bipolar capacitive-link dispersion-factor (defined in the previous section) is less than one, the dual resonant frequencies are observed in the voltage gain characteristics (Figure 4.12). This makes it necessary to track these frequencies for the load independent unity-gain operation.

On the contrary, the proposed reduced capacitance model attains unity gain at the single resonant frequency f_{RCM} , independent of the load variations and the coupling coefficient as shown in Figure 4.11. Therefore, whenever possible, that is when the bipolar capacitive-link dispersion-factor is much greater than one, it is apparent to use the reduced capacitance

model as it simplifies the analysis and provides load independent and coupling coefficient independent operation at the designed resonant frequency.

4.3 Circuit parameter design, simulation and experimental validation

4.3.1 Design and Simulation

The capacitance of each of the square parallel plate coupling structure must incorporate the fringing field effects which are prominent when the plate dimension and power transfer distance is comparable. Thus the coupling capacitance is found using (4.45) where b is the ratio of power transfer distance (d_{air}) to plate width (l). The corresponding capacitances calculated for different d_{air} values are tabulated in Table 4.1 as $C_{Plate-pair1}$ and $C_{Plate-pair2}$.

$$C_{Plate-pair} = (1 + 2.343b^{0.891}) \varepsilon_0 \varepsilon_r l^2 / d_{air} \quad (4.45)$$

As discussed in section 4.2, a symmetric LC compensation formed by L_p - C_p and L_s - C_s at the primary and secondary sides respectively is utilized to establish the resonance. In addition, this will also increase the effective capacitance and reduce the voltage stress on the capacitive link. The capacitances C_p and C_s are chosen based on the output power relation (4.46) (Refer section 5.4.2 in chapter 5).

$$P_0 = \frac{2\pi f_0 C_p C_s}{C_M} V_P V_S \quad (4.46)$$

Here, the mutual capacitance is determined using equations (4.14) and (4.45) which is dependent on the plate width and power transfer distance. The voltages V_P and V_S are defined in (4.17) and (4.18) respectively.

The circuit schematic in Figure 4.8 is simulated with the designed circuit parameters using PSIM and the waveforms are depicted in Figure 4.13. V_P is the unipolar square waveform generated at the link input from the synchronous buck configured inverter.

The capacitive link input/primary current I_P slightly lags primary link voltage V_P which makes sure the soft switching operation of the converter switches. The link output voltage V_S is in phase with output current I_S as seen at the input of the rectifier. The unipolar link input voltage leads the bipolar link output voltages by 180° which is matching with the phase angle analysis of derived voltage gain of the reduced capacitance model. This limits the circulating reactive power loss and improves the efficiency of the system. The rms value of voltage between the coupler/link plates P_1 and P_2 (or P_3 and P_4) is around 250 V and the rms value of voltage between same side plates P_1 and P_3 (or P_2 and P_4) is around 700 V when the power transfer distance is 25 mm. At a power transfer distance of 100 mm, the rms value of voltage between the coupler/link plates P_1 and P_2 (or P_3 and P_4) is around 1.5 kV and the rms value of voltage between same side plates P_1 and P_3 (or P_2 and P_4) is around 2.9 kV. As pointed out in section 4.1, the break down electric field is 3×10^6 V/m for air and the breakdown voltage limit is 75 kV for an air gap of 25 mm and 300 kV for

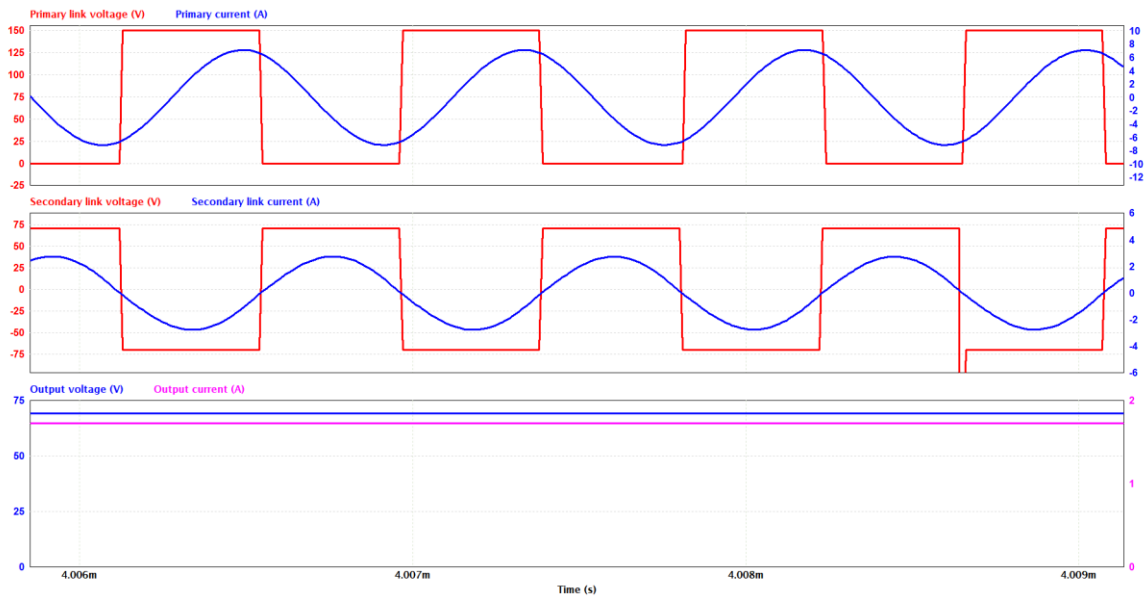


Figure 4-13 Simulated capacitive link input and output waveforms in PSIM.

an air gap of 100 mm. Therefore, there is no risk of dielectric breakdown and hence no concern of arcing in the designed system.

4.3.2 Experimental validation

The experimental prototype of the CPT system is built in the lab with the circuit parameters given in Table 4.1 (see Figure 4.14). The capacitive link or coupling plate is made up of square aluminum plate pairs of length (l) 600 mm which are separated by PVC tubes. The air gap (d_{air}) was varied to get 25 mm and 100 mm power transfer distance. The separation distance (d_s) is kept at 660 mm where $BCD = 15$ m and $k_E = 0.9$ for $d_{air}=25$ mm and $BCD = 4$ m and $k_E = 0.8$ for $d_{air}=100$ mm. The corresponding capacitances were measured using the Omicron Bode 100 analyzer. Then depending on the output power requirement (100-200 W), the capacitances C_p and C_s are selected, and these high-frequency thin-film external capacitor banks of 450 pF are connected at primary and secondary side. For the operating frequency of 1.18 MHz, the resonant tank is completed by designing the inductors using (33), which will resonate with the effective capacitances

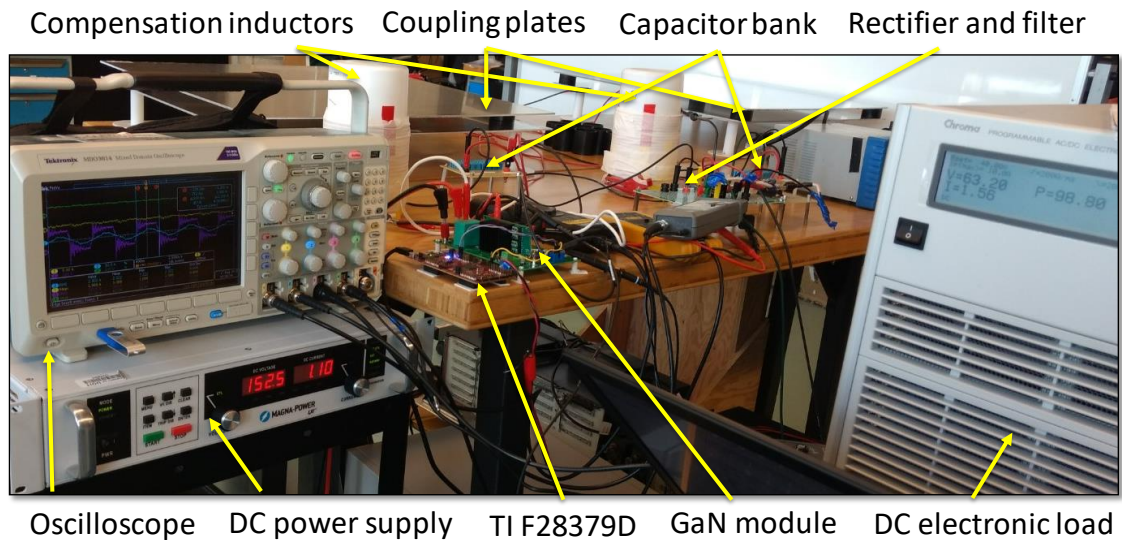


Figure 4-14 Photo of the experimental setup.

and generate high voltages on the plates for the sustained power transfer. The inductors L_p and L_s in the resonant tank have an air core and are made with AWG 8 Litz-wire. Litz-wire

Table 4-1 Circuit parameters for the CPT system

Parameters	Values
f_0	1.18 MHz
P_{max}	160 W
V_{DC}	0-200 V
V_0	0-80 V
$L_P (L_S)$	40 μ H
$C_P (C_S)$	450 pF
$C_{Plate-pair1}$	147 pF (for $l=600$ mm, $d_{air}=25$ mm)
$C_{Plate-pair2}$	47 pF (for $l=600$ mm, $d_{air}=100$ mm)
R_0	33-50 Ω

is a braided enameled conductor that can mitigate the skin and proximity effects, especially at high frequency. The skin effect causes self-induced eddy currents in the conductor and the proximity effect induces eddy currents in the nearby conductive material. Both phenomena create joule heating and reduce efficiency. Therefore, both inductors are wound on an air core using Litz-wire attaining the inductance value of 40uH.

At the transmitter side, input DC voltage is varied from 0-200V using Magna power programmable DC power supply which is connected to the inverter. The inverter switches are configured using a half-bridge evaluation board from GaN Systems featuring 650V E-HEMT GS66508T (30A/50m Ω) transistor and 2.5A gate drive optocoupler, ACPL-P34. The Texas Instruments TMS320F28379D microcontroller with 200 MHz clock frequency

is used to generate the PWM signals to drive the inverter switches externally with a dead time of 40ns. At the receiver side, a silicon carbide (SiC) Schottky diode rectifier bridge from GlobalPower is used. The rectifier output is smoothed by the low pass capacitive filter and is fed to the Chroma programmable DC electronic load at constant resistance mode.

In Figure 4.15, switching waveforms are given at switch S_1 . In Figure 4.16, the primary voltage and current (V_p , I_p) waveforms and load voltage and current (V_o , I_o) waveforms are given. The power transfer across the link was observed for varying DC input voltage (V_{DC})

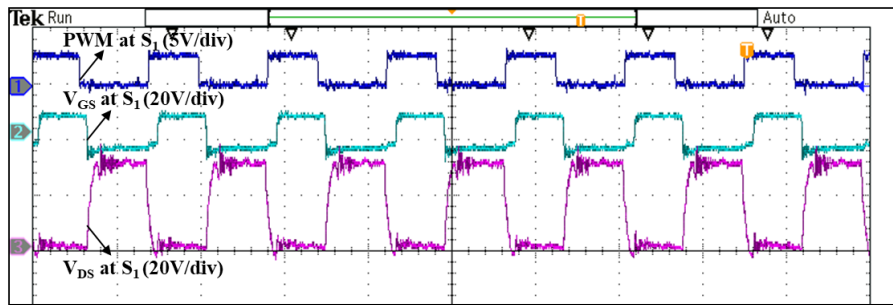


Figure 4-15 Experimental waveforms of the CPT system a) PWM pulses at switch S_1 (5 V/div) b) V_{GS} at S_1 (20V/div) c) V_{DS} at S_1 (20V/div).

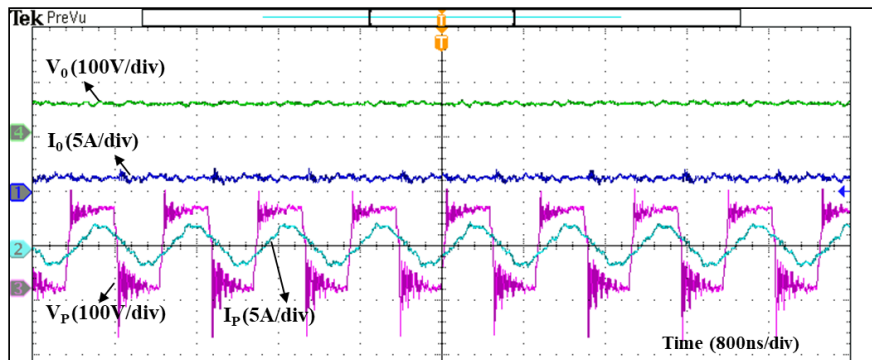
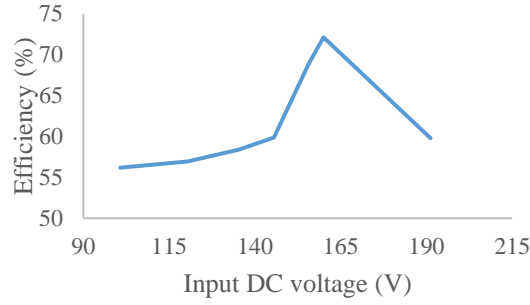
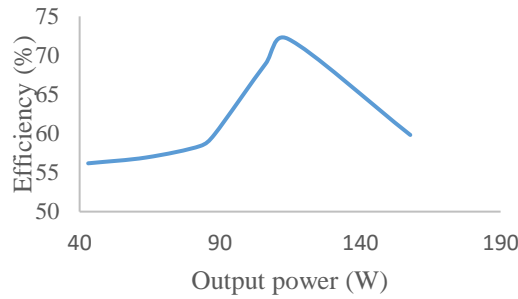


Figure 4-16 Experimental waveforms of the CPT system a) Link input voltage V_p (100 V/div) b) Link input current I_p (5 A/div) c) Output voltage V_o (100 V/div) d) Output current I_o (5 A/div).

from 100 V to 200 V. The corresponding link input voltage (V_p) rms is 45 V to 90 V. At a constant load resistance of $R_o = 40 \Omega$ ($R_L = 32.42 \Omega$), the DC output voltage across the load,



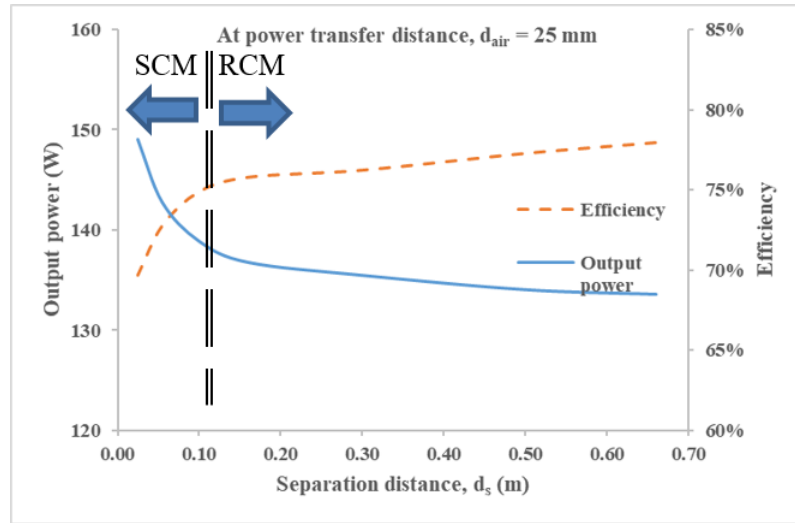
(a)



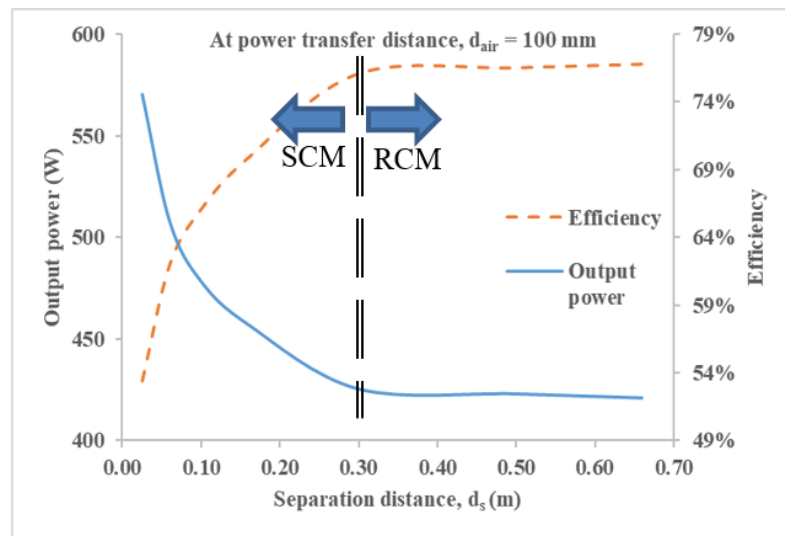
(b)

Figure 4-17 Efficiency curves a) For varying input DC voltage, b) For varying output power.

R_o is measured as 42 to 80 Ω . At $V_{DC}=160$ V, an input power of 158.4 W is transferred and an output power of 114.24 W is obtained, resulting a DC-DC efficiency of 72.12%. Under well aligned condition, the efficiency curve for varying dc voltage at $R_o = 40 \Omega$ is depicted in the Figure 4.17(a). For $V_{DC}=190$ V, an input power of 263 W is transferred and an output power of 160 W is obtained, resulting a DC-DC efficiency of 60.8%. The output power versus efficiency curve is given in Figure 4.17(b), where the maximum efficiency, $\eta_{max}=72.12\%$ is achieved at 114 watts. The maximum power transferred across the link is 160 watts at 60.8% efficiency. Though the experimental validation is done in the power range of 100-200 W for the proof of concept, the designed capacitive link is capable of handling several kilo watts of power transfer. However, the external capacitor bank is required to be redesigned to share the high link voltages. At higher frequency, the voltage



(a)



(b)

Figure 4-18 Output power and efficiency curves for varying separation distance: a) At power transfer distance, 25 mm b) At power transfer distance, 100 mm.

handling capability of the film capacitor bank decreases. Depending on the power transfer levels, the voltage stress across the compensation capacitor bank can be determined through simulation and the capacitors need to be selected accordingly for the implementation. The output voltage waveform V_o observed in Figure 4.16 is smoothed by

a capacitive filter of value $47 \mu\text{F}$ and the voltage ripple can be further reduced by increasing the filter capacitance.

The output power and efficiency comparison of reduced capacitance model (RCM) and six capacitance model (SCM) are depicted in Figure 4.18, for different power transfer distances. Here, the output power first increases with reduced efficiency levels for very small separation distances as evident from output power relation for the double sided LC compensated CPT system (4.46). This is because, C_M fluctuates due to the influence of cross coupling and same side capacitances when the plate pair separation is much small. Once the separation distance is larger such that this influence diminishes and the value of C_M stabilizes and efficiency levels improves. In both cases, the RCM is influential at a larger separation distance relative to the power transfer distance and length of the plate. For example, when power transfer distance $d_{air} = 25 \text{ mm}$, separation distance, $d_s = 100 \text{ mm}$ and plate length $l = 600 \text{ mm}$, the BCD value is 2.4 m and RCM can be applied. Similarly, when $d_{air} = 100 \text{ mm}$, for the same plate length, the RCM can be applied from a separation distance, d_s greater than or equal to 300 mm as BCD attains a value 1.8 m. Therefore, for BCD much greater than one meter, the influence of SCM diminishes and RCM is prevalent.

A reduced capacitance model for the capacitive power transfer system is discussed in this chapter which is derived from the conventional six capacitance model for the bipolar capacitive link topology. When the separation distance between the same side plate pair is large enough, the effect of same side and cross-coupling capacitances diminishes and the analysis based on a reduced capacitance modelling (RCM) with the two main capacitances can be carried out. A bipolar capacitive link dispersion factor (BCD) defined in this chapter determines the separation distance beyond which RCM can be applied relative to the plate

dimensions and power transfer distance. Further analysis showed that, RCM attains the unity voltage gain and load-independent operation at designed resonant frequency. The effectiveness of the model is analyzed and verified experimentally. The results indicated that, reduced capacitance model is suitable over six capacitance modelling for large charging area applications like electric vehicle charging where the separation distance between the same side plate pair is large enough and the effect of the same side and cross coupling capacitances can be circumvented in the analysis.

Chapter 5. Hybrid inductive and capacitive wireless power transfer system

The role of wireless power transfer systems is becoming increasingly popular in recent times, especially in medium to high power applications like EV charging [103]. The reasons for the uprising of this technology are the safety and convenience it provides by means of hands free charging as there is no need to plug in the charger to the EV as in wired chargers. In addition, through a modular link architecture, multiple vehicles can be charged without the need for handling or untangling any heavy cables such as in conventional wired chargers.

Two major wireless power transfer technologies suitable for EV charging are based on electromagnetic induction based inductive wireless power transfer (IPT) and electrostatic induction based capacitive wireless power transfer (CPT). IPT is rapidly evolving into a matured technology achieving efficiencies above 90% and reaching power levels of hundreds of kilo watts with higher power transfer distance (also referred as air-gap) in the range of 100 mm to 200 mm [2], [104]–[108]. CPT, considered as the dual of IPT, started off with low power (tens of watts) and small air-gap (<1mm) applications has progressed in to medium power transfer (~3 kW) and higher air-gap applications [25], [28], [52], [109]–[114]. A detailed comparison between IPT and CPT technologies suitable for EV charging is provided in [115]. A comparison of certain features in these technologies is given in Table 5.1. It highlights the need for integrating their benefits to enhance the performance of EV wireless charging.

Table 5-1 WPT system comparison

WPT Technology	Freq.	Power level	Coupler/Link			Surface power density and Efficiency	Misalignment tolerance	Metal object tolerance	Eddy currents
			Design	Cost	Weight				
IPT	kHz	High	Complex	High	High	High	Medium	No	Present
CPT	MHz	Medium	Simple	Low	Low	Medium	High	Yes	Absent

In literature, there were several successful attempts to integrate inductive and capacitive couplers for mutual power transfer that includes low (tens of watts) to medium power (several kW) applications as discussed in chapter 2 [94], [96], [97], [116], [117]. As this chapter focuses on light duty EV charging application, the following research works are selected. In [94], a combined IPT-CPT system realized by series connection of IPT and CPT link achieved a DC–DC efficiency of 94.95% when the converter transfers 3.0 kW of power. The full bridge inverter is switched at 1 MHz, for effective coupling. In this HPT, 70% of power is transferred using IPT and 30% using CPT. In [97], the HPT system formed by parallel connected IPT and CPT link achieved a 91.9% DC–DC efficiency at 1.1 kW power level using a full bridge inverter topology at an operating frequency of 800 kHz.

The power transfer contributed by both the links were approximately equal. In these works, the selected switching frequency for the operation of entire HPT system is very high due to the dependent nature of the IPT and CPT link. High frequency of operation is required for effective capacitive coupling and further for effective CPT. However, operating an inductive link at this high frequency and high power can generate electromagnetic radiations which exceeds the safe limits [14], [78], [80].

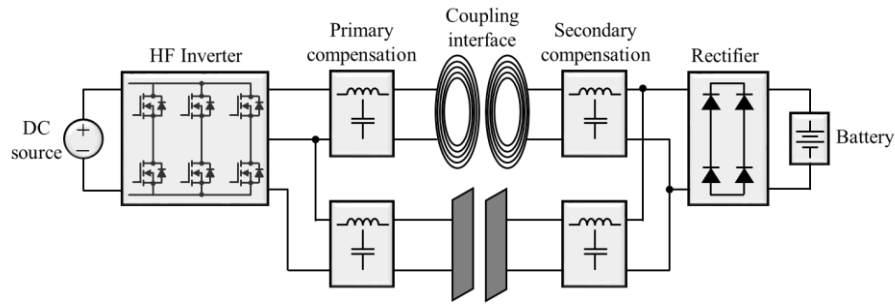


Figure 5-1 Hybrid inductive and capacitive wireless power transfer system block diagram.

In order to overcome this limitation, authors propose a high frequency three-leg inverter topology to combine inductive and capacitive links in parallel. Block diagram of the proposed concept for EV charging, given in Figure 5.1, consists of a HF three-leg inverter, primary compensation, coupling interface, secondary compensation, rectifier followed by the battery. The function of high frequency three-leg inverter is to provide a simultaneous dual frequency operation at 85 kHz and 1 MHz for switching inductive and capacitive links respectively. Further, the compensation block that resonates with the coupling interface improves the power transfer capability of both systems. A series-series capacitor compensation is provided at primary and secondary sides for the IPT system [118]. A dual LC compensation is employed in the CPT system [119]. The overall system power is contributed 66% by inductive link and 33% by the capacitive link. The modular structure of this HPT system also allows independent operation of the links besides easier implementation in static and dynamic wireless EV charging applications.

5.1 Proposed Topology

5.1.1 Circuit schematic

The circuit schematic of the three-leg inverter configured hybrid wireless power transfer system is given in Figure 5.2. The HPT system comprises of independent IPT and CPT branches driven by the three-leg inverter. The proposed three-leg inverter constitutes two complementary switches in each leg.

The switches S_1, S_2, S_3 and S_4 form a full bridge inverter topology switching at 85 kHz to drive the inductive ac link branch. The switches S_5 and S_6 switching at 1 MHz form a half bridge topology for independently driving the capacitive ac link branch. In this topology, in order to combine both systems, the first leg formed by switches S_1 and S_2 is selected as the reference leg. Therefore, the input dc link voltage V_{dc} is converted into two high frequency ac voltages, which are the input voltage reference V_{p1} (V_{IPT}) at the inductive link and V_{p2} (V_{CPT}) at the capacitive link. The inductive ac link input voltage is controlled by providing phase shift modulation in the first two legs. Here, the duty cycle of the

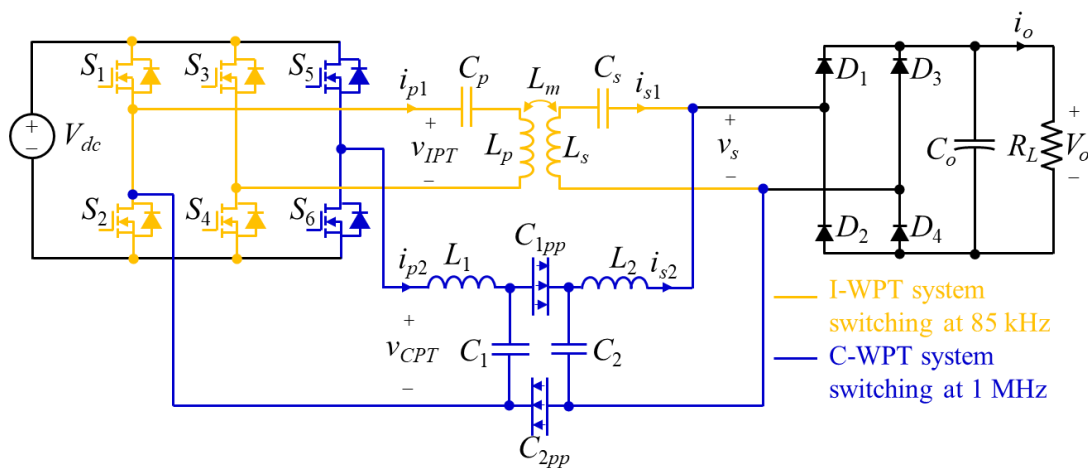


Figure 5-2 Circuit schematic of the proposed converter for hybrid inductive and capacitive wireless power transfer system.

switching waveforms is constant at 0.5, but a phase delay is introduced between the first and second legs that determines the link voltage. The capacitive ac link input voltage is duty cycle controlled.

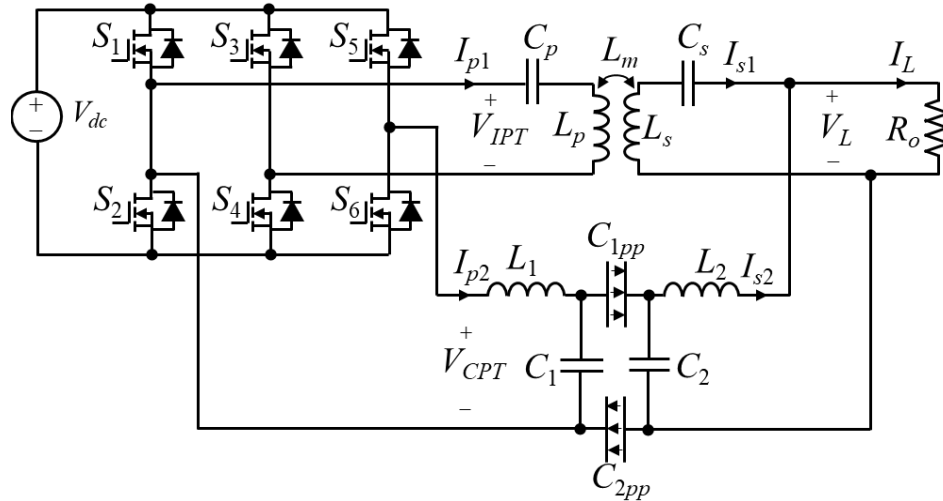


Figure 5-3 The equivalent circuit of the HPT system without rectifier.

Further, the compensation circuits are decided for both systems to boost the effective power transfer capability through resonance. A symmetric series-series compensation circuit is selected for the inductive ac link at a resonant frequency of 85 kHz at primary and secondary side. Thus, this branch offers a low impedance path to the currents at 85 kHz. Similarly, a symmetric dual LC compensation circuit that resonates at 1 MHz is designated for the capacitive ac link which provides a low impedance path to the currents at frequency 1 MHz and blocks the IPT branch currents of frequency 85 kHz. Finally, at the secondary side, the compensation circuit is followed by the rectifier, filter capacitor and the load resistance, R_L which represents the battery.

5.2 Modes of operation of the proposed converter

The load circuit comprises of two independent resonant circuits, namely low frequency IPT circuit and high frequency CPT circuit as shown in Figure 5.3. The resistance R_0 is the effective resistance comprising the rectifier and the load R_L . The switching scheme along with the link voltages (V_{IPT} , V_{CPT}) and currents (I_{p1} , I_{p2}) are given in Figure 5.4. The first and second legs form a full bridge inverter to drive the IPT system where the switches on each leg are on for 50% of switching period in a complementary fashion and the V_{IPT} is regulated by controlling the phase shift between the two inverter legs for the IPT system where δ is the phase shift angle. In the CPT system, a duty cycle control on complementary switches in the third leg is utilized to regulate the V_{CPT} whose polarity is determined by the first leg of the converter which acts as a reference.

As discussed, the IPT system is controlled by first and second legs of the converter that consists of switches S_1 - S_2 and S_3 - S_4 respectively. The switching pulses in each leg is complementary as depicted in Figure 5.4. The switches S_1 - S_4 have a constant duty cycle $D = 50\%$ and the voltage regulation is achieved by adjusting the phase angle, δ between the two legs. The output voltage V_{IPT} depends on the switching states of the first and second legs and takes any one value from the three possible voltage levels $+V_{DC}$, zero or $-V_{DC}$ at a given switching instant.

The switching states of the first and third legs determines the level of capacitive link voltage V_{CPT} from $+V_{DC}$, zero or $-V_{DC}$ at a given switching instant. The first leg switched at 85 kHz serves as the reference leg and the third leg switched at 1 MHz drives the CPT system. Further, the CPT system is regulated by the duty cycle (D_{CPT}) variation of complementary switches S_5 and S_6 on the third leg. For one switching cycle of S_1 and S_2 ,

he switches S_5 and S_6 have several switching cycles as depicted in Figure 5-4 which depends on the switching frequency of CPT. Thus, for the period in which S_1 is on, V_{CPT} traverses from zero to $-V_{DC}$ and for the period in which S_2 is on V_{CPT} traverses from zero to $+V_{DC}$ multiple times depending on the states of S_5 and S_6 .

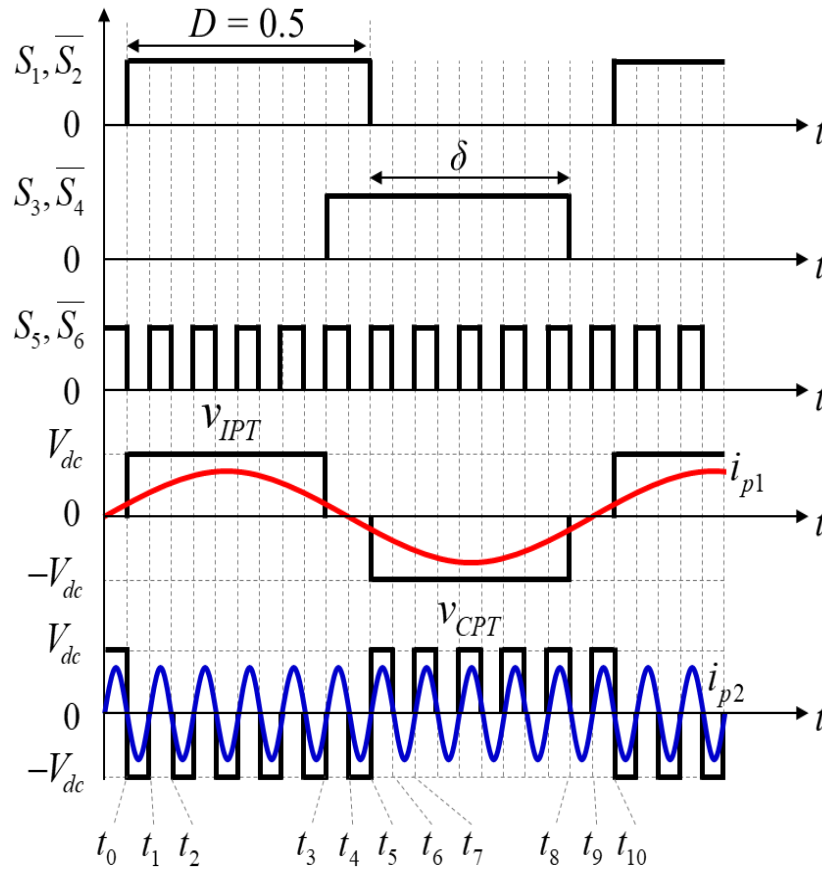


Figure 5-4 Modes of operation.

The modes of operation are as follows:

Mode 1 ($t_0 \leq t \leq t_1$): In this mode, the switches S_1 , S_4 and S_6 are turned on. The inductive link voltage V_{IPT} is at level $+V_{DC}$ and the capacitive link voltage V_{CPT} is at level $-V_{DC}$. The primary current in the IPT circuit, I_{p1} is positive and in phase with V_{IPT} which energizes the resonant tank and flows through the primary coil. This induces the secondary side voltage and the current I_{s1} flows through the secondary coil. The primary current in the CPT circuit,

I_{p2} is negative and in phase with the V_{CPT} . It circulates through S_1 and S_6 . The resonant tank is energized and the plate voltages builds up which allows a displacement current I_{s2} to flow at the secondary side of the CPT system. At the end of this mode, S_6 is turned off.

Mode 2 ($t_1 \leq t \leq t_2$): In this mode, with S_1 and S_4 are still on from the previous mode, S_5 is turned on. The inductive link voltage V_{IPT} is still at level $+V_{DC}$ on the other hand the capacitive link voltage V_{CPT} is at level zero. I_{p2} is positive and circulates through S_5 to S_1 and completes the path. At the end of this mode, S_5 is turned off.

Mode 3 ($t_2 \leq t \leq t_3$): During this time period the modes 1 and 2 repeats until S_4 is turned off.

Mode 4 ($t_3 \leq t \leq t_4$): In this mode, with S_1 still on from the previous mode, S_3 is turned on and the inductive link voltage V_{IPT} is at level zero. I_{p1} circulates through S_1 to S_3 and turns zero. At the end of this mode, S_1 is turned off. For CPT circuit, since S_5 is on at this mode, V_{CPT} is at level zero.

Mode 5 ($t_4 \leq t \leq t_5$): In this mode, the conditions for IPT circuit is same as in the mode 4. However, for CPT circuit, S_6 is on at this mode and V_{CPT} is at level $-V_{DC}$.

Mode 6 ($t_5 \leq t \leq t_6$): In this mode, with S_3 still on from the previous mode, S_2 is turned on and the inductive link voltage V_{IPT} is at level $-V_{DC}$. I_{p1} reverses the direction of flow and conducts through S_2 and S_3 . In the CPT circuit, S_5 is on and V_{CPT} is at level $+V_{DC}$ and I_{p2} is positive. At the end of this mode, S_5 is turned off.

Mode 7 ($t_6 \leq t \leq t_7$): In this mode, with S_2 and S_3 still on from the previous mode, S_6 is turned on and V_{CPT} is at level zero. I_{p2} is negative and completes the path through S_6 and S_2 . At the end of this mode, S_6 is turned off.

Mode 8 ($t_7 \leq t \leq t_8$): During this time period the modes 5 and 6 repeats until S_3 is turned off.

Mode 9 ($t_8 \leq t \leq t_9$): In this mode, the switch S_2 is on from the previous mode and now S_4 is turned on and the inductive link voltage V_{IPT} is at level zero. I_{p1} circulates through S_2 to S_4 and turns zero. For CPT circuit, since S_6 is on at this mode, V_{CPT} is at level $+V_{DC}$.

Mode 10 ($t_9 \leq t \leq t_{10}$): In this mode, the conditions for IPT circuit is same as in the mode 9. However, for CPT circuit since S_6 is on at this mode, V_{CPT} is at level zero. At the end of this mode, S_2 is turned off. In the next switching instant, S_1 is on and the circuit returns to mode 1 and a new cycle begins.

5.3 Steady state analysis

In this section, the steady-state model of the proposed three-leg inverter is derived.

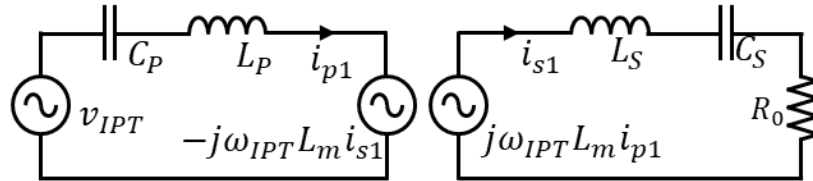


Figure 5-5 Equivalent circuit of the inductive link.

For the steady state analysis, the fundamental harmonic model is adopted with the following assumptions:

- 1) All switches and diodes are considered to be ideal;
- 2) The dead time is neglected;
- 3) Parasitic resistances of inductors and capacitors are ignored;

4) The quality factor of the CPT and IPT systems are considered to be high in order to achieve sinusoidal currents at the inductive and capacitive links.

Figures 5.5 and 5.6 show the equivalent circuits of the inductive and capacitive links respectively. In order to minimize the VA rating of the converter and maximize the power transfer capability the primary and secondary resonant circuits at IPT and CPT links are tuned to the respective angular switching frequency $\omega_{IPT(s)}$ and $\omega_{CPT(s)}$ (5.1-5.2).

$$\omega_{IPT(s)} = \frac{1}{\sqrt{L_p C_p}} = \frac{1}{\sqrt{L_s C_s}} \quad (5.1)$$

$$\omega_{CPT(s)} = \frac{1}{\sqrt{L_1 C_1}} = \frac{1}{\sqrt{L_2 C_2}} \quad (5.2)$$

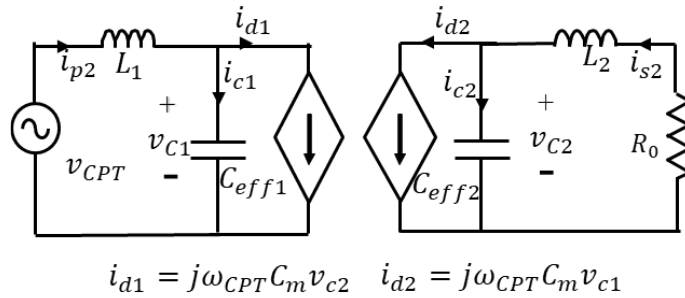


Figure 5-6 Equivalent circuit of the capacitive link.

Here L_p and L_s are the self-inductances of the primary and secondary coils and C_p and C_s are the primary and secondary compensation capacitors of the inductive link. C_1 and C_2 are the primary and secondary compensation capacitors and L_1 and L_2 are the primary and secondary compensation inductors of the capacitive link.

The primary link voltages, v_{IPT} and v_{CPT} , are bipolar and unipolar square waves respectively and they can be approximated to their fundamental components. The time domain expressions are given in (5.3-5.4).

$$v_{IPT} = \frac{4V_{dc}}{\pi} \sin \pi \delta \sin \omega_{IPT(s)} t \quad (5.3)$$

$$v_{CPT} = \frac{2V_{dc}}{\pi} \sin \pi D_{CPT} \sin \omega_{CPT(s)} t \quad (5.4)$$

The secondary side common link voltage v_L , (see Figure 5.3) at the input of the rectifier which has both high and low frequency components from inductive and capacitive links is expressed as in (5.5) where θ is the initial phase of the secondary side voltage.

$$v_L = \frac{4V_0}{\pi} \sin((\omega_{IPT(s)} + \omega_{CPT(s)})t + \theta) \quad (5.5)$$

The primary and secondary currents at the input and output of the IPT system (i_{p1} and i_{s1}) is expressed in (5.6-5.7) as it is the same as link currents due to series compensation.

$$i_{p1} = \frac{v_L}{j\omega_{IPT(s)} L_m} = \frac{4V_0}{\pi\omega_{IPT(s)} L_m} \sin((\omega_{IPT(s)} + \omega_{CPT(s)})t + \theta) - \frac{\pi}{2} \quad (5.6)$$

$$i_{s1} = -\frac{v_{IPT}}{j\omega_{IPT(s)} L_m} = \frac{4V_{dc} \sin \pi \delta}{\pi\omega_{IPT(s)} L_m} \sin(\omega_{IPT(s)} t + \frac{\pi}{2}) \quad (5.7)$$

The primary and secondary currents at the input and output of the CPT system (I_{p2} and I_{s2}) is the sum of displacement current (i_d) through the plate pair and the current through the compensation capacitor bank (i_c). Since $i_d \ll i_c$, i_{p2} and i_{s2} can be approximated as in 5.8 and 5.9 respectively.

$$i_{p2} = i_{d1} + i_{c1} = j\omega_{CPT(s)}C_m v_{C2} + j\omega_{CPT(s)}C_{eff1}v_{C1} \cong j\omega_{CPT(s)}C_{eff1}v_{C1} \quad (5.8)$$

$$i_{s2} = i_{d2} + i_{c2} = j\omega_{CPT(s)}C_m v_{C1} + j\omega_{CPT(s)}C_{eff1}v_{C2} \cong j\omega_{CPT(s)}C_{eff1}v_{C2} \quad (5.9)$$

After removing the high frequency components, the system power is approximated to P_{IPT} and P_{CPT} as given in (5.10-5.11). The final power relation of HPT system is the sum of P_{IPT} and P_{CPT} .

$$P_{IPT} = v_{IPT} i_{p1} = \frac{4V_{dc}}{\pi} \sin \pi \delta \frac{4V_0}{\pi \omega_{IPT(s)} L_m} \quad (5.10)$$

$$P_{CPT} = v_{CPT} i_{p2} = \frac{2V_{dc}}{\pi} \sin \pi D_{CPT} \omega_{CPT(s)} C_{eff1} v_{C2} \quad (5.11)$$

$$P_{HPT} = P_{IPT} + P_{CPT} \quad (5.12)$$

From (5.10), the IPT system power is controlled by the phase shift factor δ between first and second legs (see Figure 5.4) of the inverter and CPT system power is controlled by the duty cycle D_{CPT} of the switches in the third leg (5.11). The maximum power transfer condition for HPT system is when $\delta = 0.5$ and $D_{CPT} = 0.5$.

5.4 System Design and Simulation Results

5.4.1 Design of IPT system

From Figure 5.3, the input power $P_{IPT(p)}$ at the primary side of the inductive link is determined by the full bridge inverter formed by switches S_1 , S_2 , S_3 and S_4 and is given in (5.13). Here, V_{dc} is the dc link voltage, $V_{IPT(p)}$ is the fundamental RMS voltage and $I_{IPT(p)}$ or I_{p1} is the fundamental RMS current at the primary side of the IPT system.

$$P_{IPT(p)} = V_{IPT(p)} I_{IPT(p)} = \frac{4V_{dc} I_{p1}}{\pi\sqrt{2}} \quad (5.13)$$

$P_{IPT(s)}$ is the power received at the secondary side of the inductive link as given in (5.14). Here, V_0 is the output voltage across the load R_0 , $V_{IPT(s)}$ is the fundamental RMS voltage and $I_{IPT(s)}$ or I_{s1} is the fundamental RMS current at the secondary side of the IPT system.

$$P_{IPT(s)} = V_{IPT(s)} I_{IPT(s)} = \frac{4V_0 I_{s1}}{\pi\sqrt{2}} \quad (5.14)$$

The coupler at the inductive ac link is represented by primary self-inductance L_p , secondary self-inductance L_s and the mutual inductance L_m . Depending on the power requirement of the application, the power transfer across the link, $P_{IPT(l)}$ is decided. From the desired amount of power transfer $P_{IPT(l)}$ the required mutual inductance L_m is found in (5.15) where ω_{IPT} is the angular resonant frequency of the circuit (5.22), and I_{p1} and I_{s1} are the primary and secondary rms currents (5.16-5.17).

$$L_m = \frac{P_{IPT(l)}}{\omega_{IPT(s)} I_{p1} I_{s1}} \quad (5.15)$$

$$I_{p1} = \frac{4V_0}{\pi\omega_{IPT} L_m} \quad (5.16)$$

$$I_{s1} = \frac{4V_{dc}}{\pi\omega_{IPT} L_m} \quad (5.17)$$

The secondary self-inductance L_s (5.19) depends on the secondary side quality factor, Q_s (typical range ~ 2-10), the equivalent load R_0 (5.18) and resonant frequency ω_{IPT} (5.23).

The coupling coefficient k is selected to be less than the critical coupling coefficient k_c based on the recommendations to avoid bifurcation phenomena [120]. It also decides the range of the power transfer distance.

$$R_0 = \frac{8}{\pi^2} R_L \quad (5.18)$$

$$L_s = \frac{Q_s R_0}{\omega_{IPT}} \quad (5.19)$$

$$L_p = \frac{L_m^2}{L_s k^2} \quad (5.20)$$

The primary self-inductance L_p is then computed from (5.20). The relation between resonant frequency and the corresponding resonant tank elements at the primary side ($f_{IPT(p)}$) is given in (5.21) and at the secondary side ($f_{IPT(s)}$) is given by (5.22). The inverter switching frequency is allowed to slightly deviate from the resonant frequency in order to enable soft switching.

$$f_{IPT(p)} = \frac{1}{2\pi\sqrt{L_p C_p}} \quad (5.21)$$

$$f_{IPT(s)} = \frac{1}{2\pi\sqrt{L_s C_s}} \quad (5.22)$$

$$\omega_{IPT} = 2\pi f_{IPT(p)} = 2\pi f_{IPT(s)} \quad (5.23)$$

The series-series compensated resonant tank is completed by capacitor banks C_p and C_s on primary and secondary respectively. The values of capacitors are designed to create proper resonance with the coupler at the desired resonant frequency f_{IPT} . The compensation network compensates the reactive power, reduces the VA rating of inverter switches at the primary side and increases the power transfer capability at the secondary side. By equating the power expressions in (5.13-5.15), the IPT system power is given in (5.24).

$$P_{IPT} = \frac{8V_{dc}V_0}{\pi^2\omega_{IPT}L_m} \quad (5.24)$$

Once the circuit parameters are determined, the primary coil and secondary coil dimensions need to be finalized to form the required L_p and L_s . The selected shape of the coil is Archimedean spiral (see Figure 5.7).

$$L = \frac{N^2 a^2}{8a+11c} \quad (5.25)$$

$$a = \frac{D_{out} + D_{in}}{4} \quad (5.26)$$

$$c = \frac{D_{out} - D_{in}}{2} \quad (5.27)$$

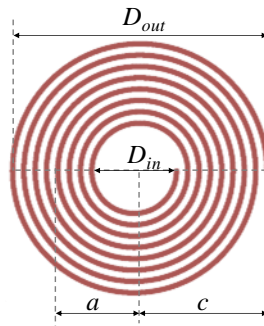


Figure 5-7 Archimedean spiral.

The geometrical parameters for this shape are derived from the Wheeler's inductance formula given in (5.25-5.27) [121]. Here in the formula, the planar coil outer diameter D_{out} and inner diameter D_{in} are used in inches and L is in μH . The value of D_{out} can be decided from the required air-gap between the coupler. From the literature, it is found that the fundamental height of the flux path in this shape is about one fourth of the coil outer diameter. The number of turns, N in the coil are assumed as single equivalent turn at first and then by arithmetic progression, D_{in} and N are determined for the given value of L .

5.4.2 Design of CPT system

The capacitance of each of the square parallel plate coupling structure must incorporate the fringing field effects which are prominent when the plate dimension and power transfer distance is comparable. Thus the coupling capacitance is found using (5.28) where b is the ratio of power transfer distance (d_{air}) to plate width (l). The plate pair capacitance C_{1pp} and C_{2pp} are found from the relation (5.28).

$$C_{plate-pair} = (1 + 2.343b^{0.891}) \epsilon_0 \epsilon_r l^2 / d_{air} \quad (5.28)$$

The voltage stress developed across the plates is also a critical design factor which is given by (5.29). For a given current rating I , the voltage V developed across the interface is controlled either by increasing the operating frequency ω or by increasing the mutual capacitance C_M . In addition, by using appropriate compensation technique, the current I flowing through the link can also be controlled.

$$V = \frac{I}{\omega C_M} \quad (5.29)$$

Thus, in order to decrease the plate voltage stress and increase the power transfer capability over large air-gap, a dual LC compensation is realized by inductor L_1 and additional capacitor C_1 at the primary side and by inductor L_2 and additional capacitor C_2 at the secondary side of the CPT system. This addition of capacitor to the series compensation inductor helps to reduce the voltage stress on the resonant inductor and plate pair especially when used for high power transfer and large air gap applications like electric vehicle charging.

The capacitances C_{1pp} , C_{2pp} and mutual capacitance C_M are fixed once the coupler dimensions are finalized according to the application requirement. Therefore, system power transfer can then be controlled by adjusting C_1 and C_2 . The effective capacitance, C_{eff1} is the sum of C_1 and C_{1pp} . Similarly, C_{eff2} is the sum of C_2 and C_{2pp} . Further, the values of inductors are designed to create proper resonance with the effective capacitance at the desired frequency f_{CPT} which in turn compensates for the reactive power.

The input power $P_{CPT(p)}$ at the primary side of the capacitive link is controlled by the half bridge inverter formed by switches S_5 and S_6 and expressed in (5.30). Here, V_{dc} is the DC link voltage, $V_{CPT(p)}$ is the fundamental RMS voltage and $I_{CPT(p)}$ or I_{p2} is the fundamental RMS current at the primary side of the CPT system as given in (5.31).

$$P_{CPT(p)} = V_{CPT(p)} I_{CPT(p)} = \frac{2V_{dc} I_{p2}}{\pi\sqrt{2}} \quad (5.30)$$

$$I_{p2} = \omega_{CPT} C_{eff1} V_{c1} \quad (5.31)$$

As shown in Figure 5.3, the capacitive link with a mutual capacitance C_M is formed by parallel plate pairs C_{1pp} and C_{2pp} .

The power received at the secondary side of the capacitive link is given as $P_{CPT(s)}$ in (5.32) where V_0 is the output voltage at the load, $V_{CPT(s)}$ is the fundamental RMS voltage and $I_{CPT(s)}$ or I_{s2} given in (5.33) is the current at the secondary side of the CPT system.

$$P_{CPT(s)} = V_{CPT(s)} I_{CPT(s)} = \frac{4V_0 I_{s2}}{\pi\sqrt{2}} \quad (5.32)$$

$$I_{s2} = \omega_{CPT} C_{eff2} V_{c2} \quad (5.33)$$

$$P_{CPT(l)} = \omega_{CPT} C_m V_{c1} V_{c2} \quad (5.34)$$

$$P_{CPT(p)} = P_{CPT(l)} = P_{CPT(s)} \quad (5.35)$$

$$P_{CPT} = \frac{4\omega_{CPT} C_{eff1} C_{eff2} V_{dc} V_0}{\pi^2 C_m} \quad (5.36)$$

The power transferred through the coupler/link, $P_{CPT(l)}$ is expressed in (5.34) where ω_{CPT} is the angular resonant frequency, C_m is the mutual inductance, V_{c1} and V_{c2} are the link voltages across C_{eff1} and C_{eff2} of the CPT system. By rearranging the power expressions as in (5.35), the CPT system power can be written as (5.36).

5.5 Simulation Results

As per the design methodology discussed in section 5.4 and 5.5 IPT and CPT circuit parameters are found respectively for a power level of 500 W with input voltage, V_{dc} at 85 V and an output voltage V_o of 72 V. The IPT and CPT circuits are then combined using three leg inverter to form HPT system. The list of circuit parameters are given in Table 5.2. Further, the HPT system with designed circuit parameters is simulated in PSIM.

Table 5-2 HPT System Specifications

Parameters	Symbol	Values
Maximum output power	P_o	500 W
Output voltage	V_o	72 V
Input voltage	V_{dc}	85 V
IPT circuit elements		
IPT switching frequency	f_{IPT}	85 kHz
Dead time	t_d	0.2 μ s
Primary coil inductance	L_p	169 μ H
Secondary coil inductance	L_s	73.4 μ H
Mutual inductance	L_M	22.2 μ H
Primary compensation capacitor	C_p	20.8 nF
Secondary compensation capacitor	C_s	47.8 nF
CPT circuit elements		
CPT switching frequency	f_{CPT}	1.18 MHz
Dead time	t_d	0.03 μ s
Plate pair capacitance	$C_{1pp} = C_{2pp}$	47 pF
Mutual capacitance	C_M	23.15 pF
Compensation capacitor	$C_1 = C_2$	453 pF
Compensation inductor	$L_1 = L_2$	50.71 μ H

The simulated switching waveforms S_1 - S_6 are given in Figure 5.8. The low frequency pulses S_1 - S_4 are driving the IPT system. S_5 - S_6 are the high frequency pulses that drives the CPT system.

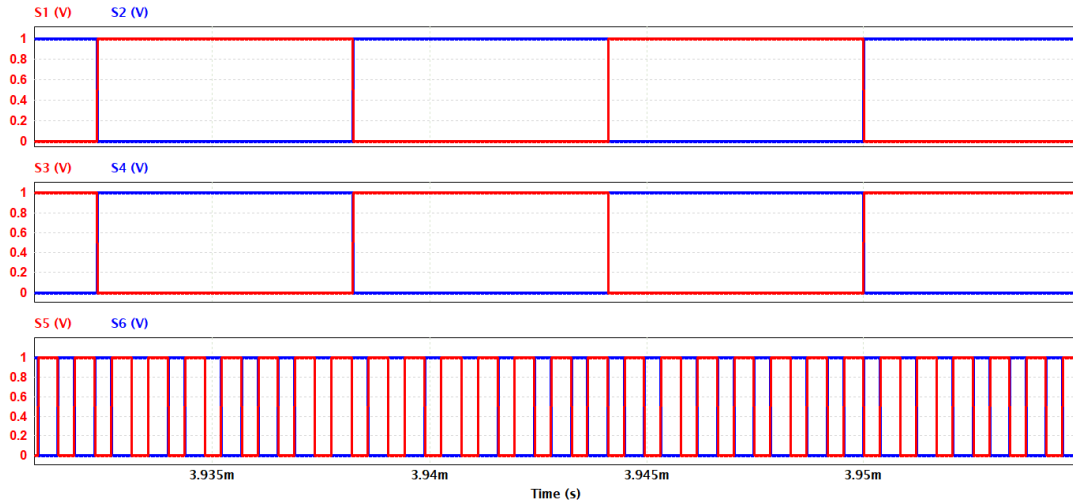


Figure 5-8 Simulation Results (a) Switching pulses at S_1 , S_2 (b) Switching pulses at S_3 , S_4 (c) Switching pulses at S_5 , S_6 .

Figure 5.9 (a) and (b) shows the primary side voltage and current waveforms at inductive and capacitive link respectively. The inductive link input voltage, V_{IPT} , and primary current, I_{p1} , are in phase and the capacitive link input voltage, V_{CPT} , and primary current, I_{p2} , are in phase.

In 5.10(a), the link voltages V_{IPT} and V_{CPT} are shown where the V_{CPT} completes approximately thirteen switching cycles in one time period of V_{IPT} . The frequency ratio (f_{ratio}) is defined as the ratio of CPT and IPT operation frequencies in (5.37).

$$f_{ratio} = \frac{f_{CPT}}{f_{IPT}} = 13 \quad (5.37)$$

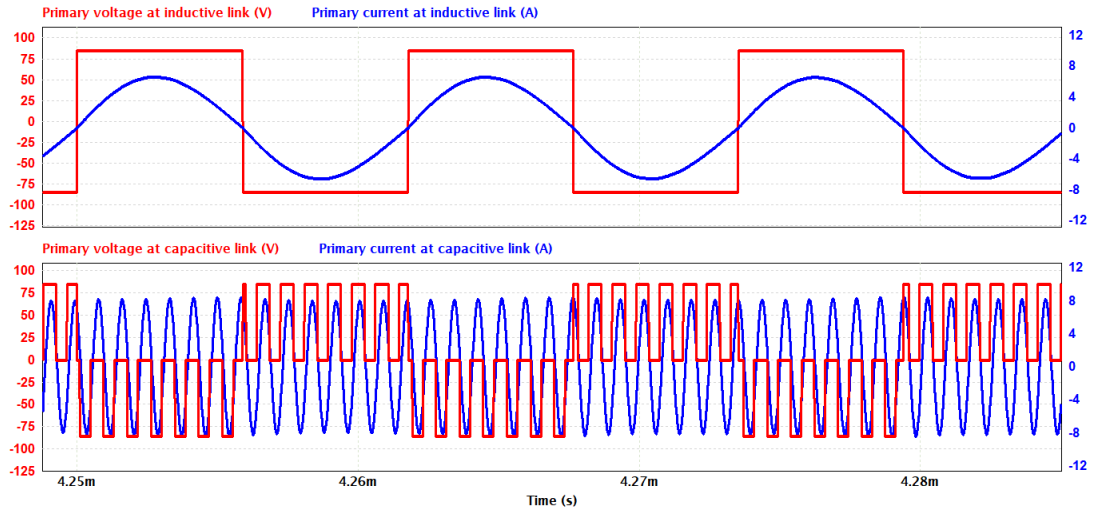


Figure 5-9 Simulation Results (a) Input link voltage, V_{IPT} , primary current, I_{p1} , at inductive link (b) Input link voltage, V_{CPT} , primary current, I_{p2} , at capacitive link.

The primary and secondary current waveforms of IPT is depicted in Figure 5.10(b).

Figure 5.10(c) shows the primary and secondary current waveforms of CPT.

The inductive link input voltage, V_{IPT} , and primary current, I_{p1} , are in phase and I_{p1} and I_{s1} are phase shifted by 90° as evident from the design equation.

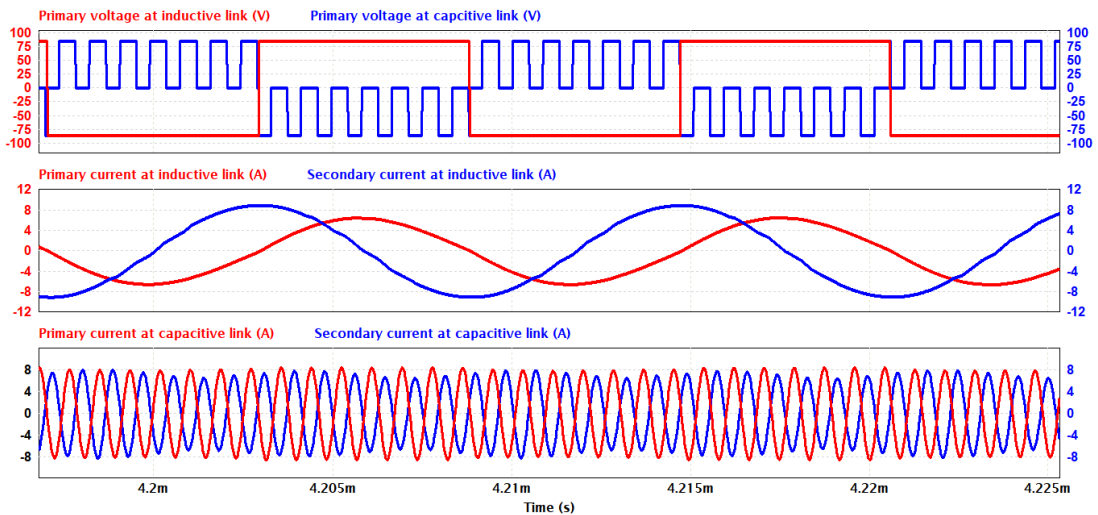


Figure 5-10 Simulation Results (a) Primary side voltage waveforms V_{IPT} and V_{CPT} (b) Primary current, I_{p1} , and secondary current, I_{s1} at inductive link (c) Primary current, I_{p2} , and secondary current, I_{s2} at capacitive link.

Similarly the capacitive link input voltage, V_{CPT} , and primary current, I_{p2} , are in phase and I_{p2} and I_{s2} are phase shifted by 180° .

In Figure 5.11 secondary side voltage and current waveforms are depicted. As it can be seen, both V_{s1} / V_{s2} and I_{total} contains high frequency and low frequency components which are contributed by the capacitive and inductive links respectively. The rectified output voltage and current waveforms are also given.

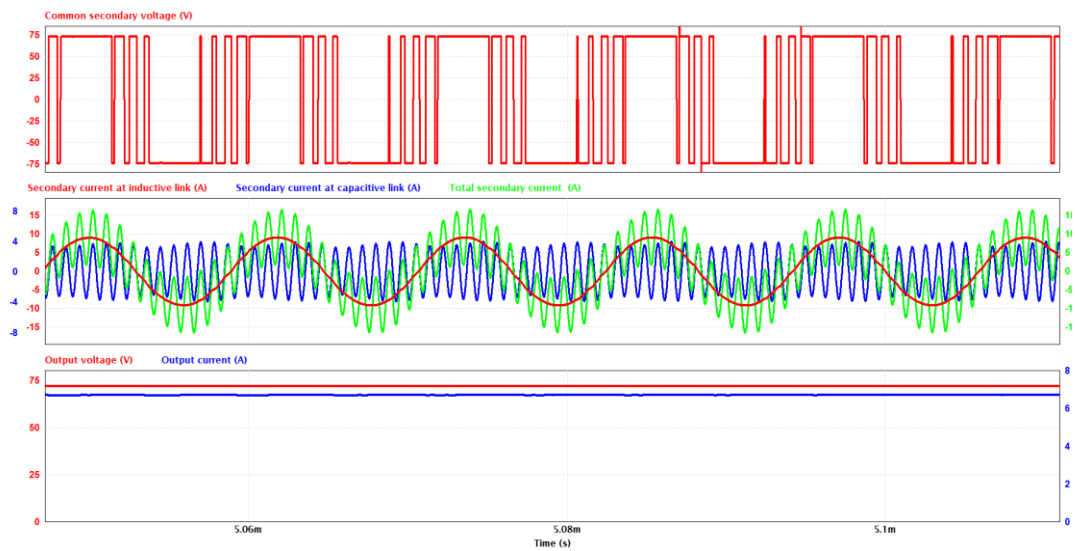


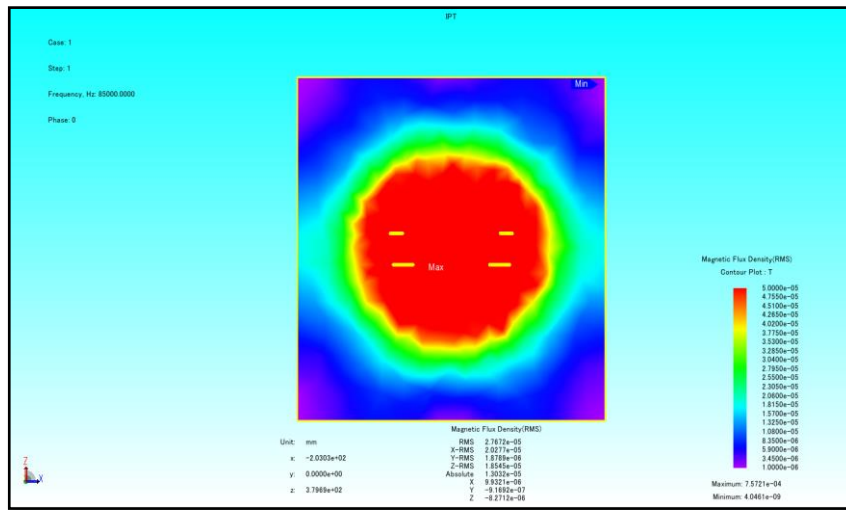
Figure 5-11 Simulation results (a) Common voltage at secondary side (V_{s1} / V_{s2}) (b) Secondary side currents (I_{s1} , I_{s2} and I_{total}) (c) Output voltage and current (V_o and I_o).

Table 5-3 Peak voltage and current stress in IPT components

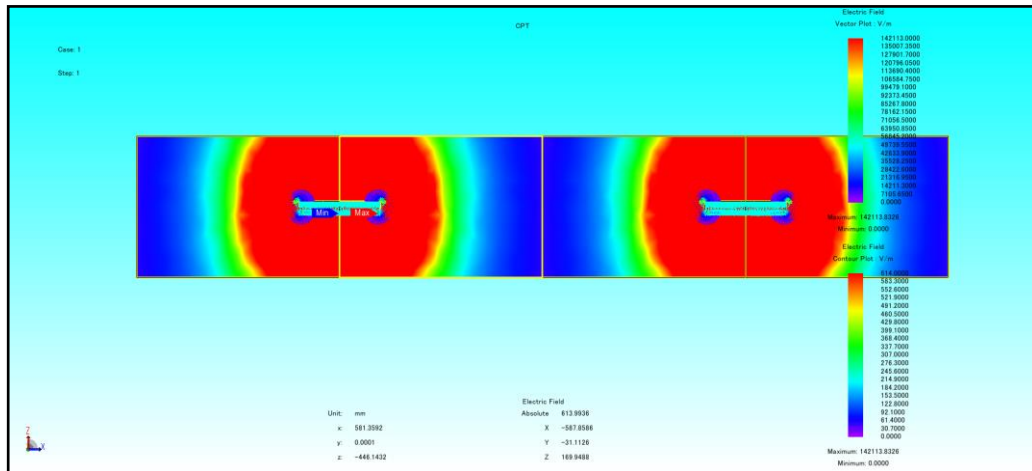
Components	C_P	Primary Coil	Secondary coil	C_S
Voltage (V)	638	725	452	350
Current (A)	9.06	9.06	7.07	7.07

Table 5-4 Peak voltage and current stress in CPT components

Components	L ₁	C ₁	Plates	C ₂	L ₂
Voltage (V)	2281	2221	523	2140	2114
Current (A)	7.51	7.33	0.17	7.14	7.31



(a)



(b)

Figure 5-12 Field distribution simulated in JMag (a) Magnetic flux density at the Inductive link(μ T) (b) Electric field at Capacitive link (V/m) components.

The peak voltage and current stress across the link and the compensation components for IPT and CPT are given in Tables 5.3 and 5.4 respectively for a power transfer level of 500 W. In Table 5.4, due to the use of dual LC compensation, the voltage stress across the plates is reduced considerably compared to the series compensated CPT system.

The leakage field influence around the couplers is simulated in JMAG with these peak voltage and current values. The ICNIRP 2010 (Table 2.7) permissible magnetic field limit of 27 μT is observed at 190 mm from the edge of the inductive link. The absolute permissible electric field of 614 V/m as per IEEE C95.1 (Table 2.6) limits is observed at a distance of 281 mm from the edge of the capacitive link. (see Figures 5.12 (a) and (b)).

5.6 Experimental Outcomes

5.6.1 Experimental setup

The experimental prototype of the HPT system is built in the lab with the circuit parameters given in Table 5.2. The HPT system stages include power supply, three leg inverter, inductive and capacitive link, compensation circuit, rectifier, filter and electronic load (see Figure 5.13). A Magna-Power Electronics programmable DC power supply and a 63800 series programmable AC/DC electronic load from Chroma System Solution were used at the supply side and load side respectively. The first two legs of the three leg inverter is configured using two silicon carbide (SiC) MOSFET high-frequency half-bridge evaluation boards that uses C3M0120090J MOSFETs from CREE in a 7L D2PAK package (CRD-5FF0912P) to drive the IPT system. A half-bridge evaluation board from GaN Systems featuring 650V E-HEMT GS66508T (30A/50m Ω) transistor forms the third leg to drive the CPT system.

The inductive link is made up of planar Archimedean spiral coil pairs separated by a distance of 100 mm. The coil material is 8 AWG type II 5×5×42/32 Litz wire. The outer diameter of the primary coil is 460 mm and the inner diameter is 280 mm. The number of turns in the primary coil is 17. The secondary coil contains ten turns and its outer and inner diameter are 460 mm and 354 mm respectively. The IPT system's compensation circuitry consists of series connected film capacitor banks C_p and C_s at each side that ensure the required capacitance values, voltage and current ratings. The capacitive link is made up of two pairs of square aluminum plates of length (l) 600 mm separated at a 100 mm power transfer distance. For the CPT system's compensation circuitry, high-frequency thin-film external capacitor banks C_1 and C_2 are connected at primary and secondary side. The resonant tank is then completed by the inductors L_p and L_s that are made with AWG 8 Litz-wire wound on an air core. The Texas Instruments TMS320F28379D microcontroller with 200 MHz clock frequency is used to generate the PWM signals to drive the inverter switches externally. A dead time of 100 ns is kept in first two legs that drive the IPT circuit and a dead time of 30ns is chosen for the last leg which drives the CPT circuit. At the receiver side, the rectifier is implemented using a SiC schottky diode rectifier-bridge from GlobalPower and the rectifier output is smoothed by a low pass capacitive filter.

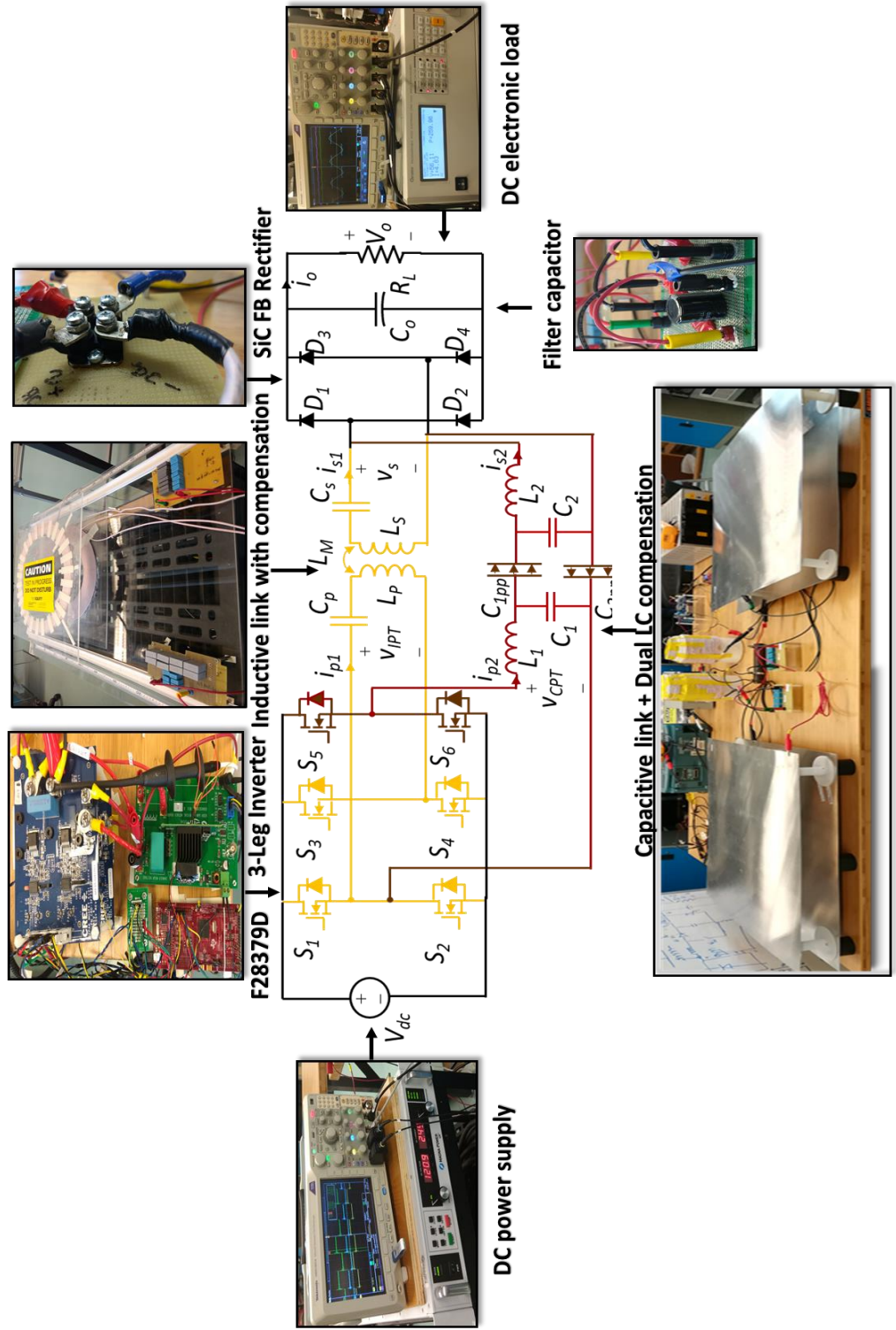


Figure 5-13 Photo of the experimental setup.

5.6.2 Experimental results

The switching pulses at the upper switches (S_1 , S_3 and S_5) of each leg is shown in Figure 5.14. As it can be seen, first two legs are switching at 85 kHz and the third leg is switched at 1.18 MHz. The phase shift angle between first and second leg is kept at 180° which ensures the maximum span of inductive link voltage, V_{IPT} .

The inductive and capacitive link voltages (V_{IPT} , V_{CPT}) are depicted in Figure 5.15. The waveforms show that in one switching cycle of V_{IPT} , there are around thirteen cycles of V_{CPT} whose polarity is positive for the negative half cycle of V_{IPT} and vice versa.

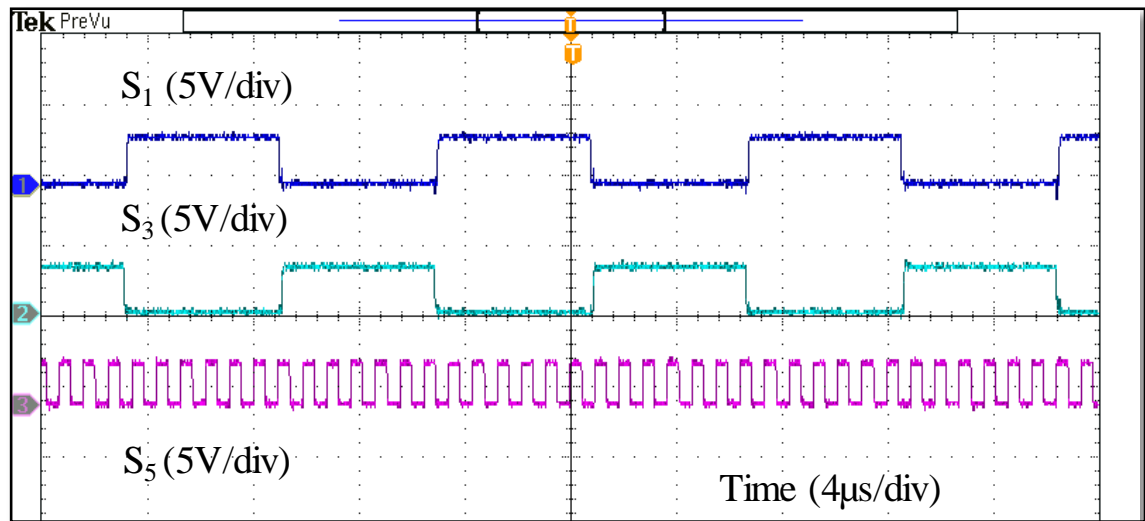


Figure 5-14 Switching pulses at S_1 , S_3 and S_5 (upper switches at each leg) (5 V/div).

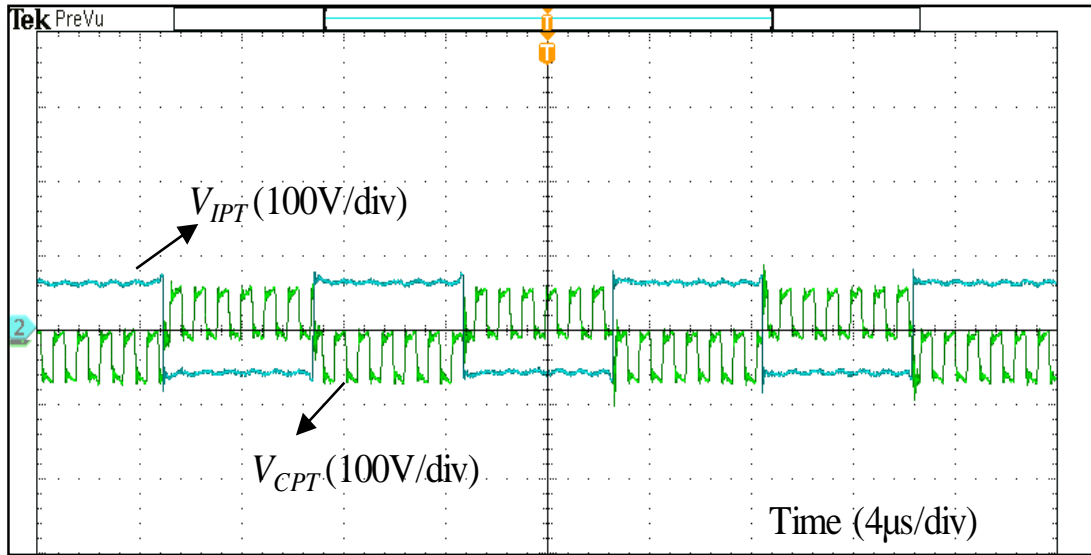


Figure 5-15 Inductive link voltage, V_{IPT} (100 V/div), V_{CPT} (100 V/div).

Figure 5.16 shows the primary side voltage and current waveforms. V_{IPT} and I_{p1} / I_{IPT} are the voltage and current measured at the input of the IPT system.

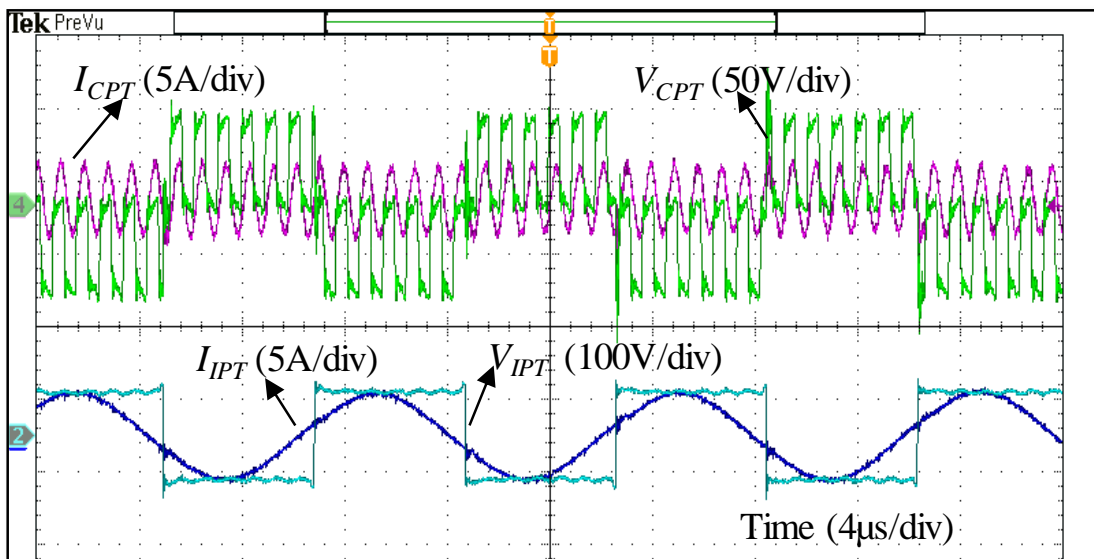


Figure 5-16 Voltage and current waveforms at the primary side: V_{CPT} (50 V/div), I_{CPT} (5 A/div), V_{IPT} (100V/div), I_{IPT} (5 A/div).

V_{CPT} is the voltage measured across the primary side of the CPT system and I_{p2} is the current flowing through it. The secondary side waveforms are depicted in Figure 5.17. As the secondary side of IPT and CPT systems are parallel connected, the secondary voltage V_s and total current I_s contains low frequency and high frequency components corresponding to IPT and CPT systems respectively.

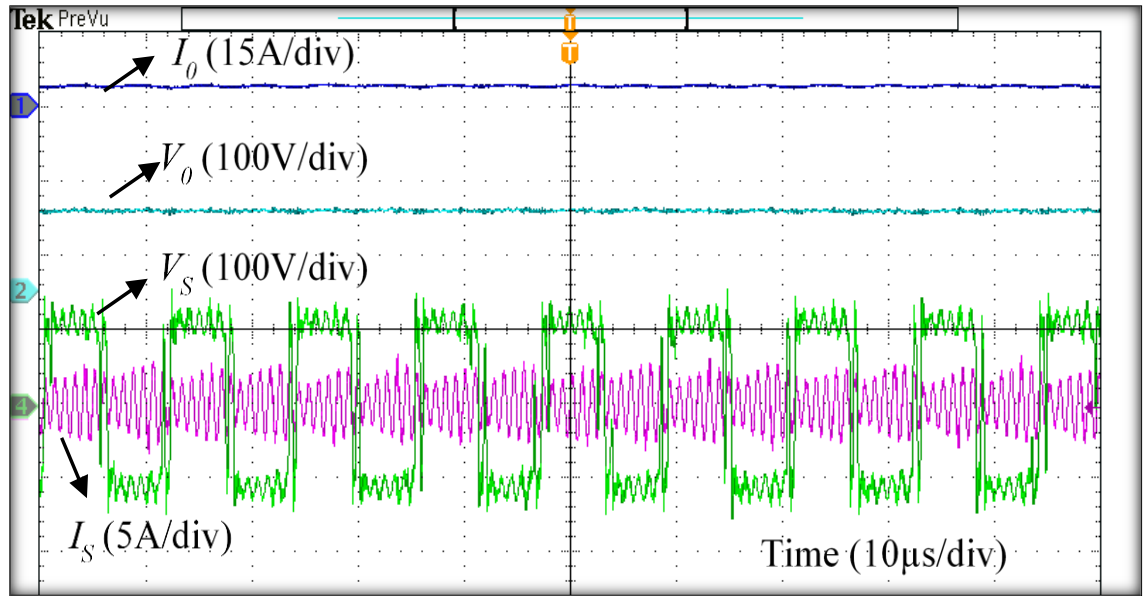


Figure 5-17 Voltage and current waveforms at the secondary side: V_s (100 V/div), I_{s2} (5 A/div), V_0 (100V/div), I_0 (5 A/div).

V_0 and I_0 are the rectified and filtered voltage and current waveforms measured across the load resistance. The efficiency levels for 500W experiment prototype is 85.4% and the simulated efficiencies at higher power levels with losses incorporated is above 90%.

5.7 Sensitivity analysis

An important aspect of wireless power transfer systems are their sensitivity to alignment variations. This is because the efficiency and power transfer is influenced by the misalignment percentage. The misalignment cases are discussed in section 2.1.2. For most

of the applications the vertical alignment or power transfer distance is fixed and hence it is assumed to be constant in this analysis. However, the horizontal alignment is highly dependent on the user. In case of EV application, several positioning mechanisms can be adopted to assist the driver while parking the car over the charging pad [14], [59].

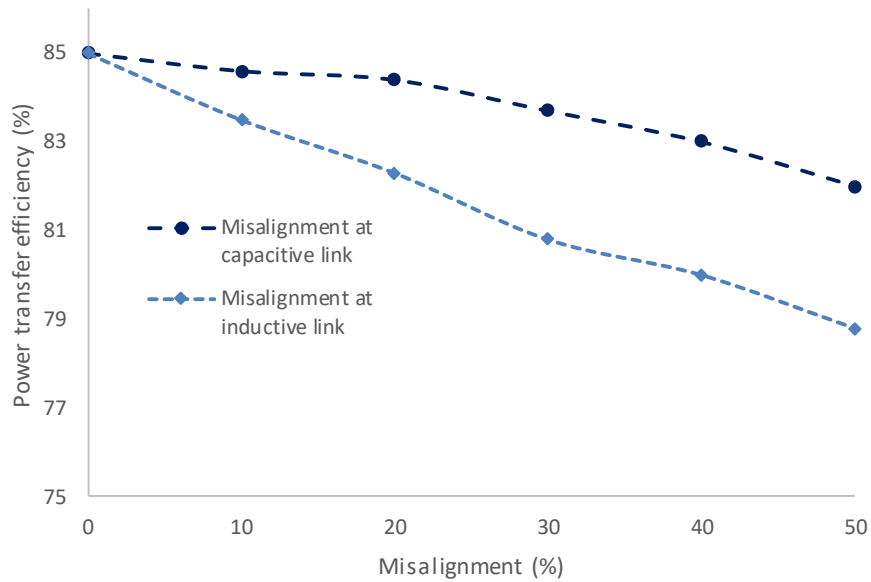


Figure 5-18 HPT system performance for individual misalignment at capacitive and inductive link.

The overall power transfer efficiency of the HPT system with respect to the misalignment percentage at the inductive and capacitive link individually is given in Figure 5.18. Here, since the dimensions of the inductive and capacitive coupler are different, the misalignment at each link is expressed in percentage. As it can be observed, the HPT system efficiency remained in the range of 85% up to 20% misalignment at capacitive link and then reduced linearly to 82% for a 50% misalignment. However, there is a linear efficiency reduction in the HPT system as the percentage misalignment progressed at the inductive link only. This

implies that the capacitive link misalignment performance is stable compared to the inductive link.

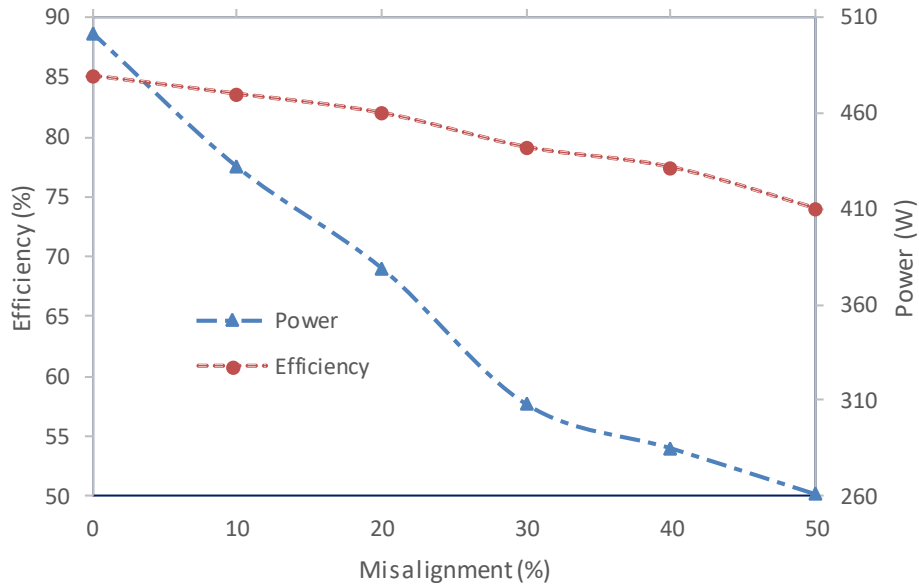


Figure 5-19 HPT system power and efficiency curves for simultaneous misalignment in both inductive and capacitive links.

Figure 5.19 illustrates the power and efficiency curves when the misalignment occurs at both links simultaneously which can be considered as the worst case scenario. The maximum efficiency of 85% is attained at a power transfer level of 500 W and it remains above 80% until mutual misalignment reaches 30% at both links. Similarly, the power transferred reduces linearly from 500W at zero misalignment at both links to 261 W at 50% misalignment at both links.

Figure 5.20 shows the power transfer ratio between inductive and capacitive link with respect to the combined misalignment. The relation of HPT power transfer ratio can be derived as in (5.38).

$$\text{Power transfer ratio} = \frac{P_{IPT}}{P_{CPT}} = \frac{2C_m}{\omega_{IPT} \omega_{CPT} L_m C_{eff1} C_{eff2}} \quad (5.38)$$

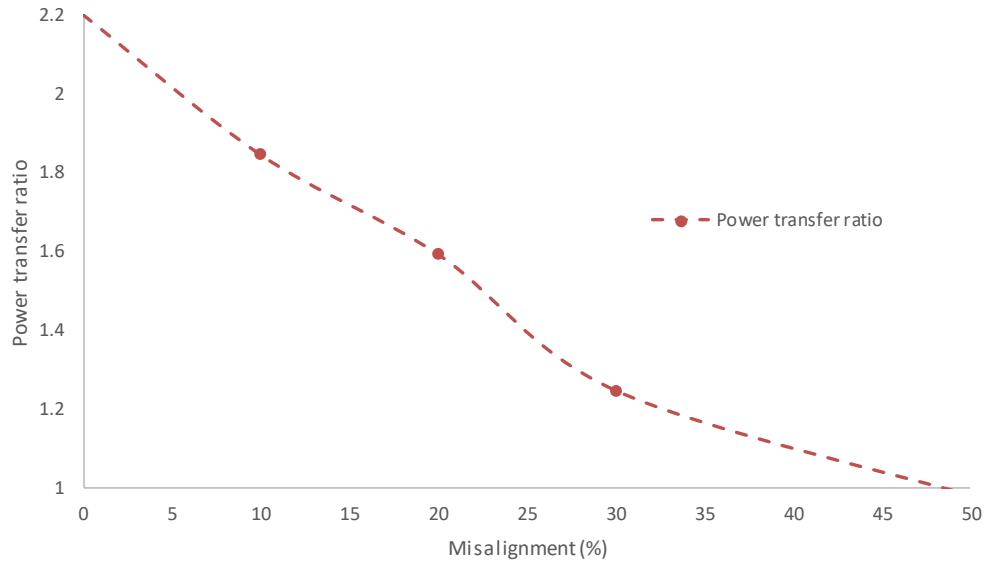


Figure 5-20 Power transfer ratio between inductive and capacitive system with respect to misalignment.

As designed, the power transfer ratio of inductive to capacitive link is two at zero percent misalignment. That means, IPT system transfers twice the power as that of CPT system. As the misalignment increases, the ratio reduces and at 50% misalignment, the IPT and CPT system transfers almost the same amount of power, as the power transfer ratio turns one. The curve shape is not straight line as it incorporates the small misalignment errors during measurements.

5.8 Loss distribution

The loss distribution is illustrated in Figure 5.21. The system power loss in the HPT system is determined across the switching devices, passive components and the link by incorporating thermal modules and internal resistances from datasheets in PSIM

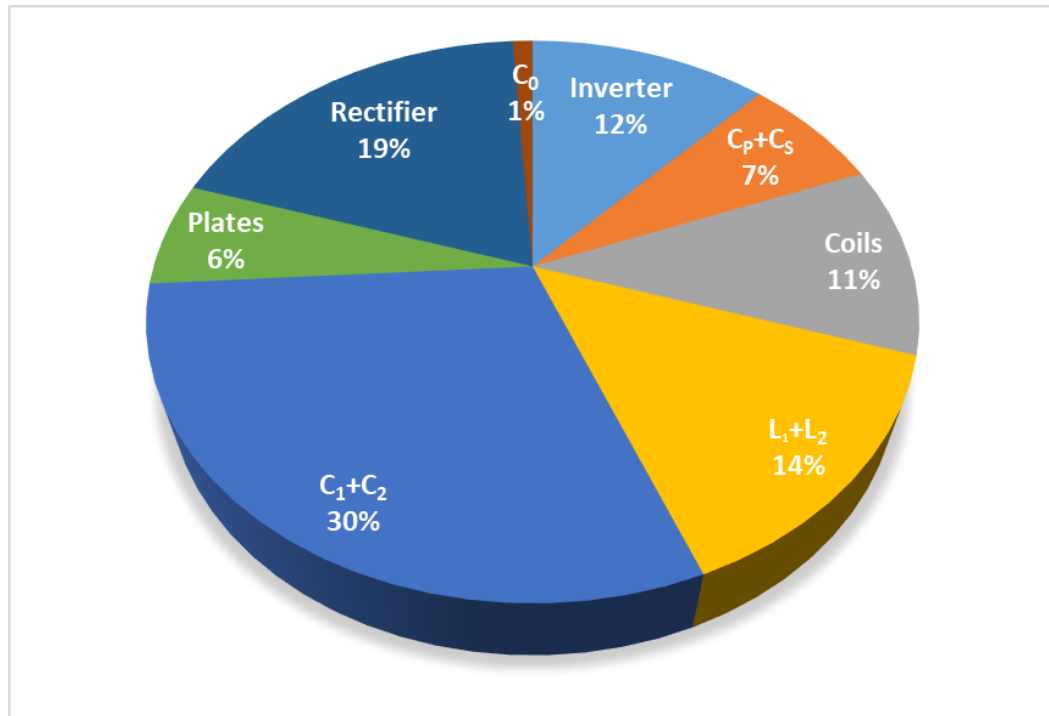


Figure 5-21 Loss distribution.

simulation. The switching and conduction losses in the three leg inverter is 12% which is mainly contributed by first and third leg due to the influence of high frequency component in these legs. The losses across the plates are comparatively less than the coil losses. This is due to the lower value of displacement current across the plates compared to the higher currents present in the coil. The overall CPT system losses are dominant due to the higher dissipation in compensation capacitors C_1 and C_2 which accounts for 30%. This could be reduced by proper selection of thin film capacitors with lower ESR. In a recent study [122],

by utilizing split-inductor matching networks, some of the parasitic capacitance effects are nullified and the remaining parasitic capacitances substituted the need for external capacitors in the system. Thus enhancing the performance and reliability of the large air gap CPT system.

5.9 Comparison with the existing HPT topologies

Table 5-5 Comparison with existing HPT topologies

WPT Technology		Frequency (kHz)	Power transfer percentage (%)	Power Level (kW)	Efficiency (%)	Plate voltage stress (kV)	Safe operating distance away from the coupler (mm)	Power Converter	Link Architecture	Ref.
HPT-1	IPT	1000	72	3	94.5	4.9	600	Full Bridge	Dependent	[94]
	CPT		28				700			
HPT-2	IPT	800	~50	1.1	91.9	2.9	--	Full Bridge	Dependent	[97]
	CPT						--			
HPT-3	IPT	85	66.66	0.5	85.4	0.52	190	Three-leg	Modular	Proposed
	CPT	1180	33.33				281			

A comparison with existing HPT topologies is outlined in Table 5.5. The existing HPT systems focused on creating a combined resonant tank for the mutual operation of both links creating a dependent two channel power transfer through coupling coils and coupling plates. However, the dependency of inductive and capacitive links that accounts for operating the whole HPT system at high frequency (800 kHz - 1 MHz). In these designs, as the link parameters are mutually dependent, parameter variations in inductive or capacitive link can cause the system to deviate from the resonance and in turn affects the power transfer. In addition, the radiations from the IPT and CPT link are high which is evident from the safe operating area around the coupler as given in the Table 5.5 which could be due to the influence of high frequency operation of IPT link and high power rating

at the capacitive link. The surge in power frequency product stimulates the leakage fields at both couplers. Thus, effective shielding techniques are vital in the high power designs.

In the proposed system, the independent operation of inductive and capacitive links is possible as they can be switched at different frequencies. This modular link architecture is therefore a viable solution in combining the IPT and CPT systems. It allows the inductive link to be operated at low frequency and high power level and the capacitive link to be operated at high frequency and low power level. This creates two independent resonant tanks in parallel supplying power to the load. The safe operating area around the coupler is significantly improved and can be further reduced by proper shielding techniques at higher power levels. By connecting an additional rectifier at the secondary side, this HPT system can supply power to additional loads independently. Therefore, modular link architecture will provide a flexible operation of the links and increases the reliability and scalability of the HPT system.

Chapter 6. Conclusions and future work

EV revolution is happening at a much faster rate than the market predictions. The developments in wireless power transfer technology can revolutionize the shift towards transportation electrification hassle free for the society. This thesis tried to explore simple and cost-effective capacitive wireless power transfer technology as a dual of inductive wireless power transfer technology based on various design and implementation characteristics to reveal their benefits and limitations. The outcomes achieved in this thesis are summarized below.

6.1 Conclusions

1. Comparative study of inductive and capacitive wireless power transfer technologies for EV charging applications.

Chapter 2 of the thesis provided a comparative review of inductive and capacitive AC link solutions used in the wireless EV charging. After a brief introduction to IPT and CPT systems respectively, AC link couplers applicable to static and dynamic wireless charging is studied. A relative discussion based on various design and implementation challenges for the inductive and capacitive links differentiated this study from the existing reviews. In addition, the state-of-the-art research on hybrid AC link by utilizing the capability of both inductive and capacitive link in a wireless power transfer (WPT) system is also explored and future directions to implement an HPT system are proposed. This analysis served as a background for the final chapter where a hybrid wireless power transfer system is realized.

2. The capacitive coupler geometry for low to medium power EV applications are evaluated and the influence of dielectrics in a capacitive coupler is explored.

In chapter three, two capacitive coupler geometries, 4x1 column and 2x2 matrix interface applicable to low to medium power applications are evaluated. A case study on UAV charging scenario is conducted. In addition, the influence of introducing dielectrics on capacitive coupler interface is explored and validated through the FEA analysis in JMAG. From the analysis of different coupling interfaces, matrix arrangement provided a higher mutual capacitance than column structure. For low power and small air-gap interface, the effective coupling capacitance is increased at least 11 times with the use of high permittivity dielectrics between the coupling interface provided the area covered by dielectrics is greater than the air-gap area. Moreover, the use of dielectrics gave much larger limits on breakdown voltage at all power transfer distances.

3. A reduced capacitance model for parallel plate configuration in CPT is derived.

A reduced capacitance model for the capacitive power transfer system is discussed in chapter four which is derived from the conventional six capacitance model for the bipolar capacitive link topology. When the separation distance between the same side plate pair is large enough, the effect of same side and cross-coupling capacitances diminishes and the analysis based on a reduced capacitance modelling (RCM) with the two main capacitances can be carried out. A bipolar capacitive link dispersion factor (BCD) defined in this chapter determined the separation distance beyond which RCM can be applied relative to the plate dimensions and power transfer distance. Further analysis showed that, RCM attains the unity voltage gain and load-independent operation at designed resonant frequency. The effectiveness of the model is analyzed and verified experimentally. To validate the RCM analysis, a synchronous buck configured dual LC compensated topology is opted for the implementation of the CPT. The system is switched at 1.18 MHz,

using GaN switches. The effectiveness of the reduced capacitance model is validated experimentally for a power level of 100-200 W and the system achieved 72.12% efficiency at power level 114 W. The results indicated that, reduced capacitance model is suitable over six capacitance modelling for large charging area applications like electric vehicle charging where the separation distance between the same side plate pair is large enough and the effect of the same side and cross coupling capacitances can be circumvented in the analysis.

4. Designed and implemented a hybrid inductive and capacitive system to achieve dual frequency operation, sharing of the system power, modularity and misalignment tolerance.

A hybrid wireless power transfer system (HPT) that uses both capacitive and inductive couplers, for shared power transfer is presented in chapter five. A modular HPT system has been realized using a three-leg inverter topology to combine the inductive and capacitive wireless power transfer system with in their individual operating frequency limits. Adhering to the frequency limits confined the unsafe electromagnetic radiations to a great extent. Two legs of the inverter, switched at 85 kHz, using SiC modules are utilized for IPT and the third leg, switched at 1 MHz, using GaN module is used for CPT. The dual switching frequency operation of the converter to drive electromagnetic and electrostatic fields simultaneously is the novelty in the proposed topology. In addition, this allowed independent compensation techniques to be adopted for IPT and CPT systems bringing the modularity feature in the hybrid wireless power transfer link. The circular inductive link outer diameter is 460 mm and the parallel plate capacitive link dimension is 600 mm x 600 mm. The power transfer distance is 100 mm at both links. The output

power ratio between inductive link to the capacitive link in this HPT system is 2:1. The effectiveness of the proposed topology is validated experimentally and the system prototype achieved 85% efficiency at a power transfer level of 500W. The simulated efficiency for a 1 kW system is 91%. Further, the voltage and current stress across the links are exclusive and improved compared to other HPT systems at similar power levels. The advantages of this HPT system are modular link architecture, improved misalignment performance and distinct frequency of operation for each link which allows inductive link to meet the SAEJ2954 standard limits compared to the existing HPT systems proposed for electric vehicle (EV) charging.

6.2 Future directions

- AC link optimization: By developing different coupler geometry and optimizing the design for various constraints such maximizing system efficiency and power transfer density, minimizing voltage stress and leakage field distribution etc.
- Compensation circuit design: The compensation circuit design can be investigated to increase the power transfer capability of the systems. Investigating on low power dissipating compensation components can improve the system efficiency.
- AC link shielding techniques: Before commercialization of WPT systems, development of effective shielding techniques to tackle the radiated emissions at high power transfer, large air-gap and high switching frequency operation is inevitable.

- Wireless communication link: In order to procure the receiver side information, suitable wireless communication techniques need to be integrated with WPT systems for safe and efficient operation.

References

- [1] IEA (2019), Global EV Outlook 2019, IEA, Paris <https://www.iea.org/reports/global-ev-outlook-2019>.
- [2] A. Ahmad, M. S. Alam, and R. Chabaan, “A Comprehensive Review of Wireless Charging Technologies for Electric Vehicles,” *IEEE Trans. Transp. Electrification*, vol. 4, no. 1, pp. 38–63, Mar. 2018, doi: 10.1109/TTE.2017.2771619.
- [3] N. Tesla, “Apparatus for transmitting electrical energy,” US1119732A, Dec. 01, 1914.
- [4] D. Patil, M. K. McDonough, J. M. Miller, B. Fahimi, and P. T. Balsara, “Wireless Power Transfer for Vehicular Applications: Overview and Challenges,” *IEEE Trans. Transp. Electrification*, vol. 4, no. 1, pp. 3–37, Mar. 2018, doi: 10.1109/TTE.2017.2780627.
- [5] Y. Jang, S. Jeong, and M. Lee, “Initial Energy Logistics Cost Analysis for Stationary, Quasi-Dynamic, and Dynamic Wireless Charging Public Transportation Systems,” *Energies*, vol. 9, no. 7, p. 483, Jun. 2016, doi: 10.3390/en9070483.
- [6] G. A. Covic and J. T. Boys, “Modern Trends in Inductive Power Transfer for Transportation Applications,” *IEEE J. Emerg. Sel. Top. Power Electron.*, vol. 1, no. 1, pp. 28–41, Mar. 2013, doi: 10.1109/JESTPE.2013.2264473.
- [7] S. Lukic and Z. Pantic, “Cutting the Cord: Static and Dynamic Inductive Wireless Charging of Electric Vehicles,” *IEEE Electrification Mag.*, vol. 1, no. 1, pp. 57–64, Sep. 2013, doi: 10.1109/MELE.2013.2273228.

- [8] A. A. S. Mohamed, C. R. Lashway, and O. Mohammed, "Modeling and Feasibility Analysis of Quasi-dynamic WPT System for EV Applications," *IEEE Trans. Transp. Electrification*, pp. 1–1, 2017, doi: 10.1109/TTE.2017.2682111.
- [9] J. M. Miller *et al.*, "Demonstrating Dynamic Wireless Charging of an Electric Vehicle: The Benefit of Electrochemical Capacitor Smoothing," *IEEE Power Electron. Mag.*, vol. 1, no. 1, pp. 12–24, Mar. 2014, doi: 10.1109/MPEL.2014.2300978.
- [10] V. Cirimele, M. Diana, F. Freschi, and M. Mitolo, "Inductive Power Transfer for Automotive Applications: State-of-the-Art and Future Trends," *IEEE Trans. Ind. Appl.*, vol. 54, no. 5, pp. 4069–4079, Sep. 2018, doi: 10.1109/TIA.2018.2836098.
- [11] L. Patnaik, P. S. Huynh, D. Vincent, and S. S. Williamson, "Wireless Opportunity Charging as an Enabling Technology for EV Battery Size Reduction and Range Extension: Analysis of an Urban Drive Cycle Scenario," in *2018 IEEE PELS Workshop on Emerging Technologies: Wireless Power Transfer (Wow)*, Montréal, QC, Canada, Jun. 2018, pp. 1–5, doi: 10.1109/WoW.2018.8450900.
- [12] O. C. Onar, S. L. Campbell, L. E. Seiber, C. P. White, and M. Chinthavali, "A high-power wireless charging system development and integration for a Toyota RAV4 electric vehicle," Jun. 2016, pp. 1–8, doi: 10.1109/ITEC.2016.7520247.
- [13] C. C. Mi, G. Buja, S. Y. Choi, and C. T. Rim, "Modern Advances in Wireless Power Transfer Systems for Roadway Powered Electric Vehicles," *IEEE Trans. Ind. Electron.*, vol. 63, no. 10, pp. 6533–6545, Oct. 2016, doi: 10.1109/TIE.2016.2574993.

- [14] “J2954B (WIP) Wireless Power Transfer for Light-Duty Plug-In/Electric Vehicles and Alignment Methodology - SAE International,” Jan. 09, 2019. <https://www.sae.org/standards/content/j2954/> (accessed Jan. 09, 2019).
- [15] B. Kushwaha, G. Rituraj, and P. Kumar, “3-D Analytical Model for Computation of Mutual Inductance for Different Misalignment with Shielding in Wireless Power Transfer System,” *IEEE Trans. Transp. Electrification*, pp. 1–1, 2017, doi: 10.1109/TTE.2017.2649881.
- [16] J. Ma, X. Huang, J. Zhou, Y. Fang, J. Zhang, and Y. Gao, “Magnetic field design for optimal wireless power transfer to multiple receivers,” *IET Power Electron.*, vol. 9, no. 9, pp. 1885–1893, Jul. 2016, doi: 10.1049/iet-pel.2015.0915.
- [17] S. Y. Jeong, V. X. Thai, J. H. Park, and C. T. Rim, “Metal Object Detection System with Parallel-mistuned Resonant Circuits and Nullifying Induced Voltage for Wireless EV Chargers,” in *2018 International Power Electronics Conference (IPEC-Niigata 2018 -ECCE Asia)*, May 2018, pp. 2564–2568, doi: 10.23919/IPEC.2018.8507535.
- [18] Y. H. Sohn, B. H. Choi, E. S. Lee, and C. T. Rim, “Comparisons of magnetic field shaping methods for ubiquitous wireless power transfer,” in *2015 IEEE PELS Workshop on Emerging Technologies: Wireless Power (2015 WoW)*, Jun. 2015, pp. 1–6, doi: 10.1109/WoW.2015.7132810.
- [19] P. T. Jones and O. Onar, “Impact of Wireless Power Transfer in transportation: Future transportation enabler, or near term distraction,” in *2014 IEEE International Electric Vehicle Conference (IEVC)*, Dec. 2014, pp. 1–7, doi: 10.1109/IEVC.2014.7056203.

- [20] S. Y. Choi, B. W. Gu, S. Y. Jeong, and C. T. Rim, “Advances in Wireless Power Transfer Systems for Roadway-Powered Electric Vehicles,” *IEEE J. Emerg. Sel. Top. Power Electron.*, vol. 3, no. 1, pp. 18–36, Mar. 2015, doi: 10.1109/JESTPE.2014.2343674.
- [21] D. Boffey, “World’s first electrified road for charging vehicles opens in Sweden,” *The Guardian*, Apr. 12, 2018.
- [22] M. P. Theodoridis, “Effective Capacitive Power Transfer,” *IEEE Trans. Power Electron.*, vol. 27, no. 12, pp. 4906–4913, Dec. 2012, doi: 10.1109/TPEL.2012.2192502.
- [23] J. Dai and D. C. Ludois, “Capacitive Power Transfer Through a Conformal Bumper for Electric Vehicle Charging,” *IEEE J. Emerg. Sel. Top. Power Electron.*, vol. 4, no. 3, pp. 1015–1025, Sep. 2016, doi: 10.1109/JESTPE.2015.2505622.
- [24] H. Zhang, F. Lu, H. Hofmann, W. Liu, and C. Mi, “A 4-Plate Compact Capacitive Coupler Design and LCL-Compensated Topology for Capacitive Power Transfer in Electric Vehicle Charging Applications,” *IEEE Trans. Power Electron.*, pp. 1–1, 2016, doi: 10.1109/TPEL.2016.2520963.
- [25] J. Dai and D. C. Ludois, “A Survey of Wireless Power Transfer and a Critical Comparison of Inductive and Capacitive Coupling for Small Gap Applications,” *IEEE Trans. Power Electron.*, vol. 30, no. 11, pp. 6017–6029, Nov. 2015, doi: 10.1109/TPEL.2015.2415253.
- [26] J. L. Villa, J. Sallan, J. F. Sanz Osorio, and A. Llombart, “High-Misalignment Tolerant Compensation Topology For ICPT Systems,” *IEEE Trans. Ind. Electron.*, vol. 59, no. 2, pp. 945–951, Feb. 2012, doi: 10.1109/TIE.2011.2161055.

- [27] W. Zhang and C. C. Mi, "Compensation Topologies of High-Power Wireless Power Transfer Systems," *IEEE Trans. Veh. Technol.*, vol. 65, no. 6, pp. 4768–4778, Jun. 2016, doi: 10.1109/TVT.2015.2454292.
- [28] F. Lu, H. Zhang, and C. Mi, "A Review on the Recent Development of Capacitive Wireless Power Transfer Technology," *Energies*, vol. 10, no. 11, p. 1752, Nov. 2017, doi: 10.3390/en10111752.
- [29] J. Deng, W. Li, T. D. Nguyen, S. Li, and C. C. Mi, "Compact and Efficient Bipolar Coupler for Wireless Power Chargers: Design and Analysis," *IEEE Trans. Power Electron.*, vol. 30, no. 11, pp. 6130–6140, Nov. 2015, doi: 10.1109/TPEL.2015.2417115.
- [30] B. Luo, R. Mai, Y. Chen, Y. Zhang, and Z. He, "A voltage stress optimization method of capacitive power transfer charging system," Mar. 2017, pp. 1456–1461, doi: 10.1109/APEC.2017.7930890.
- [31] H. Zhang, F. Lu, H. Hofmann, W. Liu, and C. C. Mi, "Six-Plate Capacitive Coupler to Reduce Electric Field Emission in Large Air-Gap Capacitive Power Transfer," *IEEE Trans. Power Electron.*, vol. 33, no. 1, pp. 665–675, Jan. 2018, doi: 10.1109/TPEL.2017.2662583.
- [32] C.-S. Wang, G. A. Covic, and O. H. Stielau, "Power transfer capability and bifurcation phenomena of loosely coupled inductive power transfer systems," *IEEE Trans. Ind. Electron.*, vol. 51, no. 1, pp. 148–157, Feb. 2004, doi: 10.1109/TIE.2003.822038.
- [33] F. Nakao, Y. Matsuo, M. Kitaoka, and H. Sakamoto, "Ferrite core couplers for inductive chargers," in *Power Conversion Conference, 2002. PCC-Osaka 2002*.

- Proceedings of the*, 2002, vol. 2, pp. 850–854, Accessed: May 15, 2017. [Online]. Available: <http://ieeexplore.ieee.org/abstract/document/997631/>.
- [34] Pathipati Vamsi, “Design of a Novel Ferrite Core based Highly Efficient Wireless Resonant Inductive Power Transfer System,” UOIT, 2016.
- [35] M. Budhia, G. A. Covic, and J. T. Boys, “Design and Optimization of Circular Magnetic Structures for Lumped Inductive Power Transfer Systems,” *IEEE Trans. Power Electron.*, vol. 26, no. 11, pp. 3096–3108, Nov. 2011, doi: 10.1109/TPEL.2011.2143730.
- [36] M. Budhia, J. T. Boys, G. A. Covic, and C.-Y. Huang, “Development of a Single-Sided Flux Magnetic Coupler for Electric Vehicle IPT Charging Systems,” *IEEE Trans. Ind. Electron.*, vol. 60, no. 1, pp. 318–328, Jan. 2013, doi: 10.1109/TIE.2011.2179274.
- [37] D. Vincent, S. Chakraborty, P. S. Huynh, and S. S. Williamson, “Efficiency analysis of a 7.7 kW inductive wireless power transfer system with parallel displacement,” in *2018 IEEE International Conference on Industrial Electronics for Sustainable Energy Systems (IESES)*, Jan. 2018, pp. 409–414, doi: 10.1109/IESES.2018.8349911.
- [38] W. Chen, C. Liu, C. Lee, and Z. Shan, “Cost-Effectiveness Comparison of Coupler Designs of Wireless Power Transfer for Electric Vehicle Dynamic Charging,” *Energies*, vol. 9, no. 11, p. 906, Nov. 2016, doi: 10.3390/en9110906.
- [39] M. Budhia, G. A. Covic, J. T. Boys, and C.-Y. Huang, “Development and evaluation of single sided flux couplers for contactless electric vehicle charging,” in *Energy Conversion Congress and Exposition (ECCE), 2011 IEEE*, 2011, pp. 614–621.

- [40] A. Zaheer, H. Hao, G. A. Covic, and D. Kacprzak, "Investigation of Multiple Decoupled Coil Primary Pad Topologies in Lumped IPT Systems for Interoperable Electric Vehicle Charging," *IEEE Trans. Power Electron.*, vol. 30, no. 4, pp. 1937–1955, Apr. 2015, doi: 10.1109/TPEL.2014.2329693.
- [41] A. Kamineni, G. A. Covic, and J. T. Boys, "Analysis of Coplanar Intermediate Coil Structures in Inductive Power Transfer Systems," *IEEE Trans. Power Electron.*, vol. 30, no. 11, pp. 6141–6154, Nov. 2015, doi: 10.1109/TPEL.2014.2378733.
- [42] V. X. Thai, S. Y. Choi, B. H. Choi, J. H. Kim, and C. T. Rim, "Coreless power supply rails compatible with both stationary and dynamic charging of electric vehicles," in *2015 IEEE 2nd International Future Energy Electronics Conference (IFEEEC)*, Nov. 2015, pp. 1–5, doi: 10.1109/IFEEEC.2015.7361495.
- [43] A. Tejada, C. Carretero, J. T. Boys, and G. A. Covic, "Ferrite-Less Circular Pad With Controlled Flux Cancellation for EV Wireless Charging," *IEEE Trans. Power Electron.*, vol. 32, no. 11, pp. 8349–8359, Nov. 2017, doi: 10.1109/TPEL.2016.2642192.
- [44] S. Y. Choi, B. W. Gu, S. W. Lee, W. Y. Lee, J. Huh, and C. T. Rim, "Generalized Active EMF Cancel Methods for Wireless Electric Vehicles," *IEEE Trans. Power Electron.*, vol. 29, no. 11, pp. 5770–5783, Nov. 2014, doi: 10.1109/TPEL.2013.2295094.
- [45] A. Gil and J. Taiber, "A Literature Review in Dynamic Wireless Power Transfer for Electric Vehicles: Technology and Infrastructure Integration Challenges," in *Sustainable Automotive Technologies 2013*, J. Wellnitz, A. Subic, and R. Trufin, Eds. Cham: Springer International Publishing, 2014, pp. 289–298.

- [46] G. A. J. Elliott, G. A. Covic, D. Kacprzak, and J. T. Boys, "A New Concept: Asymmetrical Pick-Ups for Inductively Coupled Power Transfer Monorail Systems," *IEEE Trans. Magn.*, vol. 42, no. 10, pp. 3389–3391, Oct. 2006, doi: 10.1109/TMAG.2006.879619.
- [47] G. A. J. Elliott, J. T. Boys, and G. A. Covic, "A Design Methodology for Flat Pick-up ICPT Systems," in *2006 1st IEEE Conference on Industrial Electronics and Applications*, May 2006, pp. 1–7, doi: 10.1109/ICIEA.2006.257165.
- [48] S. Raabe, G. A. J. Elliott, G. A. Covic, and J. T. Boys, "A Quadrature Pickup for Inductive Power Transfer Systems," in *2007 2nd IEEE Conference on Industrial Electronics and Applications*, May 2007, pp. 68–73, doi: 10.1109/ICIEA.2007.4318371.
- [49] T. Fujita, T. Yasuda, and H. Akagi, "A Dynamic Wireless Power Transfer System Applicable to a Stationary System," *IEEE Trans. Ind. Appl.*, vol. 53, no. 4, pp. 3748–3757, Jul. 2017, doi: 10.1109/TIA.2017.2680400.
- [50] B. Ge, D. C. Ludois, and R. Perez, "The use of dielectric coatings in capacitive power transfer systems," in *2014 IEEE Energy Conversion Congress and Exposition (ECCE)*, Sep. 2014, pp. 2193–2199, doi: 10.1109/ECCE.2014.6953695.
- [51] D. Rozario, N. A. Azeez, and S. S. Williamson, "Analysis and design of coupling capacitors for contactless capacitive power transfer systems," Jun. 2016, pp. 1–7, doi: 10.1109/ITEC.2016.7520244.
- [52] S. Li, Z. Liu, H. Zhao, L. Zhu, C. Shuai, and Z. Chen, "Wireless Power Transfer by Electric Field Resonance and Its Application in Dynamic Charging," *IEEE Trans.*

- Ind. Electron.*, vol. 63, no. 10, pp. 6602–6612, Oct. 2016, doi: 10.1109/TIE.2016.2577625.
- [53] C. Mi, “High power capacitive power transfer for electric vehicle charging applications,” in *Power Electronics Systems and Applications (PESA), 2015 6th International Conference on*, 2015, pp. 1–4, Accessed: May 09, 2017. [Online]. Available: <http://ieeexplore.ieee.org/abstract/document/7398937/>.
- [54] H. Zhang, F. Lu, H. Hofmann, W. Liu, and C. C. Mi, “An LC-Compensated Electric Field Repeater for Long-Distance Capacitive Power Transfer,” *IEEE Trans. Ind. Appl.*, vol. 53, no. 5, pp. 4914–4922, Sep. 2017, doi: 10.1109/TIA.2017.2697846.
- [55] F. Lu, H. Zhang, H. Hofmann, and C. C. Mi, “A Dynamic Charging System With Reduced Output Power Pulsation for Electric Vehicles,” *IEEE Trans. Ind. Electron.*, vol. 63, no. 10, pp. 6580–6590, Oct. 2016, doi: 10.1109/TIE.2016.2563380.
- [56] “IEC 61980-1 - Electric Vehicle Wireless Power Transfer (WPT) Systems – Part 1: General requirements | Engineering360,” Jan. 25, 2019. <https://standards.globalspec.com/std/10072061/iec-61980-1> (accessed Jan. 25, 2019).
- [57] “ISO/PAS 19363:2017,” *ISO*, Jan. 25, 2019. <http://www.iso.org/cms/render/live/en/sites/isoorg/contents/data/standard/06/47/64700.html> (accessed Jan. 25, 2019).
- [58] “Electric Vehicle Charging Stations | Industries | UL,” *Industries*, Jan. 09, 2019. <https://industries.ul.com/energy/e-mobility/charging-stations> (accessed Jan. 09, 2019).
- [59] Hybrid - EV Committee, “Signaling Communication for Wirelessly Charged Electric Vehicles,” SAE International, Jan. 2019. doi: 10.4271/J2931/6_201508.

- [60] Hybrid - EV Committee, "Communication between Wireless Charged Vehicles and Wireless EV Chargers," SAE International, Jan. 2019. doi: 10.4271/J2847/6_201508.
- [61] W. Niu, J. Chu, W. Gu, and A. Shen, "Exact Analysis of Frequency Splitting Phenomena of Contactless Power Transfer Systems," *IEEE Trans. Circuits Syst. Regul. Pap.*, vol. 60, no. 6, pp. 1670–1677, Jun. 2013, doi: 10.1109/TCSI.2012.2221172.
- [62] K. Aditya and S. S. Williamson, "Design Guidelines to Avoid Bifurcation in a Series-Series Compensated Inductive Power Transfer System," *IEEE Trans. Ind. Electron.*, pp. 1–1, 2018, doi: 10.1109/TIE.2018.2851953.
- [63] F. Lu, H. Zhang, H. Hofmann, and C. Mi, "A CLLC-compensated high power and large air-gap capacitive power transfer system for electric vehicle charging applications," in *2016 IEEE Applied Power Electronics Conference and Exposition (APEC)*, Mar. 2016, pp. 1721–1725, doi: 10.1109/APEC.2016.7468099.
- [64] F. Lu, H. Zhang, H. Hofmann, and C. Mi, "A Double-Sided LCLC-Compensated Capacitive Power Transfer System for Electric Vehicle Charging," *IEEE Trans. Power Electron.*, vol. 30, no. 11, pp. 6011–6014, Nov. 2015, doi: 10.1109/TPEL.2015.2446891.
- [65] J. L. Villa, A. Llombart, J. F. Sanz, and J. Sallan, "Practical development of a 5 kW ICPT system SS compensated with a large air gap," in *Industrial Electronics, 2007. ISIE 2007. IEEE International Symposium on*, 2007, pp. 1219–1223.
- [66] A. M. Sodagar and P. Amiri, "Capacitive coupling for power and data telemetry to implantable biomedical microsystems," in *2009 4th International IEEE/EMBS*

- Conference on Neural Engineering*, Apr. 2009, pp. 411–414, doi: 10.1109/NER.2009.5109320.
- [67] C. T. Rim and C. Mi, *Wireless Power Transfer for Electric Vehicles and Mobile Devices*. Chichester, UK: John Wiley & Sons, Ltd, 2017.
- [68] R. Bosshard and J. W. Kolar, “Multi-Objective Optimization of 50 kW/85 kHz IPT System for Public Transport,” *IEEE J. Emerg. Sel. Top. Power Electron.*, vol. 4, no. 4, pp. 1370–1382, Dec. 2016, doi: 10.1109/JESTPE.2016.2598755.
- [69] B. Regensburger, A. Kumar, S. Sinha, and K. Afridi, “High-Performance 13.56-MHz Large Air-Gap Capacitive Wireless Power Transfer System for Electric Vehicle Charging,” in *2018 IEEE 19th Workshop on Control and Modeling for Power Electronics (COMPEL)*, Jun. 2018, pp. 1–4, doi: 10.1109/COMPEL.2018.8460153.
- [70] B. Regensburger, J. Estrada, A. Kumar, S. Sinha, Z. Popović, and K. K. Afridi, “High-Performance Capacitive Wireless Power Transfer System for Electric Vehicle Charging with Enhanced Coupling Plate Design,” in *2018 IEEE Energy Conversion Congress and Exposition (ECCE)*, Sep. 2018, pp. 2472–2477, doi: 10.1109/ECCE.2018.8557881.
- [71] F. Lu, H. Zhang, and C. Mi, “A Two-Plate Capacitive Wireless Power Transfer System for Electric Vehicle Charging Applications,” *IEEE Trans. Power Electron.*, pp. 1–1, 2017, doi: 10.1109/TPEL.2017.2735365.
- [72] P. B. Bobba and K. R. Rajagopal, “Modeling and analysis of hybrid energy storage systems used in Electric vehicles,” in *2012 IEEE International Conference on Power Electronics, Drives and Energy Systems (PEDES)*, Dec. 2012, pp. 1–6, doi: 10.1109/PEDES.2012.6484365.

- [73] G. R. Nagendra, G. A. Covic, and J. T. Boys, "Determining the Physical Size of Inductive Couplers for IPT EV Systems," *IEEE J. Emerg. Sel. Top. Power Electron.*, vol. 2, no. 3, pp. 571–583, Sep. 2014, doi: 10.1109/JESTPE.2014.2302295.
- [74] C. Zheng, H. Ma, J.-S. Lai, and L. Zhang, "Design Considerations to Reduce Gap Variation and Misalignment Effects for the Inductive Power Transfer System," *IEEE Trans. Power Electron.*, vol. 30, no. 11, pp. 6108–6119, Nov. 2015, doi: 10.1109/TPEL.2015.2424893.
- [75] A. Ahmad, M. S. Alam, and R. C. Chaban, "Efficiency enhancement of wireless charging for Electric vehicles through reduction of coil misalignment," in *Transportation Electrification Conference and Expo (ITEC), 2017 IEEE*, 2017, pp. 21–26.
- [76] F. Lu, H. Zhang, H. Hofmann, W. Su, and C. C. Mi, "A Dual-Coupled LCC-Compensated IPT System With a Compact Magnetic Coupler," *IEEE Trans. Power Electron.*, vol. 33, no. 7, pp. 6391–6402, Jul. 2018, doi: 10.1109/TPEL.2017.2748391.
- [77] F. Y. Lin, G. A. Covic, and J. T. Boys, "Evaluation of Magnetic Pad Sizes and Topologies for Electric Vehicle Charging," *IEEE Trans. Power Electron.*, vol. 30, no. 11, pp. 6391–6407, Nov. 2015, doi: 10.1109/TPEL.2015.2419592.
- [78] "ICNIRP | HF (100 kHz-300 GHz)," Jan. 10, 2019. <https://www.icnirp.org/en/frequencies/high-frequency/index.html> (accessed Jan. 10, 2019).

- [79] “ICNIRP | LF (1 Hz-100 kHz),” Jan. 10, 2019. <https://www.icnirp.org/en/frequencies/low-frequency/index.html> (accessed Jan. 10, 2019).
- [80] “IEEE C95.1-2005 - IEEE Standard for Safety Levels with Respect to Human Exposure to Radio Frequency Electromagnetic Fields, 3 kHz to 300 GHz,” Jan. 10, 2019. https://standards.ieee.org/standard/C95_1-2005.html (accessed Jan. 10, 2019).
- [81] P. Ding, L. Bernard, L. Pichon, and A. Razek, “Evaluation of Electromagnetic Fields in Human Body Exposed to Wireless Inductive Charging System,” *IEEE Trans. Magn.*, vol. 50, no. 2, pp. 1037–1040, Feb. 2014, doi: 10.1109/TMAG.2013.2284245.
- [82] A. Christ *et al.*, “Evaluation of Wireless Resonant Power Transfer Systems With Human Electromagnetic Exposure Limits,” *IEEE Trans. Electromagn. Compat.*, pp. 1–10, 2012, doi: 10.1109/TEM.2012.2219870.
- [83] Z. Bi, T. Kan, C. C. Mi, Y. Zhang, Z. Zhao, and G. A. Keoleian, “A review of wireless power transfer for electric vehicles: Prospects to enhance sustainable mobility,” *Appl. Energy*, vol. 179, pp. 413–425, Oct. 2016, doi: 10.1016/j.apenergy.2016.07.003.
- [84] B. Regensburger, A. Kumar, S. Sinha, and K. K. Afridi, “Impact of Foreign Objects on the Performance of Capacitive Wireless Charging Systems for Electric Vehicles,” in *2018 IEEE Transportation Electrification Conference and Expo (ITEC)*, Jun. 2018, pp. 892–897, doi: 10.1109/ITEC.2018.8450220.
- [85] N. Kuyvenhoven, C. Dean, J. Melton, J. Schwannecke, and A. E. Umenei, “Development of a foreign object detection and analysis method for wireless power systems,” in *2011 IEEE Symposium on Product Compliance Engineering Proceedings*, Oct. 2011, pp. 1–6, doi: 10.1109/PSES.2011.6088250.

- [86] G. C. Jang, S. Y. Jeong, H. G. Kwak, and C. T. Rim, "Metal object detection circuit with non-overlapped coils for wireless EV chargers," in *2016 IEEE 2nd Annual Southern Power Electronics Conference (SPEC)*, Dec. 2016, pp. 1–6, doi: 10.1109/SPEC.2016.7846132.
- [87] H. Kudo, K. Ogawa, N. Oodachi, N. Deguchi, and H. Shoki, "Detection of a metal obstacle in wireless power transfer via magnetic resonance," in *2011 IEEE 33rd International Telecommunications Energy Conference (INTELEC)*, Oct. 2011, pp. 1–6, doi: 10.1109/INTLEC.2011.6099728.
- [88] N. H. Kutkut, D. M. Divan, D. W. Novotny, and R. H. Marion, "Design considerations and topology selection for a 120-kW IGBT converter for EV fast charging," *IEEE Trans. Power Electron.*, vol. 13, no. 1, pp. 169–178, 1998.
- [89] A. Pevere, R. Petrella, C. C. Mi, and S. Zhou, "Design of a high efficiency 22 kW wireless power transfer system for EVs fast contactless charging stations," in *Electric Vehicle Conference (IEVC), 2014 IEEE International*, 2014, pp. 1–7.
- [90] J. F. Sanz, J. L. Villa, J. Sallan, J. M. Perie, and L. G. Duarte, "UNPLUGGED Project: development of a 50 kW inductive electric vehicle battery charge system," in *Electric Vehicle Symposium and Exhibition (EVS27), 2013 World*, 2013, pp. 1–7.
- [91] A. Schroedermeier and D. C. Ludois, "Integrated Inductor and Capacitor With Co-located Electric and Magnetic Fields," *IEEE Trans. Ind. Appl.*, vol. 53, no. 1, pp. 380–390, Jan. 2017, doi: 10.1109/TIA.2016.2604219.
- [92] Y.-G. Su, W. Zhou, A. P. Hu, C.-S. Tang, S.-Y. Xie, and Y. Sun, "Full-Duplex Communication on the Shared Channel of a Capacitively Coupled Power Transfer

- System,” *IEEE Trans. Power Electron.*, vol. 32, no. 4, pp. 3229–3239, Apr. 2017, doi: 10.1109/TPEL.2016.2580607.
- [93] X. Li, C. Tang, X. Dai, P. Deng, and Y. Su, “An Inductive and Capacitive Combined Parallel Transmission of Power and Data for Wireless Power Transfer Systems,” *IEEE Trans. Power Electron.*, vol. 33, no. 6, pp. 4980–4991, Jun. 2018, doi: 10.1109/TPEL.2017.2725990.
- [94] F. Lu, H. Zhang, H. Hofmann, and C. C. Mi, “An Inductive and Capacitive Combined Wireless Power Transfer System With LC-Compensated Topology,” *IEEE Trans. Power Electron.*, vol. 31, no. 12, pp. 8471–8482, Dec. 2016, doi: 10.1109/TPEL.2016.2519903.
- [95] D. Vincent, P. H. Sang, and S. S. Williamson, “Feasibility study of hybrid inductive and capacitive wireless power transfer for future transportation,” in *2017 IEEE Transportation Electrification Conference and Expo (ITEC)*, Jun. 2017, pp. 229–233, doi: 10.1109/ITEC.2017.7993276.
- [96] F. Lu, H. Zhang, H. Hofmann, and C. C. Mi, “An Inductive and Capacitive Integrated Coupler and Its LCL Compensation Circuit Design for Wireless Power Transfer,” *IEEE Trans. Ind. Appl.*, vol. 53, no. 5, pp. 4903–4913, Sep. 2017, doi: 10.1109/TIA.2017.2697838.
- [97] B. Luo, T. Long, R. Mai, R. Dai, Z. He, and W. Li, “Analysis and design of hybrid inductive and capacitive wireless power transfer for high-power applications,” *IET Power Electron.*, vol. 11, no. 14, pp. 2263–2270, 2018, doi: 10.1049/iet-pel.2018.5279.

- [98] *Unmanned aircraft systems: UAS*. Montréal: International Civil Aviation Organization, 2011. Cir 328, ISBN 978-92-9231-751-5.
- [99] T. Campi, F. Dionisi, S. Cruciani, V. De Santis, M. Feliziani, and F. Maradei, “Magnetic field levels in drones equipped with Wireless Power Transfer technology,” in *Electromagnetic Compatibility (APEMC), 2016 Asia-Pacific International Symposium on*, 2016, vol. 1, pp. 544–547.
- [100] T. Campi, S. Cruciani, G. Rodríguez, and M. Feliziani, “Coil design of a wireless power transfer charging system for a drone,” in *Electromagnetic Field Computation (CEFC), 2016 IEEE Conference on*, 2016, pp. 1–1.
- [101] H. B. Palmer, “The Capacitance of a Parallel-Plate Capacitor by the Schwartz-Christoffel Transformation,” *Trans. Am. Inst. Electr. Eng.*, vol. 56, no. 3, pp. 363–366, Mar. 1937, doi: 10.1109/T-AIEE.1937.5057547.
- [102] H. Nishiyama and M. Nakamura, “Form and capacitance of parallel-plate capacitors,” *IEEE Trans. Compon. Packag. Manuf. Technol. Part A*, vol. 17, no. 3, pp. 477–484, Sep. 1994, doi: 10.1109/95.311759.
- [103] Evatran, “Mainstream Electric Car Makers Race to Wireless EV Charging,” *Plugless Power*. <https://www.pluglesspower.com/learn/mainstream-electric-cars-are-headed-towards-wireless-charging/> (accessed Apr. 26, 2020).
- [104] O. C. Onar, M. Chinthavali, S. Campbell, P. Ning, C. P. White, and J. M. Miller, “A SiC MOSFET based inverter for wireless power transfer applications,” in *2014 IEEE Applied Power Electronics Conference and Exposition - APEC 2014*, Mar. 2014, pp. 1690–1696, doi: 10.1109/APEC.2014.6803533.

- [105] A. Q. Cai and L. Siek, “A 2-kW, 95% Efficiency Inductive Power Transfer System Using Gallium Nitride Gate Injection Transistors,” *IEEE J. Emerg. Sel. Top. Power Electron.*, vol. 5, no. 1, pp. 458–468, Mar. 2017, doi: 10.1109/JESTPE.2016.2632743.
- [106] S. G. Rosu, M. Khalilian, V. Cirimele, and P. Guglielmi, “A dynamic wireless charging system for electric vehicles based on DC/AC converters with SiC MOSFET-IGBT switches and resonant gate-drive,” in *IECON 2016 - 42nd Annual Conference of the IEEE Industrial Electronics Society*, Oct. 2016, pp. 4465–4470, doi: 10.1109/IECON.2016.7793809.
- [107] S. Li, W. Li, J. Deng, T. D. Nguyen, and C. C. Mi, “A Double-Sided LCC Compensation Network and Its Tuning Method for Wireless Power Transfer,” *IEEE Trans. Veh. Technol.*, vol. 64, no. 6, pp. 2261–2273, Jun. 2015, doi: 10.1109/TVT.2014.2347006.
- [108] F. Lu *et al.*, “A high efficiency and compact inductive power transfer system compatible with both 3.3kW and 7.7kW receivers,” in *2017 IEEE Applied Power Electronics Conference and Exposition (APEC)*, Mar. 2017, pp. 3669–3673, doi: 10.1109/APEC.2017.7931225.
- [109] J. Dai and D. C. Ludois, “Single active switch power electronics for kilowatt scale capacitive power transfer,” *IEEE J. Emerg. Sel. Top. Power Electron.*, vol. 3, no. 1, pp. 315–323, 2015.
- [110] B. Regensburger *et al.*, “High-performance large air-gap capacitive wireless power transfer system for electric vehicle charging,” in *Transportation Electrification Conference and Expo (ITEC), 2017 IEEE*, 2017, pp. 638–643.

- [111] S. Sinha, B. Regensburger, K. Doubleday, A. Kumar, S. Pervaiz, and K. K. Afridi, “High-power-transfer-density capacitive wireless power transfer system for electric vehicle charging,” in *2017 IEEE Energy Conversion Congress and Exposition (ECCE)*, Oct. 2017, pp. 967–974, doi: 10.1109/ECCE.2017.8095890.
- [112] A. Sepahvand, A. Kumar, K. Afridi, and D. Maksimović, “High power transfer density and high efficiency 100 MHz capacitive wireless power transfer system,” in *Control and Modeling for Power Electronics (COMPEL), 2015 IEEE 16th Workshop on*, 2015, pp. 1–4, Accessed: May 09, 2017. [Online]. Available: <http://ieeexplore.ieee.org/abstract/document/7236492/>.
- [113] D. Rozario, N. A. Azeez, and S. S. Williamson, “A modified resonant converter for wireless capacitive power transfer systems used in battery charging applications,” in *Transportation Electrification Conference and Expo (ITEC), 2016 IEEE*, 2016, pp. 1–6, Accessed: May 09, 2017. [Online]. Available: <http://ieeexplore.ieee.org/abstract/document/7520272/>.
- [114] L. Huang and A. P. Hu, “Defining the mutual coupling of capacitive power transfer for wireless power transfer,” *Electron. Lett.*, vol. 51, no. 22, pp. 1806–1807, 2015.
- [115] D. Vincent, P. S. Huynh, N. A. Azeez, L. Patnaik, and S. S. Williamson, “Evolution of Hybrid Inductive and Capacitive AC Links for Wireless EV Charging -A Comparative Overview,” *IEEE Trans. Transp. Electrification*, pp. 1–1, 2019, doi: 10.1109/TTE.2019.2923883.
- [116] X. Chen, S. Yu, S. Song, R. T. H. Li, X. Yang, and Z. Zhang, “Hybrid coupler for 6.78 MHz desktop wireless power transfer applications with stable open-loop gain,”

- IET Power Electron.*, vol. 12, no. 10, pp. 2642–2649, Aug. 2019, doi: 10.1049/iet-pel.2018.6199.
- [117] W. Zhou, Y. Su, L. Huang, X. Qing, and A. P. Hu, “Wireless Power Transfer Across a Metal Barrier by Combined Capacitive and Inductive Coupling,” *IEEE Trans. Ind. Electron.*, vol. 66, no. 5, pp. 4031–4041, May 2019, doi: 10.1109/TIE.2018.2849991.
- [118] O. H. Stielau and G. A. Covic, “Design of loosely coupled inductive power transfer systems,” in *Proc. of International Conference on Power System Technology*, Perth, WA, Australia, 2000, vol. 1, pp. 85–90, Accessed: May 15, 2017. [Online]. Available: <http://ieeexplore.ieee.org/abstract/document/900036/>.
- [119] F. Lu, H. Zhang, H. Hofmann, and C. C. Mi, “A Double-Sided LC-Compensation Circuit for Loosely Coupled Capacitive Power Transfer,” *IEEE Trans. Power Electron.*, vol. 33, no. 2, pp. 1633–1643, Feb. 2018, doi: 10.1109/TPEL.2017.2674688.
- [120] K. Aditya and S. S. Williamson, “Design Guidelines to Avoid Bifurcation in a Series-Series Compensated Inductive Power Transfer System,” *IEEE Trans. Ind. Electron.*, pp. 1–1, 2018, doi: 10.1109/TIE.2018.2851953.
- [121] H. A. Wheeler, “Simple Inductance Formulas for Radio Coils,” *Proc. Inst. Radio Eng.*, vol. 16, no. 10, pp. 1398–1400, Oct. 1928, doi: 10.1109/JRPROC.1928.221309.
- [122] S. Sinha, A. Kumar, B. Regensburger, and K. K. Afridi, “A New Design Approach to Mitigating the Effect of Parasitics in Capacitive Wireless Power Transfer Systems for Electric Vehicle Charging,” *IEEE Trans. Transp. Electrification*, vol. 5, no. 4, pp. 1040–1059, Dec. 2019, doi: 10.1109/TTE.2019.2931869.

Appendix A.

A1. Publications

Journal publications:

- [1] **D. Vincent**, P. S. Huynh, and S. S. Williamson, " A Three-Leg Inverter Driven Hybrid Inductive and Capacitive Wireless Power Transfer System" (to be submitted).
- [2] **D. Vincent**, A. V. J. S. Praneeth, and S. S. Williamson "Modeling, Design, and Verification of a Reduced Capacitive Wireless Power Transfer System Model for Transportation Electrification Applications" (to be submitted).
- [3] **D. Vincent**, P. S. Huynh, N. A. Azeez, L. Patnaik, and S. S. Williamson, "Evolution of Hybrid Inductive and Capacitive AC Links for Wireless EV Charging -A Comparative Overview," in IEEE Transactions on Transportation Electrification, June 2019.
- [4] **D. Vincent**, P. S. Huynh, L. Patnaik, David Capano, and S.S. Williamson, "Accelerating the autonomous electric transportation revolution: Wireless charging and advanced battery management systems" IEEE Transportation Electrification Community (TEC), e-newsletter, Feb.2018.
- [5] P. S. Huynh, D. Ronanki, **D. Vincent**, and S. S. Williamson "Direct AC-AC Active-Clamped Half-Bridge Converter for Inductive Charging Applications," in IEEE Transactions on Power Electronics (Early access)
- [6] P. S. Huynh, D. Ronanki, **D. Vincent**, L. Patnaik, and S. S. Williamson "Overview and Comparative Assessment of Single-Phase Power Converter Topologies of Inductive Wireless Charging Systems", Energies 2020, 13, 2150.

[7] Ibsan U. Castillo-Zamora, P.S. Huynh, **D. Vincent**, Martin A. Rodriguez-Licea, Francisco J.Perez-Pinal, and S.S. Williamson, "Hexagonal Geometry Coil for a WPT High Power Fast Charging Application" in IEEE Transactions on Transportation Electrification, Sept. 2019.

Conference publications:

[1] **D. Vincent** and S. S. Williamson, "Design and verification of a reduced model for capacitive wireless power transfer system for electric vehicle charging" in Proc. IEEE Energy Conversion Congress and Exposition (ECCE), Michigan, USA, Oct. 2020 (to be presented).

[2] **D. Vincent** and S. S. Williamson, "Role of Dielectrics in the Capacitive Wireless Power Transfer System" in Proc. IEEE International Conference on Industrial Technology (ICIT), Buenos Aires, Argentina, Feb. 2020.

[3] **D. Vincent**, P. S. Huynh, and S. S. Williamson, "A novel three leg inverter for high power hybrid inductive and capacitive wireless power transfer system," in Proc. IEEE 45th Annual Conf. of Industrial Electronics Society (IECON), Lisbon, Portugal, Oct. 2019.

[4] A. V. J. S. Praneeth, **D. Vincent**, and S. S. Williamson, "A Universal On-board Battery Charger with Wide Output Voltage Range for Electric Transportation" in Proc. IEEE Energy Conversion Congress and Exposition (ECCE), Baltimore, MD, Oct. 2019.

[5] **D. Vincent**, P. S. Huynh, L. Patnaik, and S. S. Williamson, "Prospects of capacitive wireless power transfer (C-WPT) for unmanned aerial vehicles," in Proc. IEEE PELS Workshop on Emerging Technologies: Wireless Power Transfer (WoW), Montreal, QC, June 2018.

- [6] L. Patnaik, P. S. Huynh, **D. Vincent**, and S. S. Williamson, “Wireless opportunity charging as an enabling technology for EV battery size reduction and range extension: Analysis of an urban drive cycle scenario,” in Proc. IEEE PELS Workshop on Emerging Technologies: Wireless Power Transfer (WoW), Montreal, QC, June 2018.
- [7] P. S. Huynh, **D. Vincent**, L. Patnaik, and S. S. Williamson, “FPGA-based PWM implementation of matrix converter in inductive wireless power transfer systems,” in Proc. IEEE PELS Workshop on Emerging Technologies: Wireless Power Transfer (WoW), Montreal, QC, June 2018.
- [8] P. S. Huynh, **D. Vincent**, N. Abdul Azeez, L. Patnaik, and S. S. Williamson, “Performance analysis of a single-stage high-frequency AC-AC buck converter for a series-series compensated inductive power transfer system,” in Proc. IEEE Transportation Electrification Conf. and Expo. (ITEC), Long Beach, CA, June 2018.
- [9] **D. Vincent**, S. Chakraborty, P. S. Huynh, and S. S. Williamson, “Efficiency analysis of a 7.7kW inductive wireless power transfer system with parallel displacement,” in Proc. IEEE 1st International Conf. on Industrial Electronics for Sustainable Energy Systems (IECON), Hamilton, New Zealand, Jan. 2018.
- [10] **D. Vincent**, P. S. Huynh, and S. S. Williamson, “Feasibility study of hybrid inductive and capacitive wireless power transfer for future transportation,” in Proc. IEEE Transportation Electrification Conf. and Expo., Chicago, IL, June 2017, pp. 229-233.

Book chapters:

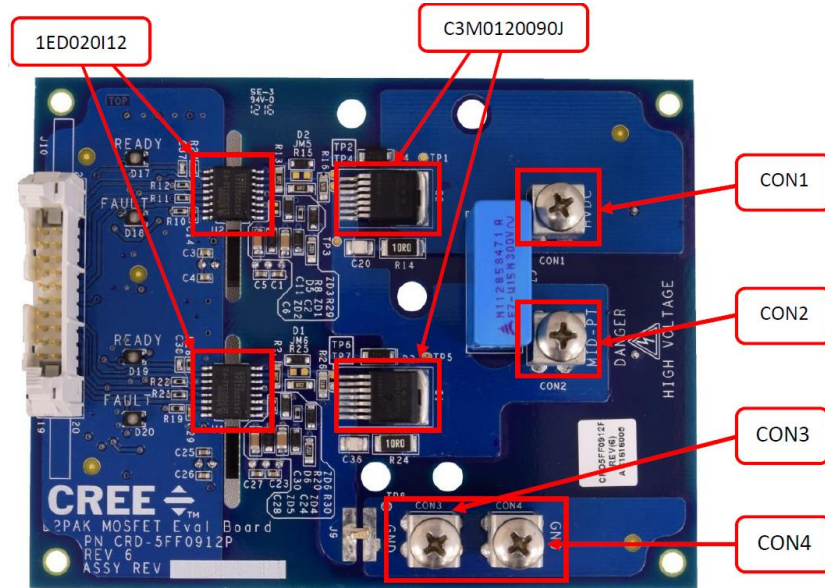
- [1] S.S. Williamson, **D. Vincent**, Jaya Sai Praneeth A V, and P. S. Huynh, “Charging strategies for electrified transport” in the book “Advances in Carbon Management Technologies”, CRC press. (accepted)

Book (under preparation):

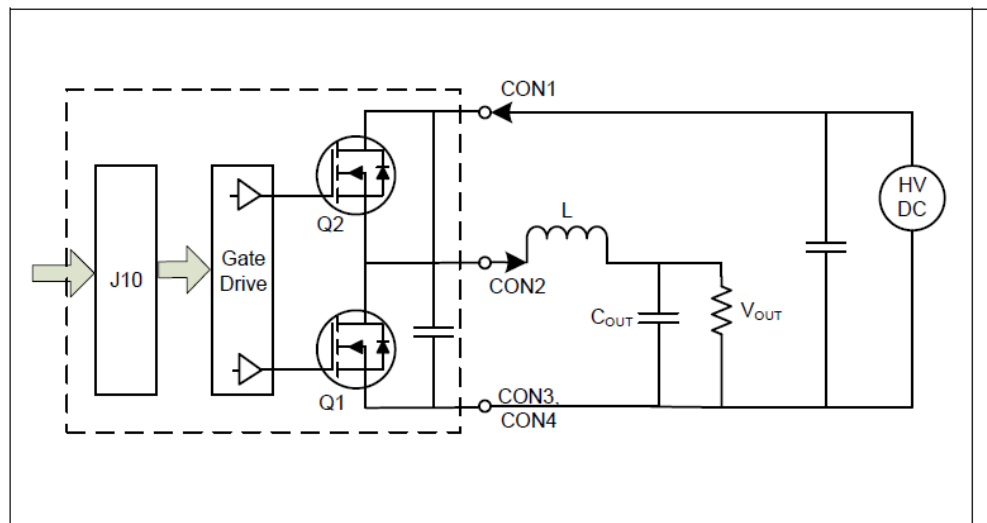
- [1] “Handbook of Electric and Plug-in Hybrid Electric Vehicle Charging” Springer.

Appendix B.

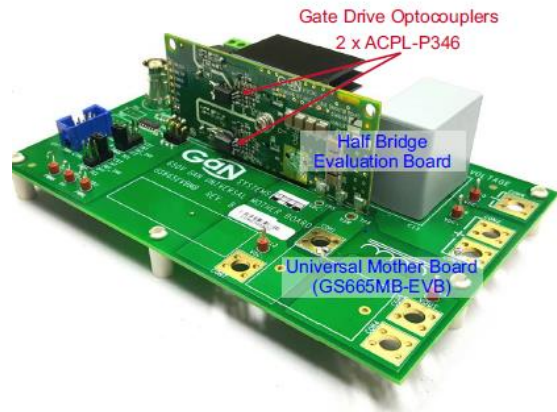
B1. SiC MOSFET half bridge module (CREE®) (CRD-5FF0912P)



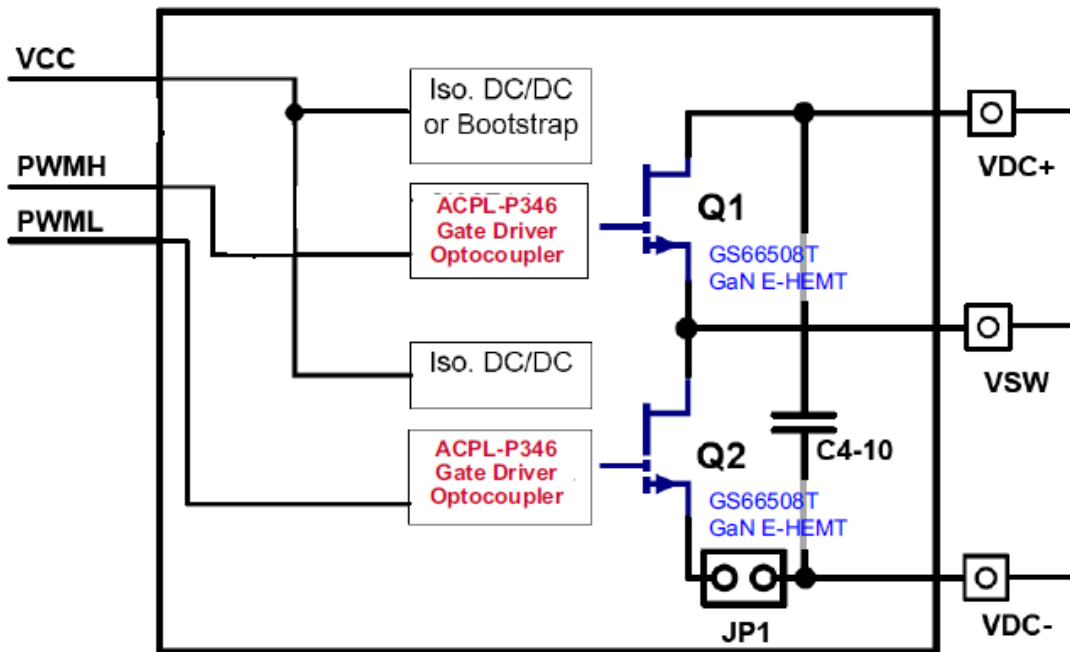
B2. Synchronous buck configuration (Reference: datasheet CRD-5FF0912P)



B3. GaN half bridge module (Broadcom and GaN systems)

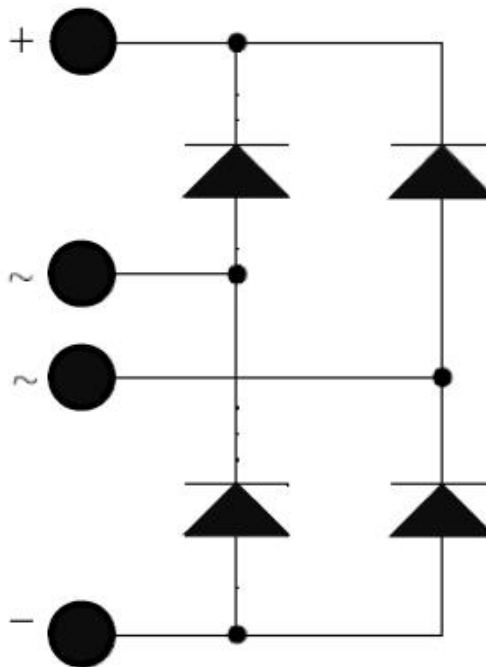


B4. Connection diagram (Reference: ACPL-P346 GaN Systems GaN E-HEMT GS66508T)



B5. Rectifier module Reference: GlobalPower SiC modules: GHXS030A120S-D1
datasheet

SiC SBD Rectifier Bridge Power Module



Appendix C.

C1. Approximate cost and weight comparison of AC link built in the lab (without shielding)

AC link	Cost (CAD) (Transmitter and receiver)	Mass (kg) (Transmitter and receiver)
Inductive	\$ 261.00	5.9
Capacitive	\$ 84.00	1.45